POLITECNICO DI TORINO

Master's Degree in Electronic Engineering

Master's Degree Thesis

Analysis of Quantum Dot-based optical amplifiers: a time-domain traveling-wave approach

Supervisor

Prof. Paolo BARDELLA

Candidate

Andrea MARCHISIO

OCTOBER 2022

Summary

Chirped and tapered Quantum Dot semiconductor optical amplifiers (SOAs) are a valid solution for the direct amplification of ultra-short pulsed sources such as mode-locked lasers, thanks to their broad gain bandwidth and fast recovery times. Traditionally, the SOAs are operated in a so-called single-pass configuration: the radiation enters from one facet, it is amplified and exits from the opposite side. However, it was found out in [7] that a double-pass configuration, where the radiation is extracted from the same facet it is injected into, can lead to enhanced performances, increasing gain and output power, with a limited degradation of the amplified pulses duration, making this configuration a possible future standard for the amplification of light sources.

The main objective of this thesis work consists in the enhancement of an existing time-domain traveling-wave (TDTW) model to allow the simulation of QD layers with different optical properties ("chirped layers") and to include stimulated emission from the second QD excited state, which is typically neglected in theoretical laser models. Those improvements were implemented in an existing TDTW simulator in MATLAB. The reliability of the simulator to predict the behaviour of chirped QD SOAs is validated through the direct comparison of the numerical results with the experimental data measured by the Photonics group at Heriot-Watt University, Edinburgh, on a chirped, tapered and multi-section QD SOA.

After a brief introduction to the problem and a state-of-the-art review in the first chapter, in the second one I concisely examine the peculiar aspects of Quantum Dot physics, with particular attention to their optical properties. Then, in the third chapter, I derive and discuss the equations constituting the TDTW model. In the fourth chapter, I present the device under test alongside the experimental setups considered. In the fifth chapter I extensively describe the main details of the MATLAB implementation of the TDTW model and, finally, in the last chapter, I report and discuss the most relevant simulations results.

The main results presented in this thesis are the following. I found out that this simulator is able to predict the tunable spectral asymmetry affecting the output power spectra at the rear and front facets of the considered SOA under continuous wave biasing conditions, in which the device works as a SLED. Three main spectral

components are registered at 1210 nm, 1240 nm and 1280 nm. Their relative weights can be tuned by changing the front and rear section driving currents. Results are in good agreement with the reference measurements. Moreover, I performed simulations with an external optical excitation in order to test the amplifying capabilities of the device, in both single and double pass amplification configurations. In agreement with the experimental data, considering a source pulse with average power of 2.5 mW and pulse duration of 2.3 ps, the SOA under test in double pass configuration offers an enhancement of signal gain up to almost 4.1 dB with respect to the same device in single pass configuration. This comes without significant pulse degradation: the pulse duration varies between 2.4 ps and 2.7 ps.

Acknowledgements

I would like to thank my parents for supporting me in all my decisions and for teaching me the value of hard work. You made me who I am.
I would like to thank my sisters Silvia and Sara for giving me invaluable advice, guidance, and support, as well as for sparking in me the interest for scientific subjects.
I would like to thank all my friends — old and new — for making these five years a beautiful and fun adventure.
I would like to thank Valeria for always being there, even in the toughest of times, and for helping me believe in myself. I really couldn't have done it without you.

Table of Contents

List of Tables

List of Figures

Chapter 1

Introduction and Thesis outline

In the spectral region for wavelengths in the range $1.1 - 1.3\,\mu m$, Quantum Dot-based active materials caught a considerable amount of interest and show significant promise because the average Quantum Dot size can be finely engineered in order to target a particular wavelength of interest. This latter promising feature has been enabled prominently by the improvements made in the field of epitaxial growth techniques, that allow to create semiconductor heterostructures wherein carriers are confined in one or more directions, on a scale comparable with- or even smaller than- the de Broglie wavelength. Among the reduced dimensionality structures, there are:

- **Quantum Wells**, one-dimensional confinement, two free directions (2D structures);
- **Quantum Wires**, two-dimensional confinement, one free direction (1D structures);
- **Quantum Dots**, three-dimensional confinement, no free direction (0D structures).

These heterostructures, besides being characterized by a different carrier confinement, are also differing for what concerns the energy levels and the *density of states*, namely the fraction of states that will be occupied by the system at a given energy. In particular, Quantum Dots, thanks to the three dimensional confinement of the carriers on a nanometric scale, present a set of discrete energy levels, which are quite similar to those of an atom. Between these energy levels, some interband transitions with specific transition threshold energies can take place and they are the reason why Quantum Dot materials have particular optical properties that differ from those of higher-dimensionality structures. Concerning the density of states, in an ideal case, they are characterized by a series of Dirac's deltas centered

at the previously-mentioned transition energies. Dots with different features (e.g. dimensions), of course, will be characterized by a different set of transition energies. Moreover, if an array of supposedly identical dots is considered, it could also happen that these dots do not have perfectly matched features, meaning that they provide contributions to the total density of states that are slightly detuned with respect to the nominal, ideal transition energy of the Dirac's delta. This results in a density of states that can be assumed to be broadened inhomogeneously.

The main objective of this thesis research consists in the numerical simulation of the two-section tapered semiconductor optical amplifier with chirped quantum dot-based active region in single and double pass configuration, comparing the results with the experimental ones showcased in [7]. This is done by expanding the rate equation model and the time-domain travelling-wave approach presented in [1], [13] and [17], in order to take into account the chirp of the Quantum Dot layers, the emission from the second excited state and some experimental details so to emulate the setup employed in [7] (i.e. the mirror for the double pass configuration and the external cavity filter). A schematic of said device is reported in Figure 1.1.

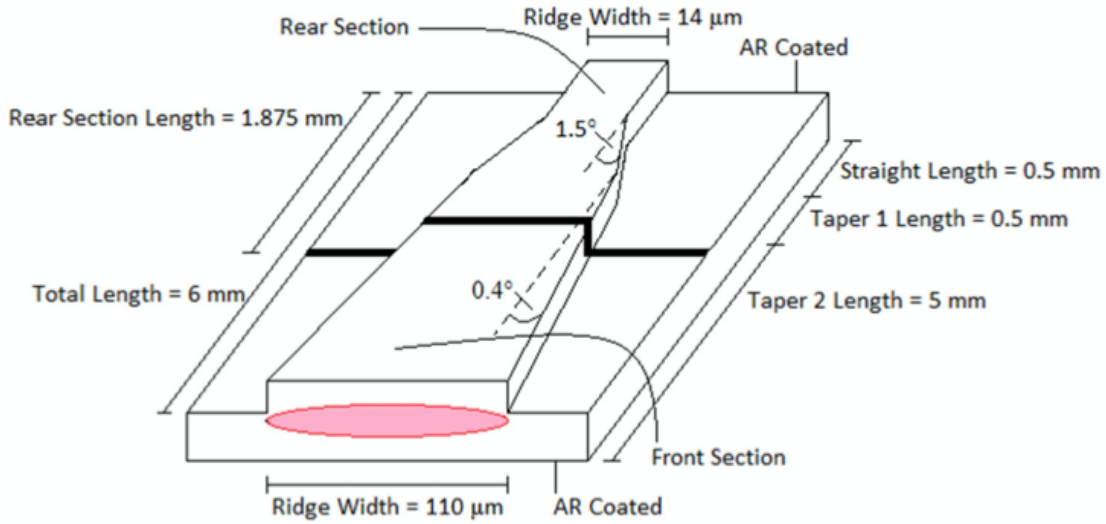

Figure 1.1. Schematic of the device under test. Taken from reference [8].

As highlighted by [7], employing such devices for the amplification of ultrashort pulses offers many advantages, including the low cost, good efficiency and simplicity. Furthermore, on account of the tapered structure and of the chirp of the layers, they offer increased output power, short gain recovery times and large gain over broad bandwidths ([7] and [14]).

This thesis work is organized as follows:

In **Chapter 2**, some fundamental concepts related to the physics and fabrication of Quantum Dots will be presented.

In **Chapter 3**, the theory of the time-domain travelling-wave model implemented in the MATLAB simulation will be discussed, dealing with the travelling wave equations, the multi-population rate equation model and the time-stepped solution of the field propagation equations.

In **Chapter 4**, the device and the experimental setup of [7] will be analysed more in depth, in order to have a better understanding of what has been implemented in the MATLAB program.

In **Chapter 5**, the MATLAB code implementation will be examined in detail, with a reference to the theory and experimental details of the previous chapters.

In **Chapter 6**, finally, the numerical simulation results will be compared with the experimental ones of [7] (external optical excitation) and [9] (continuous wave regime).

Chapter 2

Quantum Dot Basics

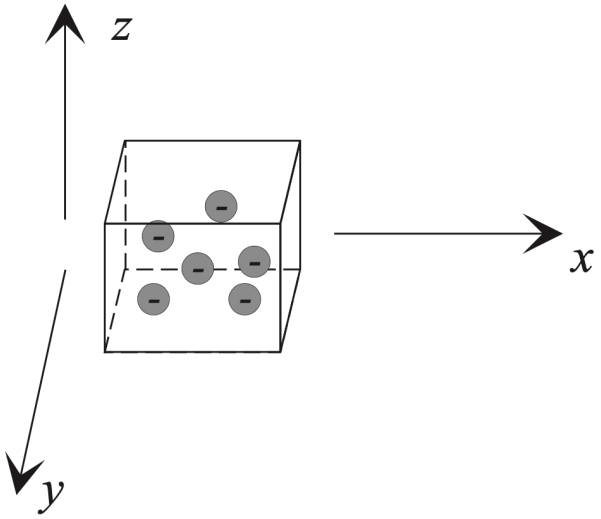

Figure 2.1. Representation of a quantum dot, where the particles are constrained in all directions, making it a zero-dimensional heterostructure. Taken from reference [11].

In this second chapter, the general concepts behind QD heterostructures will be shortly reviewed. In particular, in a first section, the main electronic properties of III-V semiconductor QDs, such as density of states and energy levels, will be discussed; in a second section, there will be an overview of the main techniques that can be exploited for the fabrication of QD-based active materials for optoelectronic applications.

2.1 III-V semiconductor QDs properties

By employing III-V semiconductors, it is possible to realize QDs that are able cover the range of wavelengths between 0.9 µm and 1.8 µm [16], used in telecommunication applications. Depending on the target wavelength, different III-V compounds can be employed for the creation of the heterostructure.
In order to evaluate the energy levels and the other electronic properties of a cylindrical QD, we have to start from the evaluation of the electron and hole eigenstates. Of course, the starting point is the time-independent Schrödinger's equation, assuming that the QD dimensions are much larger than the semiconductor unit cell, meaning that the *effective mass approximation* can be employed. Within the parabolic band approximation, it reads:

$$\left[-\frac{\hbar^2}{2m^*}\nabla^2 + U(\boldsymbol{r})\right]\Psi(\boldsymbol{r}) = E\Psi(\boldsymbol{r}) \tag{2.1}$$

where $\hbar$ is the reduced Planck constant, m^* is the electron or hole effective mass, $U(\boldsymbol{r})$ is the confinement potential for electrons and holes (three-dimensional since we are considering a zero-dimensional heterostructure). $\Psi(\boldsymbol{r})$ is the electron or hole single-particle wavefunction and E represents the energy eigenvalue.
The previous assumption regarding the dimensions of the QD with respect to those of the semiconductor unit cell also allows us to factorize the wavefunction $\Psi(\boldsymbol{r})$ in two terms, one referring to the slowly varying envelope functions $\varphi(\boldsymbol{r})$ and another one referring to the Block functions u (evaluated near the edge of the band, where $\boldsymbol{k} \simeq 0$):

$$\Psi(\boldsymbol{r}) = \varphi(\boldsymbol{r})u(\boldsymbol{k} \simeq 0, \boldsymbol{r}) \tag{2.2}$$

With wavefunctions in this formulation, the equation (2.1) can be rewritten for the electron or hole envelope functions:

$$\left[-\frac{\hbar^2}{2m^*}\nabla^2 + U(\boldsymbol{r})\right]\varphi(\boldsymbol{r}) = E\varphi(\boldsymbol{r}) \tag{2.3}$$

As explained in [16], in order to retrieve analytically the QD wavefunctions, it is necessary to switch from a set of Cartesian coordinates (x, y, z) to a set of cylindrical coordinates (x, r, θ). This strategy is enabled by the fact that, according to [18], we can assume that a lens-shaped QD with radius significantly larger than its height has a weak confinement in the in-plane directions r and θ (harmonic potential) and a strong confinement in the growth direction x (infinitely high potential well). Within these hypotheses, according to [16], the potential in cylindrical coordinates becomes $U(x, r, \theta) = \frac{1}{2}\, m^*\omega^2 r^2 + U_x(x)$. At this point, it is possible to factorize the electron and hole envelope functions of Equation (2.3) with an in-plane function $\phi(r, \theta)$ and a transverse one $\xi(x)$; these functions also allow us to separate Equation

(2.3) in a set of two independent eigenvalue equations:

$$\left[-\frac{\hbar^2}{2m^*}\frac{d}{dx} + U_x(x)\right]\xi(x) = E_n\xi(x) \tag{2.4a}$$

$$\left[-\frac{\hbar^2}{2m^*}\left(\frac{\partial^2}{\partial r^2} + \frac{1}{r}\frac{\partial}{\partial r} + \frac{1}{r^2}\frac{\partial^2}{\partial\theta^2}\right) + \frac{1}{2}m^*\omega^2 r^2\right]\phi(r,\theta) = (E - E_n)\phi(r,\theta) \tag{2.4b}$$

Since the potential in the growth direction x was assumed to be an infinitely high well, it is reasonable to expect a solution for Equation (2.4a) in the typical form for this kind of problems [15]:

$$\xi(x) = \sqrt{\frac{2}{L_w}}\sin\left(\frac{n\pi x}{L_w}\right) \tag{2.5}$$

where $n \in \mathbb{N}$ and where L_w is the width of the potential well. The energy eigenvalues will be consequently discretized and written as

$$E_n = \frac{\hbar^2\pi^2 n^2}{2m^* L_w^2} \tag{2.6}$$

Instead, the solution of the in-plane eigenvalue equation (2.4b) for electrons and holes, as explained in [16], is in the form of Fock-Darwin eigenstates:

$$\phi^{p,m}(r,\theta) = \phi_0\exp(jm\theta)\exp\left(-\frac{1}{2}\frac{m^*\omega}{\hbar}r^2\right)\left(\sqrt{\frac{m^*\omega}{\hbar}}r\right)^{|m|}\mathcal{L}_p^{|m|}\left(\frac{m^*\omega}{\hbar}r^2\right) \tag{2.7}$$

where ϕ_0 is a normalization constant, $\mathcal{L}_p^{|m|}$ are the generalized Laguerre polynomials, index $m \in \mathbb{Z}$ is the angular momentum quantum number and index $p \in \mathbb{W}$ is the radial quantum number.
Considering once again the assumption that the height of the QD is significantly smaller than its radius, it is possible to state that only the fundamental transverse energy eigenvalue has a non-negligible contribution. Therefore, the energy eigenvalues for the complete system result to be discrete and in the following form, according to [3]:

$$E_{p,m} = E_1 + \hbar\omega(2p + |m| + 1) \tag{2.8}$$

It is possible to recognize the various discrete levels, characterised by different sets of quantum numbers:

- Ground state (GS), with quantum numbers (0,0);
- First excited state (ES1), with quantum numbers $(0, \pm 1)$;
- Second excited state (ES2), with quantum numbers $(0, \pm 2)$ and (1,0).

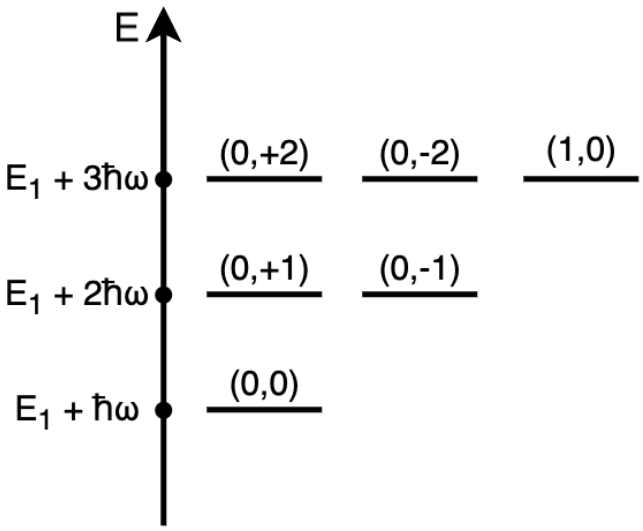

Figure 2.2. Representation of the QD energy eigenvalues of Equation (2.8).

Considering Pauli's exclusion principle, it is possible to say that the ground state has a two-fold degeneracy ($\mu_{GS} = 2$), since it is able to host two carriers with opposite spin. Analogously, we can also say for the same reason that the first excited state has a four-fold degeneracy ($\mu_{ES_1} = 4$), while the second excited state has a six-fold degeneracy ($\mu_{ES_2} = 6$). A graphical representation of said energy eigenvalues is reported in Figure 2.2. In addition to these three main levels, Equation (2.8) yields also infinitely-many equally-spaced eigenstates at progressively high energies. In reality, this model is valid only at low energies, since, at high energy, the eigenstate confinement is progressively reduced, causing the levels to become more degenerate and to be closer to each other.

In real-world quantum dots, progressing towards higher energies, the discrete levels transition to a continuum of quantum well-like states belonging to the so-called *wetting layer* (WL) and, eventually, to the 3D bulk-like states of the *separate confined heterostructure* (SCH). Of course, there will be transitions from and to these states, with their own characteristic times. Notice that, for instance, the set of SCH states is actually exploited in order to inject carriers in the QD from the external environment, since, otherwise, it would not be possible to access the confined discrete states of the QD itself. Basically, the carriers are injected there with a certain efficiency and then they progressively relax towards the lower energy levels according to the characteristic escape and capture times of the various levels. In Figure 2.3, it is possible to appreciate a schematic band structure of the QD, with the confined QD states, the WL continuum and the SCH continuum.

Not only this, as stated by [16], in real quantum dots it is possible to observe that the holes are significantly less confined with respect to the electrons. This means that the QD discrete energy levels in valence band are characterised by a smaller

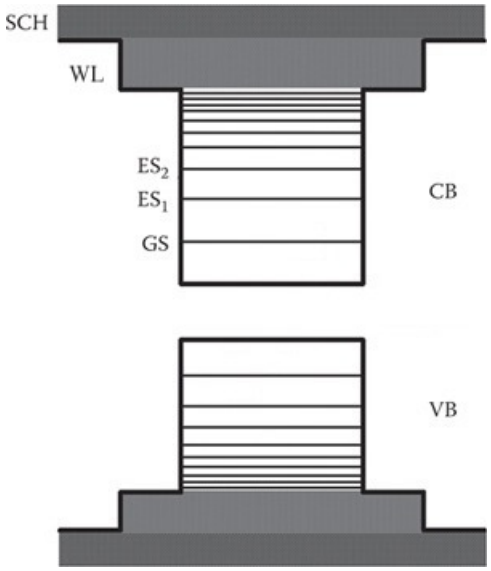

Figure 2.3. Schematic of a QD electronic band structure, with the continuum of WL and SCH states in gray.

energy difference with respect to those in conduction band and the continuum of WL and SCH levels in valence band can be found at lower energies.

After the analysis of the energy levels of a QD heterostructure, it is also interesting to study its density of states, since it is influencing the properties of this kind of materials. Contrary to the density of states in bulk semiconductors (with a square root profile) and in quantum wells (with a stepped profile), in the case of QDs, the density of states will be in the form presented in [15]:

$$D_{QD}(E) = 2\sum_{p,m} \delta(E - E_{p,m}) \tag{2.9}$$

where $E_{p,m}$ are the quantum dot discrete levels. In Figure 2.4, the densities of states for the various heterostructures are reported.

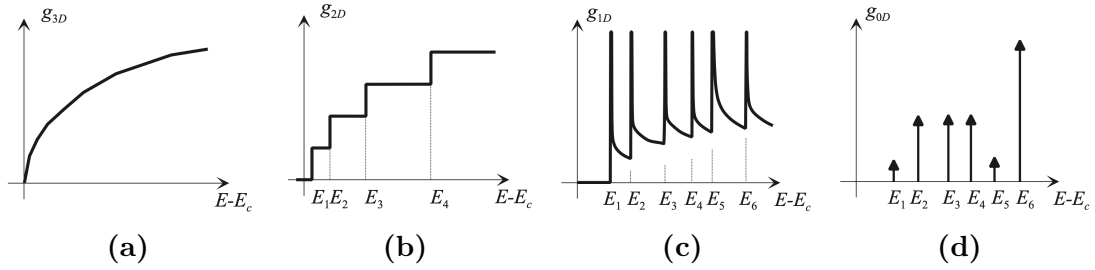

Figure 2.4. (a) Bulk DOS. (b) Quantum well DOS. (c) Quantum wire DOS. (d) Quantum dot DOS. All taken from reference [11].

2.2 Fabrication techniques

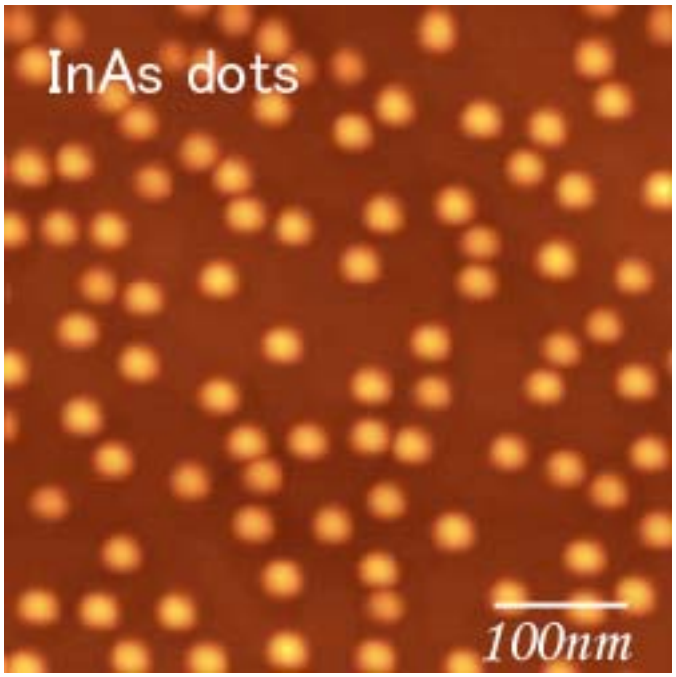

Figure 2.5. AFM image of InAs QDs on GaAs substrate. Taken from reference [25].

After the review of the most important electronic properties of QD of the previous one, in this section the main fabrication techniques for QD active materials will be shortly discussed as well. The so-called *Molecular Beam Epitaxy* (MBE) technique is for sure the most important and employed one. MBE is comprehensively described in [10].
First, let's consider two materials that are fairly lattice-mismatched, for instance InAs and GaAs (with a 7% lattice mismatch). Starting from a GaAs substrate, the InAs is deposited with a 2D layer-by-layer mechanism. Due to the mismatch between the two compounds, the deposited InAs layers will result to be strained. The strained layers form the wetting layer. This strained deposition carries on until a certain critical amount of material (*critical coverage* θ_c) is reached: at this point, the 2D layer-by-layer mechanism is naturally substituted by the formation of pyramid-shaped islands. Those are usually characterised by a nanometric size, even though their features can vary appreciably depending on the growth parameters. In Figure 2.5, it is possible to appreciate an atomic force microscopy (AFM) image of some InAs QDs grown on a GaAs substrate. Of course, not all QDs will be characterised by the same size, but they will have Gaussian-distributed sizes, according to the Gaussian distribution related to the inhomogeneous broadening,

reported in [17]:

$$G_i = \frac{1}{Z} \exp\left(-4 \ln 2 \frac{(\hbar \Delta\omega_i)^2}{\Delta E^2}\right) \tag{2.10}$$

where Z is an appropriate normalization constant that grants $\sum_i G_i = 1$, $\Delta\omega_i$ is the angular frequency difference between the one of the i-th level and the reference and ΔE is the Full Width Half Maximum of the Gaussian distribution. This also modifies the properties of the QDs, leading for instance to a non-delta DOS and to non-monochromatic emission for QD-based lasers.

The growth of the self-assembled pyramid-shape islands above the 2D wetting layer is called *Stranski-Krastanov growth*. As pointed out by [10], the Stranski-Krastanov growth onsets due to the relaxation of elastic energy, but it doesn't cause dislocations at the interfaces between the mismatched materials.

After the QD layer growth, it is common to have the deposition of a capping layer. It has been proved that the emission wavelength can be tuned by changing the characteristics of this capping layer [16].

Chapter 3

TDTW model theory

After the analysis of the main QD electronic properties and QD fabrication techniques carried out in the previous one, in this chapter, the focus will be on the time-domain travelling-wave (TDTW) model. In particular, travelling wave equations describing the evolution of the field and rate equations describing carrier dynamics will be expressed. Finally, we will write down the time stepped solution of field propagation equations. These equations are the foundations for the TDTW MATLAB program that will be used for the simulation of the device of Figure 1.1. The time-domain travelling-wave method is of utmost importance for the simulation of devices like optical amplifiers and lasers. It consists in the solution of the differential equations describing the evolution of the system by means of a finite difference scheme. Basically, the device under test is subdivided in slices with constant length and, for each time step, we compute the evolution of the field inside each slice. This method is clearly quite computational-heavy, but, for some simulations, it is the only scheme that allows us to retrieve reasonable results, for instance in the case of the double-pass configuration for the SOA under test.

3.1 Travelling wave equations

First and foremost, it is possible to express the optical field inside the active material of the device exploiting the so-called *slowly varying envelope approximation* (SVEA) that consists in expressing it as the product between a rapidly varying term and a slowly varying term. The formula of this field is the following:

$$\vec{E} = \hat{e}\phi(x,y)\left[E^{+}(z,t)e^{-jk_0 z} + E^{-}(z,t)e^{+jk_0 z}\right]e^{+j\omega_0 t} \tag{3.1}$$

where $\phi(x,y)$ is the transverse mode profile, ω_0 is the reference frequency, k_0 is the wave number related to the reference frequency ($k_0 = \omega_0/v_g$, where $v_g = c/n_{eff}$ is the group velocity in the dielectric medium) and $E^{\pm}$ are the slowly varying envelopes for the forward and backward travelling waves. The SVEA can be

considered valid if one assumes to have negligible second order time and space derivatives with respect to the first order ones, namely if:

$$\left|\frac{\partial^2 E^{\pm}}{\partial t^2}\right| \ll \left|\omega_0 \frac{\partial E^{\pm}}{\partial t}\right| \tag{3.2a}$$

$$\left|\frac{\partial^2 E^{\pm}}{\partial z^2}\right| \ll \left|k_0 \frac{\partial E^{\pm}}{\partial z}\right| \tag{3.2b}$$

Within the assumption of the validity of the SVEA, the evolution of $E^{\pm}$ in space and time will be described by the two following wave equations [17]:

$$\frac{1}{v_g}\frac{\partial E^{\pm}}{\partial t} \pm \frac{\partial E^{\pm}}{\partial z} = -\frac{1}{2}(\alpha_i^{\pm} + \alpha_p)E^{\pm}(z,t) - j\frac{\omega_0 \Gamma_{xy}}{2cn_{eff}\epsilon_0}P^{\pm}(z,t) + S_{sp}^{\pm}(z,t) \tag{3.3}$$

where $\alpha_i^{\pm}$ are the forward and backward components of the intrinsic waveguide losses, α_p are the plasma losses, ϵ_0 is the dielectric permittivity in vacuum, Γ_{xy} is the field confinement factor in the active layers, $P^{\pm}(z,t)$ are the slowly varying envelopes of the macroscopic polarization describing the stimulated response of the active layers and $S_{sp}^{\pm}(z,t)$ describes the spontaneous emission as a random noise source.
Similarly to any other partial differential equation, the travelling wave equation (3.3) requires *boundary conditions* as well. In this case, according to [6], we only have spurious residual reflectivities at the facets of the device and an efficiency term for the external optical source. In the double pass configuration, we have also to take into account a term for the external cavity mirror.

$$E^{+}(0,t) = r_0 E^{-}(0,t) + \sqrt{1-r_0^2}E_{inj}(t) \tag{3.4}$$

$$E^{-}(L,t) = r_L E^{+}(L,t) + (1-r_L^2)r_{ext}E^{+}(L,t-\tau_{ext}) \tag{3.5}$$

where r_0 and r_L are the previously-mentioned spurious reflectivities of the SOA, $E_{inj}(t)$ is the externally injected optical field, r_{ext} is the reflectivity of the external mirror for the double pass configuration and τ_{ext} is the external cavity propagation delay. The same model for boundary conditions can be employed to study edge-emitting QD lasers, using larger values for the facet reflectivities r_0 and r_L.

3.2 Optical response of the active medium

While in the previous section we expressed the travelling wave equations and the associated boundary conditions, in this one we will develop the model further by taking into account the optical response of the QD active medium, consisting in the macroscopic polarization $P^{\pm}(z,t)$, linked to the stimulated response, and in the spontaneous emission $S_{sp}^{\pm}(z,t)$, both appearing in (3.3).

Starting from the first one, we can say that the macroscopic polarization is the sum of the microscopic intraband polarization terms associated to the levels of inhomogeneously broadened QD groups. Indeed, in this case, we consider the inhomogeneous broadening of the QDs, which have a probability G_i (Equation (2.10)) of belonging to the i-th QD group (with $i = 1...N$). The dynamics of the microscopic polarization of the m-th level of the i-th QD group can be expressed as:

$$\frac{\partial p^{\pm}_{im}}{\partial t} = [j(\omega_{im} - \omega_0) - \Gamma]p^{\pm}_{im}(z,t) + j\frac{d^i_m}{\hbar}(2\rho_{im}(z,t) - 1)E^{\pm}(z,t) \tag{3.6}$$

where $m = GS, ES_1, ES_2$ and $i = 1, ..., N$, $\hbar\omega_{im}$ are the interband transition energies for the m-th level of the i-th group, $1/\Gamma$ is the so-called *characteristic dephasing time* of the interband transitions that leads to the homogeneous broadening, $\rho_{im}(z,t)$ are the occupation probabilities for the various states, linked to the gain $2\rho_{im}(z,t) - 1$ (assuming to have the *excitonic approximation*, that allows us to consider electrons and holes dynamics as equal to each other) and, finally, d^i_m is the dipole matrix element that can be written as [16]:

$$d^i_m = \frac{e\hbar^2}{m_0(E_m - E_{m'})} \int \varphi^*_{m'}\varphi_m \, dxdydz \times \frac{1}{\Omega_L}\int_{\Omega_L} u^*_{m'}\nabla u_m \, dxdydz \tag{3.7}$$

where E_m and $E_{m'}$ are the energy eigenvalues of the states that are involved in the intraband transition (denoted as m and m'), φ_m, $\varphi_{m'}$, u_m and $u_{m'}$ are exactly the slowly varying envelope functions and the Bloch functions of Equation (2.2) and Ω_L is the volume of the semiconductor unit cell. This dipole matrix element is basically telling whether the transition between the states m and m' can occur or not: if it is different from zero, it can take place, if it is zero (or close to zero) it cannot. In the case of a QD system, it turns out that the dipole matrix element is not zero only if the quantum numbers of the two interacting states are the same ($m' = m$), but from valence band to conduction band or vice versa.
In any case, with the microscopic polarization of Equation (3.6), we are now able to express the macroscopic one:

$$P^{\pm}(z,t) = \frac{N_D}{h_W}\sum_{i=1}^{N}\sum_{\substack{m=GS,\\ ES_1,ES_2}} G_i\mu_m d^{i*}_m p^{\pm}_{im}(z,t), \tag{3.8}$$

In order to express this equation more easily, it is necessary to compute the Fourier transform of Equation (3.6).

$$j\Omega p^{\pm}_{im}(z,\Omega) = [j(\omega_{im} - \omega_0) - \Gamma]p^{\pm}_{im}(z,\Omega) + j\frac{d^i_m}{\hbar}(2\rho_{im}(z,\Omega) - 1) * E^{\pm}(z,\Omega)$$

$$\Longrightarrow p_{im}^{\pm}(z,\Omega) = j\frac{1}{j(\Omega-\omega_{im}+\omega_0)+\Gamma}\frac{d_m^i}{\hbar}(2\rho_{im}(z,\Omega)-1) * E^{\pm}(z,\Omega) \tag{3.9}$$

where the symbol $*$ represents a convolution operation.
Now, we have to compute Fourier transform of the macroscopic polarization of (3.8) and then substitute (3.9) in it.

$$\begin{aligned} P_{im}^{\pm}(z,\Omega) &= \frac{N_D}{h_W}\sum_{i=1}^{N}\sum_{m} j\frac{G_i\mu_m}{\hbar}\frac{d_m^{i*}d_m^i}{j(\Omega-\Delta\omega_{im})+\Gamma}(2\rho_{im}(z,\Omega)-1) * E^{\pm}(z,\Omega) \\ &= j\frac{N_D}{h_W}\sum_{i=1}^{N}\sum_{m}\frac{G_i\mu_m|d_m^i|^2}{\hbar\Gamma}\left\{\frac{1}{1+j\frac{\Omega-\Delta\omega_{im}}{\Gamma}}\right\}(2\rho_{im}(z,\Omega)-1) * E^{\pm}(z,\Omega) \end{aligned} \tag{3.10}$$

The term between curly brackets in (3.10) is basically the Fourier transform of a complex Lorentzian function centered in $\Delta\omega_{im}$, whose anti-transform is an exponential $\mathscr{L}_{im}(t) = \Gamma\exp(j\Delta\omega_{im}t)\exp(-\Gamma t)$. This means that the factor $(2\rho_{im}(z,\Omega)-1) * E^{\pm}(z,\Omega)$ is filtered by this complex Lorentzian function. Back to the time domain, this concept can be expressed as a convolution product between the Lorentzian function and the term $(2\rho_{im}(z,t)-1)E^{\pm}(z,t)$:

$$\mathscr{L}_{im}(t) * \{(2\rho_{im}-1)E^{\pm}\} = \int_{-\infty}^{t}\Gamma e^{j\Delta\omega_{im}(t-\tau)}e^{-\Gamma(t-\tau)}(2\rho_{im}(z,\tau)-1)E^{\pm}(z,\tau)d\tau \tag{3.11}$$

This term of course will appear in the macroscopic polarization $P^{\pm}(z,t)$.
As pointed out by [17], it is possible to say that the system has a memory limited to a past interval of time of few hundreds of femtoseconds, because the macroscopic polarization is depending only on the past evolution of ρ_{im} and $E^{\pm}$ on a limited span of time of duration corresponding to the characteristic dephasing time $1/\Gamma \sim 100\,\text{fs}$. This basically leads to the so-called *adiabatic approximation*, that assumes that the occupation probability of the QD states ρ_{im} is much slower than $1/\Gamma$, allowing us to take it out from the integral of (3.11). Therefore,

$$\mathscr{L}_{im}(t) * \{(2\rho_{im}-1)E^{\pm}\} = (2\rho_{im}(z,t)-1)\int_{-\infty}^{t}\Gamma e^{j\Delta\omega_{im}(t-\tau)}e^{-\Gamma(t-\tau)}E^{\pm}(z,\tau)d\tau \tag{3.12}$$

where the remaining integral can be interpreted as the forward and backward field components filtered by a Lorentzian function. Let's denote this convolution integral as $I_{im}^{\pm}(z,t)$:

$$I_{im}^{\pm}(z,t) = \mathscr{L}_{im}(t) * E^{\pm}(z,t) \tag{3.13}$$

All things considered, the macroscopic polarization term of (3.3) results to be:

$$-j\frac{\omega_0\Gamma_{xy}}{2cn_{eff}\epsilon_0}P^{\pm}(z,t)=\sum_{i=1}^{N}\sum_{m}g_{im}^{0}(2\rho_{im}(z,t)-1)I_{im}^{\pm}(z,t) \tag{3.14}$$

where g_{im}^{0} contains the various constants:

$$g_{im}^{0}=\frac{\Gamma_{xy}G_i\mu_m|d_m^i|^2\omega_0N_D}{2cn_{eff}\epsilon_0\hbar\Gamma h_W}=\frac{\Gamma_{xy}G_iN_D}{2\pi\hbar\Gamma h_W}A_m \tag{3.15}$$

Now that the polarization response of the system is fully characterised, it is also necessary to model the spontaneous emission random noise source. Assuming that the spontaneous emission rate (per unit volume) R_{im}^{sp} from the QD confined states is in a form similar to that presented in [5],

$$R_{im}^{sp}(z,t)=\frac{N_DG_1\mu_m}{h_W}\frac{\rho_{im}(z,t)}{\tau_m^{sp}} \tag{3.16}$$

where τ_m^{sp} is the spontaneous emission characteristic time from the m-th state, we are able to write the spontaneously emitted power (per unit volume) as [17]:

$$\begin{aligned}|S_{sp}^{\pm}(z,\Omega)|^2&=\sum_{i=1}^{N}\sum_{m}|S_{im,sp}^{\pm}(z,\Omega)|^2=\\&=\frac{\beta_{sp}}{2}N_lWh_W\sum_{i=1}^{N}\sum_{m}R_{im}^{sp}(z,t)\frac{\hbar\omega_{im}}{\pi\Gamma}|\mathscr{L}_{im}(\Omega)|^2=\\&=\frac{\beta_{sp}}{2}N_DN_lW\sum_{i=1}^{N}\sum_{m}G_i\mu_m\frac{\rho_{im}(z,t)}{\tau_m^{sp}}\frac{\Gamma}{\pi}\frac{\hbar\omega_{im}}{\Gamma^2+(\Omega-\Delta\omega_{im})^2}\end{aligned} \tag{3.17}$$

where N_l is the number of QD layers, β_{sp} is the coupling factor between the spontaneously emitted noise and the transverse mode profile of the waveguide and W is the ridge waveguide width. The time domain contribution to (3.3) results to be in the form:

$$S_{sp}^{\pm}(z,t)dz=\sum_{i=1}^{N}\sum_{m}\sqrt{\frac{\hbar\omega_{im}\beta_{sp}}{2\pi\Gamma}B\frac{N_{im}(z,t)}{\tau_m^{sp}}}I_{im,sp}^{\pm}(z,t) \tag{3.18}$$

where $N_{im}(z,t)=WN_DN_lG_i\mu_m\rho_{im}(z,t)dz$ is the total number of carriers occupying the m-th state belonging to the i-th population, B is the bandwidth of the random process and $I_{im,sp}^{\pm}(z,t)$ is a convolution product between the Lorentzian function and a random phase noise $e^{j\phi_{im}^{\pm}(z,t)}$:

$$I_{im,sp}^{\pm}(z,t)=\mathscr{L}_{im}(t)*e^{j\phi_{im}^{\pm}(z,t)} \tag{3.19}$$

Now, everything is in place for the time and space discretization of (3.3) that will be used in the MATLAB program.

3.3 Time discretization of the problem

The goal of this Section consists in the formulation of a proper finite difference scheme for the travelling wave equation (3.3), that can subsequently be implemented in MATLAB for the simulations.
First and foremost, it is necessary to substitute Equations (3.13) and (3.14) in (3.3). Let $\alpha_w^{\pm} = \alpha_i^{\pm} + \alpha_p$. In this way, we obtain:

$$\begin{aligned}\frac{1}{v_g}\frac{\partial E^{\pm}}{\partial t} \pm \frac{\partial E^{\pm}}{\partial z} = &- \frac{\alpha_w^{\pm}}{2} E^{\pm}(z,t) + S_{sp}^{\pm}(z,t) - \\ &- \sum_{i=1}^{N}\sum_{m} g_{im}^{0}(2\rho_{im}(z,t)-1)[\mathscr{L}_{im}(t) * E^{\pm}(z,t)]\end{aligned} \tag{3.20}$$

In order to solve this equation more comfortably, it is of course convenient to move to the frequency domain by taking its Fourier transform, thus obtaining:

$$\begin{aligned}\pm\frac{\partial E^{\pm}}{\partial z}(z,\Omega) = &\left\{-j\frac{\Omega}{v_g} - \frac{\alpha_w^{\pm}}{2} - \sum_{i=1}^{N}\sum_{m} g_{im}^{0}(2\rho_{im}(z,\Omega)-1) * \mathscr{L}_{im}(\Omega)\right\} \cdot \\ &\cdot E^{\pm}(z,\Omega) + S_{sp}^{\pm}(z,\Omega) = \beta(z,\Omega)E^{\pm}(z,\Omega) + S_{sp}^{\pm}(z,\Omega)\end{aligned} \tag{3.21}$$

In the frequency domain, Equation (3.20) became a first-order non-homogeneous differential equation, whose general solution can be written by summing its particular solution and the general solution of the associated homogeneous equation.

$$\begin{aligned}E^{\pm}(z,\Omega) = &\exp\left\{\pm\int_{z_0}^{z} dz'\beta(z',\Omega)\right\}\Big[E^{\pm}(z_0,\Omega) + \\ &+ \int_{z_0}^{z} dz' S_{sp}^{\pm}(z',\Omega)\exp\left\{\mp\int_{z_0}^{z'} dz''\beta(z'',\Omega)\right\}\Big]\end{aligned} \tag{3.22}$$

It is now time to introduce a spatial discretization of the active material with unit step Δz, that must be small enough to allow the approximation of the integrals and the exponentials with first order expansions. This means that (3.22) approximately becomes:

$$\begin{aligned}E^{\pm}(z_0 \pm \Delta z,\Omega) &\simeq E^{\pm}(z_0,\Omega)\exp\{\beta(z_0,\Omega)\Delta z\} + S_{sp}^{\pm}(z_0,\Omega)\Delta z = \\ &= S_{sp}^{\pm}(z_0,\Omega)\Delta z + E^{\pm}(z_0,\Omega)\exp\left\{-j\frac{\Omega}{v_g}\right\}\exp\left\{-\frac{\alpha_w^{\pm}\Delta z}{2} + \right. \\ &\left. + \Delta z\sum_{m} g_{im}^{0}(2\rho_{im}(z_0,\Omega)-1) * \mathscr{L}_{im}(\Omega)\right\} \simeq \\ &\simeq S_{sp}^{\pm}(z_0,\Omega)\Delta z + E^{\pm}(z_0,\Omega)\exp\left\{-j\frac{\Omega}{v_g}\right\}\left\{1 - \frac{\alpha_w^{\pm}\Delta z}{2} + \right. \\ &\left. + \Delta z\sum_{m} g_{im}^{0}(2\rho_{im}(z_0,\Omega)-1) * \mathscr{L}_{im}(\Omega)\right\}\end{aligned} \tag{3.23}$$

For the goal of simulating devices, we ought to introduce a time discretization as well. In this case, we use $\Delta t = \Delta z / v_g$. With this, coming back to the time domain, we get the final time-stepped solution of the travelling wave equation, where the field depends on its value in the previous time step:

$$\begin{aligned} E^{\pm}(z_0 \pm \Delta z, t) = &+ S^{\pm}_{sp}(z_0, t) + E^{\pm}(z_0, t - \Delta t) - \frac{\alpha^{\pm}_w}{2} E^{\pm}(z_0, t - \Delta t)\Delta z + \\ &+ \Delta z \sum_m g^0_{im}(2\rho_{im}(z_o, t - \Delta t) - 1) I^{\pm}_{im}(z_0, t - \Delta t) \end{aligned} \tag{3.24}$$

We still have to solve the convolution integral of $I^{\pm}_{im}(z,t)$ and that of $I^{\pm}_{im,sp}(z,t)$, contained in $S^{\pm}_{sp}(z,t)$. Starting from the first one, the approximate result that we obtain is [17]:

$$\begin{aligned} I^{\pm}_{im}(z,t) = &+ e^{j\Delta\omega_{im}\Delta t} e^{-\Gamma\Delta t} I^{\pm}_{im}(z, t - \Delta t) + \\ &+ \frac{\Gamma\Delta t}{2} e^{j\Delta\omega_{im}\Delta t} e^{-\Gamma\Delta t} E^{\pm}(z, t - \Delta t) + \frac{\Gamma\Delta t}{2} E^{\pm}(z,t) \end{aligned} \tag{3.25}$$

This is an important result because it means that the filtered field at the current time step depends on its value at the previous time step: this can be used in a recursive numerical implementation. With similar computations, we obtain basically the same result for $I^{\pm}_{im,sp}(z,t)$ as well:

$$\begin{aligned} I^{\pm}_{im,sp}(z,t) = &+ e^{j\Delta\omega_{im}\Delta t} e^{-\Gamma\Delta t} I^{\pm}_{im,sp}(z, t - \Delta t) + \\ &+ \frac{\Gamma\Delta t}{2} e^{j\Delta\omega_{im}\Delta t} e^{-\Gamma\Delta t} e^{j\phi^{\pm}_{im}(z, t-\Delta t)} + \frac{\Gamma\Delta t}{2} e^{j\phi^{\pm}_{im}(z,t)} \end{aligned} \tag{3.26}$$

These equations give us a complete finite difference scheme for the numerical computation of the propagating field in the device. This has to be coupled to some rate equations for the description of carriers dynamics.
One last thing that has to be discussed concerning the propagating field is the *reference frequency* ω_0.

3.3.1 Reference frequency choice

The reference frequency, which appears in many of the previous formulae and equations, can be chosen to be one of the following:

- $\omega_0 = \omega_{(N+1)/2,GS}$, central GS frequency;
- $\omega_0 = ½(\omega_{(N+1)/2,GS} + \omega_{(N+1)/2,ES_1})$, average between the central GS and central ES1 frequencies;
- $\omega_0 = ½(\omega_{(N+1)/2,GS} + \omega_{(N+1)/2,ES_2})$, average between the central GS and central ES2 frequencies.

In SOAs models, the choice is dictated by which frequencies contribute to the stimulated emission, making also sure that the SVEA is still applicable (small frequency detuning). For instance, the central GS frequency could be a good choice in order to avoid the aliasing due to the Lorentzian filter tails beyond the Nyquist frequency, but it completely fails when describing the gain spectrum or emission from the excited states.
Another idea could be to use the average between the GS and ES1 central frequencies, but in this case we have to carefully choose the simulation time step in order to avoid the aliasing and we still have the problem of the description of the stimulated emission from ES2.
For this reason, if we assume to have stimulated emission from ES2 as well (as we do), it could be convenient to work with reference frequency given by the average between the GS and ES2 central frequencies, but, in this case, the validity of the SVEA must be verified. If we consider the central energies of the various QD layers in Table 4.1 and we consider their mean for the various states, we obtain $E_{GS} = 0.9955\,\text{eV}$, $E_{ES_1} = 1.0242\,\text{eV}$ and $E_{ES_2} = 1.0510\,\text{eV}$. If we choose the average between GS and ES2 energies as reference, we get $E_0 = 1.0233\,\text{eV}$. Then, we know that the energy in eV and the wavelength in µm are related by the following formula [11]:

$$E = \frac{1.24}{\lambda|_{\mu\text{m}}}\text{eV} \tag{3.27}$$

With this equation, we obtain that the wavelengths associated to the energies reported above are $\lambda_{GS} = 1.2456\,\mu\text{m}$, $\lambda_{ES_1} = 1.2107\,\mu\text{m}$, $\lambda_{ES_2} = 1.1798\,\mu\text{m}$ and $\lambda_0 = 1.2118\,\mu\text{m}$. Finally, using $\lambda f = c$, we get that $f_{GS} = 241\,\text{THz}$, $f_{ES_1} = 248\,\text{THz}$, $f_{ES_2} = 254\,\text{THz}$ and $f_0 = 247\,\text{THz}$. This means that the relative difference between the frequencies and the reference are $\simeq 2.4\%$ for GS, $\simeq 0.4\%$ for ES1 and $\simeq 2.8\%$ for ES2.
Due to the fact that in all three cases the relative difference is very small ($< 5\%$), we can safely say that the SVEA is still valid with this choice of reference frequency. Therefore, since we are assuming that ES2 as well contributes to the emission, this reference frequency will be also implemented in the numerical simulation.

3.4 Rate equation model for carriers dynamics

Besides the evolution of the forward and backward propagating field components, we also need some rate equations for the carriers dynamics, so to have a complete description of the system.
In this Section, actually, two different rate equation models will be presented: one, more general, where electrons and holes dynamics are independent from each other (as they are in real systems) [12], one where they are considered to be equivalent (*excitonic approximation*) [13], [17].

Let's start from a general description of the model. Basically, it consists in a set of equations describing the variation of the number of carriers in a given QD confined state, taking into account all the possible mechanisms that could add or subtract carriers from this state. In particular, in this model, the following ones are taken into account, each one characterised by its own characteristic time constant describing the strength of the interaction:

- capture from another energy level, with characteristic time $\tau_{c,m}$;
- escape towards another energy level, with characteristic time $\tau_{e,m}$;
- non-radiative recombination, with characteristic time $\tau_{nr,m}$;
- spontaneous radiative recombination, with characteristic time $\tau_{sp,m}$;
- stimulated radiative recombination, with characteristic time $\tau_{st,m}$;
- Auger recombination, with characteristic time $\tau_{Aug,m}$.

Concerning the scattering processes of capture and escape, it is possible to assert that they are regulate by Pauli's exclusion principle: in order to have the mechanism, it is necessary to have an initial occupied state (probability $\rho_{im}(z,t)$) and a final free state (probability $1-\rho_{im}(z,t)$). With this in mind, we can define the rates for these phenomena using the probabilities of the two states involved in the process and the characteristic time:

$$\mathcal{R}_{c,m}(z,t) = \frac{1}{\tau_{c,m}}\rho_{im'}(z,t)(1-\rho_{im}(z,t)) \tag{3.28}$$

$$\mathcal{R}_{e,m}(z,t) = \frac{1}{\tau_{e,m}}\rho_{im}(z,t)(1-\rho_{im'}(z,t)) \tag{3.29}$$

Equation (3.28) represents the capture rate for a reference state m of a carrier coming from a state m'; Equation (3.29) represents the escape rate for a reference state m of a carrier escaping towards a state m'. Note that these two mechanisms do not only involve the QD confined states but also SCH (escape towards WL, capture from WL) and WL (escape towards SCH and ES2, capture from SCH and ES2).
Concerning the non-radiative recombination processes, they are basically trap-assisted recombination phenomena involving trap levels located in the semiconductor bandgap, that can interact with the carriers in the QD states. They involve just a single carrier, therefore they can be modelled with the following equation:

$$\mathcal{R}_{nr,m}(z,t) = \frac{\rho_{im}(z,t)}{\tau_{nr,m}} \tag{3.30}$$

Since only one carrier is involved, it is reasonable to expect a single probability function in Equation (3.30).

Spontaneous emission of course involves an electron and a hole that spontaneously recombine, emitting a photon. This means that the spontaneous recombination rate can be modelled simply with the existence probabilities of a hole and an electron (in the independent model $\rho^h_{im}(z,t)$ and $\rho^e_{im}(z,t)$, respectively) and with a proper phenomenological characteristic time. All in all, the radiative spontaneous recombination rate can be written as:

$$\mathcal{R}_{sp,m}(z,t) = \frac{1}{\tau_{sp,m}} \rho^e_{im}(z,t)\rho^h_{im}(z,t) \tag{3.31}$$

Finally, Auger recombination is another type of non-radiative recombination that involves three different carriers. It consists in the recombination of an electron-hole pair that transfer the transition energy to another carrier, either electron or hole. A rigorous model for these processes can be found in [4]. In this case, we have a rate equation containing a contribution due to the electron-hole-electron interaction, but also another one due to the dual process electron-hole-hole:

$$\mathcal{R}^e_{Aug,m}(z,t) = \frac{1}{\tau^e_{Aug,m}} (\rho^e_{im})^2 \rho^h_{im} + \frac{1}{2} \frac{1}{\tau^h_{Aug,m}} (\rho^h_{im})^2 \rho^e_{im} \tag{3.32a}$$

$$\mathcal{R}^h_{Aug,m}(z,t) = \frac{1}{\tau^h_{Aug,m}} (\rho^h_{im})^2 \rho^e_{im} + \frac{1}{2} \frac{1}{\tau^e_{Aug,m}} (\rho^e_{im})^2 \rho^h_{im} \tag{3.32b}$$

In the last term of both (3.32a) and (3.32b) a factor ½, due to the fact that the last term is not related to the reference carrier (electrons for (3.32a), holes for (3.32b)). In reality, the model can be simplified by neglecting the second term of both equations:

$$\mathcal{R}^e_{Aug,m}(z,t) = \frac{1}{\tau^e_{Aug,m}} (\rho^e_{im})^2 \rho^h_{im} \tag{3.33a}$$

$$\mathcal{R}^h_{Aug,m}(z,t) = \frac{1}{\tau^h_{Aug,m}} (\rho^h_{im})^2 \rho^e_{im} \tag{3.33b}$$

Note also that these two equations will coincide in the excitonic model, since we make the assumption that $\rho^h_{im} = \rho^e_{im}$.

At this point, we are ready to write the rate equation model. This will be done both with a more general approach, considering independent holes and electrons dynamics ($\rho^h_{im} \neq \rho^e_{im}$), and with the excitonic approximation, in which instead we assume to have the same dynamics for the two populations ($\rho^h_{im} = \rho^e_{im} \triangleq \rho_{im}$).

3.4.1 Independent rate equation model

In this case, due to the fact that the electrons and holes dynamics are independent, we have two separate sets of rate equations that have to be computed. Of course, we

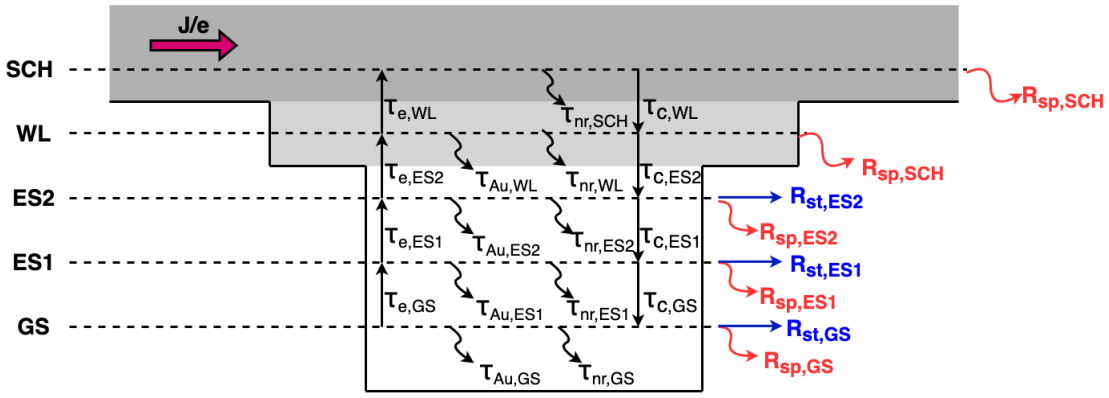

Figure 3.1. Schematic representation of all possible scattering and recombination phenomena between the various states of the conduction band of the i-th QD.

have a pair of equations for each one of the considered energy levels (SCH, WL, ES2, ES1, GS). In theory, we could have captures and escapes towards each state and from each state, but, for the sake of simplicity, let's assume that only levels that are adjacent in energy can interact. Let's also assume that the WL can interact with all the QD layers and populations and that the external current is injected in the system through the SCH (with a certain injection efficiency η_i). Furthermore, let's assume that all the levels provide a spontaneous emission contribution, however only the confined QD states (ES2, ES1, GS) provide a stimulated emission contribution. In this case we will also consider non-radiative recombination for all the states, but Auger recombination (in the formulation of (3.32a) and (3.32b)) only for the confined QD states and for the WL.
Within these assumptions, we can write five electron rate equations and five hole rate equations (in this case written at the same time for the sake of brevity):

$$\begin{aligned}\frac{\partial N_{SCH}^{e/h}}{\partial t} = &+\eta_i \frac{J}{e} W - \frac{N_{SCH}^{e/h}}{\tau_{c,WL}^{e/h}} + \frac{N_{WL}^{e/h}}{\tau_{e,WL}^{e/h}} - \\ &- \frac{B_{SCH}}{W h_{SCH}} N_{SCH}^{e} N_{SCH}^{h} - \frac{N_{SCH}^{e/h}}{\tau_{nr,SCH}^{e/h}}\end{aligned} \tag{3.34a}$$

$$\begin{aligned}\frac{\partial N_{WL}^{e/h}}{\partial t} = &+\frac{N_{SCH}^{e/h}}{\tau_{c,WL}^{e/h}} - \frac{N_{WL}^{e/h}}{\tau_{e,WL}^{e/h}} - \frac{B_{WL}}{W h_{W}} N_{WL}^{e} N_{WL}^{h} - \\ &- \frac{N_{SCH}^{e/h}}{\tau_{nr,SCH}^{e/h}} - \frac{N_{WL}^{e} N_{WL}^{h}}{\tau_{Aug,ES_2}} N_{WL}^{e/h} - \\ &- \sum_{i=1}^{N} \frac{G_i}{\tau_{c,ES_2}^{e/h}} N_{WL}^{e/h} (1 - \rho_{iES_2}^{e/h}) + \sum_{i=1}^{N} \frac{N_{iES_2}^{e/h}}{\tau_{e,ES_2}^{e/h}}\end{aligned} \tag{3.34b}$$

$$\begin{aligned}
\frac{\partial N_{iES_2}^{e/h}}{\partial t} &= +\frac{G_i}{\tau_{c,ES_2}^{e/h}} N_{WL}^{e/h}(1-\rho_{iES_2}^{e/h}) - \frac{N_{iES_2}^{e/h}}{\tau_{e,ES_2}^{e/h}} - \\
&- \frac{N_{iES_2}^{e/h}}{\tau_{c,ES_1}^{e/h}}(1-\rho_{iES_1}^{e/h}) + \frac{N_{iES_1}^{e/h}}{\tau_{e,ES_1}^{e/h}}(1-\rho_{iES_2}^{e/h}) - \frac{N_{iES_2}^{e}\rho_{iES_2}^{h}}{\tau_{sp,ES_2}} - \\
&- \frac{\rho_{iES_2}^{e}\rho_{iES_2}^{h}}{\tau_{Aug,ES_2}}\left(N_{iES_2}^{e/h} + \frac{1}{2}N_{iES_2}^{h/e}\right) - \frac{N_{iES_2}^{e/h}}{\tau_{nr,ES_2}^{e/h}} - \mathcal{R}_{st,iES_2}
\end{aligned} \tag{3.34c}$$

$$\begin{aligned}
\frac{\partial N_{iES_1}^{e/h}}{\partial t} &= +\frac{N_{iES_2}^{e/h}}{\tau_{c,ES_1}^{e/h}}(1-\rho_{iES_1}^{e/h}) - \frac{N_{iES_1}^{e/h}}{\tau_{e,ES_1}^{e/h}}(1-\rho_{iES_2}^{e/h}) - \\
&- \frac{N_{iES_1}^{e/h}}{\tau_{c,GS}^{e/h}}(1-\rho_{iGS}^{e/h}) + \frac{N_{iGS}^{e/h}}{\tau_{e,GS}^{e/h}}(1-\rho_{iES_1}^{e/h}) - \frac{N_{iES_1}^{e}\rho_{iES_1}^{h}}{\tau_{sp,ES_1}} - \\
&- \frac{\rho_{iES_1}^{e}\rho_{iES_1}^{h}}{\tau_{Aug,ES_1}}\left(N_{iES_1}^{e/h} + \frac{1}{2}N_{iES_1}^{h/e}\right) - \frac{N_{iES_1}^{e/h}}{\tau_{nr,ES_1}^{e/h}} - \mathcal{R}_{st,iES_1}
\end{aligned} \tag{3.34d}$$

$$\begin{aligned}
\frac{\partial N_{iGS}^{e/h}}{\partial t} &= +\frac{N_{iES_1}^{e/h}}{\tau_{c,GS}^{e/h}}(1-\rho_{iGS}^{e/h}) - \frac{N_{iGS}^{e/h}}{\tau_{e,GS}^{e/h}}(1-\rho_{iES_1}^{e/h}) - \frac{N_{iGS}^{e}\rho_{iGS}^{h}}{\tau_{sp,GS}} - \\
&- \frac{\rho_{iGS}^{e}\rho_{iGS}^{h}}{\tau_{Aug,GS}}\left(N_{iGS}^{e/h} + \frac{1}{2}N_{iGS}^{h/e}\right) - \frac{N_{iGS}^{e/h}}{\tau_{nr,GS}^{e/h}} - \mathcal{R}_{st,iGS}
\end{aligned} \tag{3.34e}$$

There are some quantities in Equations (3.34a)-(3.34e) that have yet to be expressed explicitly. First of all, the quantities $N_{im}^{e/h}$, already appearing in (3.18), represent the total number of carriers occupying the m-th QD state belonging to the i-th population and they are in the form:

$$N_{im}^{e/h}(z,t) = W N_D N_l G_i \mu_m \rho_{im}^{e/h}(z,t)dz \tag{3.35}$$

Similarly, $N_{SCH}^{e/h}$ and $N_{WL}^{e/h}$ are the total number of carriers in the SCH and in the WL. Then, we have also to express the stimulated emission rates $\mathcal{R}_{st,im}$ for Equations (3.34c)-(3.34e). This can be done with [2]:

$$\mathcal{R}_{st,im} = j\frac{dz}{\hbar\omega_{im}}[(E^{+}{p_{im}^{+}}^{*} - E^{+*}p_{im}^{+}) + (E^{-}{p_{im}^{-}}^{*} - E^{-*}p_{im}^{-})] \tag{3.36}$$

According to [17], there must be a specific relationship between the capture and escape time of the various energy levels, in order to guarantee the recovery of a

quasi-equilibrium energy distribution without any external perturbation:

$$\frac{\tau_{e,WL}^{e/h}}{\tau_{c,WL}^{e/h}} = \frac{D_{WL}N_l}{D_{SCH}h_{SCH}} \exp\left(\frac{\Delta E_{SCH-WL}}{k_BT}\right) \tag{3.37a}$$

$$\frac{\tau_{e,ES_2}^{e/h}}{\tau_{c,ES_2}^{e/h}} = \frac{\mu_{ES_2}N_D}{D_{WL}} \exp\left(\frac{\Delta E_{WL-iES_2}}{k_BT}\right) \tag{3.37b}$$

$$\frac{\tau_{e,ES_1}^{e/h}}{\tau_{c,ES_1}^{e/h}} = \frac{\mu_{ES_1}}{\mu_{ES_2}} \exp\left(\frac{\Delta E_{iES_2-iES_1}}{k_BT}\right) \tag{3.37c}$$

$$\frac{\tau_{e,GS}^{e/h}}{\tau_{c,GS}^{e/h}} = \frac{\mu_{GS}}{\mu_{ES_1}} \exp\left(\frac{\Delta E_{iES_1-iGS}}{k_BT}\right) \tag{3.37d}$$

where the quantities $\Delta E_{m-m'}$, $m' \neq m$, represent the energy difference between two adjacent energy levels. The quantities D_{SCH} and D_{WL} in Equations (3.37a) and (3.37b) are, respectively, the 3D bulk-like DOS associated to the SCH and the 2D quantum well-like DOS associated to the WL. They can be expressed as follows:

$$D_{SCH} = 2\left(2\frac{\pi m_{e/h,SCH}^* k_BT}{\hbar^2}\right)^{\frac{3}{2}} \tag{3.38a}$$

$$D_{WL} = \frac{m_{e/h,WL}^* k_BT}{\pi\hbar^2} \tag{3.38b}$$

where $m_{e/h,SCH}^*$ and $m_{e/h,WL}^*$ are the electron and hole effective masses in the SCH and in the WL, respectively.

The equations that were presented here, coupled with the propagating field and the polarization equations, represent a complete set for the accurate description of the physics of this system. Albeit more accurate, the independent electron and hole rate equation model requires the solution of two sets of equation, for electrons and holes separately and this could be a disadvantage from the point of view of the computational cost.

3.4.2 Excitonic rate equation model

The excitonic model, instead, is an approximation that allows for a reduced computational cost. Basically, it relies upon the assumption that in the SCH, in the WL and in each one of the QD confined levels charge neutrality is established. This means that:

$$N_{SCH} \triangleq N_{SCH}^e = N_{SCH}^h \tag{3.39a}$$

$$N_{WL} \triangleq N_{WL}^e = N_{WL}^h \tag{3.39b}$$

$$\rho_{im} \triangleq \rho_{im}^e = \rho_{im}^h \tag{3.39c}$$

These assumptions effectively enable us to cut in half the number of rate equations to be solved. This is clearly reducing the computational cost, however the accuracy of the model is reduced as well, since, in real systems, electrons and holes do not have perfectly matching dynamics.
In any case, the assumptions regarding the scattering and recombination phenomena are the same as before (refer to the schematic of Figure 3.1). The only difference is that, now, the Auger recombination contributions are modelled using the simpler Equations (3.33a) and (3.33b).
Within these hypothesis, the excitonic rate equations become:

$$\begin{aligned}\frac{\partial N_{SCH}}{\partial t} &= +\eta_i \frac{J}{e} W - \frac{N_{SCH}}{\tau_{c,WL}} + \frac{N_{WL}}{\tau_{e,WL}} - \\ &- \frac{B_{SCH}}{W h_{SCH}} N_{SCH}^2 - \frac{N_{SCH}}{\tau_{nr,SCH}}\end{aligned} \tag{3.40a}$$

$$\begin{aligned}\frac{\partial N_{WL}}{\partial t} &= +\frac{N_{SCH}}{\tau_{c,WL}} - \frac{N_{WL}}{\tau_{e,WL}} - \frac{B_{WL}}{W h_W} N_{WL}^2 - \frac{N_{SCH}}{\tau_{nr,SCH}} - \\ &- \frac{N_{WL}^3}{\tau_{Aug,ES_2}} - \sum_{i=1}^{N} \frac{G_i}{\tau_{c,ES_2}} N_{WL}(1-\rho_{iES_2}) + \sum_{i=1}^{N} \frac{N_{iES_2}}{\tau_{e,ES_2}}\end{aligned} \tag{3.40b}$$

$$\begin{aligned}\frac{\partial N_{iES_2}}{\partial t} &= +\frac{G_i}{\tau_{c,ES_2}} N_{WL}(1-\rho_{iES_2}) - \frac{N_{iES_2}}{\tau_{e,ES_2}} - \\ &- \frac{N_{iES_2}}{\tau_{c,ES_1}}(1-\rho_{iES_1}) + \frac{N_{iES_1}}{\tau_{e,ES_1}}(1-\rho_{iES_2}) - \\ &- \frac{N_{iES_2}\rho_{iES_2}}{\tau_{sp,ES_2}} - \frac{\rho_{iES_2}^2}{\tau_{Aug,ES_2}} N_{iES_2} - \frac{N_{iES_2}}{\tau_{nr,ES_2}} - \mathcal{R}_{st,iES_2}\end{aligned} \tag{3.40c}$$

$$\begin{aligned}\frac{\partial N_{iES_1}}{\partial t} &= +\frac{N_{iES_2}}{\tau_{c,ES_1}}(1-\rho_{iES_1}) - \frac{N_{iES_1}}{\tau_{e,ES_1}}(1-\rho_{iES_2}) - \\ &- \frac{N_{iES_1}}{\tau_{c,GS}}(1-\rho_{iGS}) + \frac{N_{iGS}}{\tau_{e,GS}}(1-\rho_{iES_1}) - \\ &- \frac{N_{iES_1}\rho_{iES_1}}{\tau_{sp,ES_1}} - \frac{\rho_{iES_1}^2}{\tau_{Aug,ES_1}} N_{iES_1} - \frac{N_{iES_1}}{\tau_{nr,ES_1}} - \mathcal{R}_{st,iES_1}\end{aligned} \tag{3.40d}$$

$$\begin{aligned}\frac{\partial N_{iGS}}{\partial t} &= +\frac{N_{iES_1}}{\tau_{c,GS}}(1-\rho_{iGS}) - \frac{N_{iGS}}{\tau_{e,GS}}(1-\rho_{iES_1}) - \\ &- \frac{N_{iGS}\rho_{iGS}}{\tau_{sp,GS}} - \frac{\rho_{iGS}^2}{\tau_{Aug,GS}} N_{iGS} - \frac{N_{iGS}}{\tau_{nr,GS}} - \mathcal{R}_{st,iGS}\end{aligned} \tag{3.40e}$$

Then, we have also to consider the fact that we have different QD populations associated to the chirped layer. This must be taken into account by means of a summation on the index i for the three QD discrete states.
These are the equations that will be directly implemented in MATLAB for the simulations of the device. The rate equations that have been presented here are

just time-variations of the carriers populations in each one of the QD energy levels: in a numerical implementation, therefore, we have to compute the variations with respect to the total number of carriers in each energy level, in the previous time instant of the simulation and, then, to sum these to the total populations themselves.

Chapter 4

Device and Experimental setup

In the previous chapter, the foundations for the time-domain travelling-wave model that will be implemented in MATLAB were laid down. In this new chapter, instead, we will discuss more about the device of [7], fabricated by III-V Labs, and the experimental setup employed by the Heriot-Watt University group in that article.

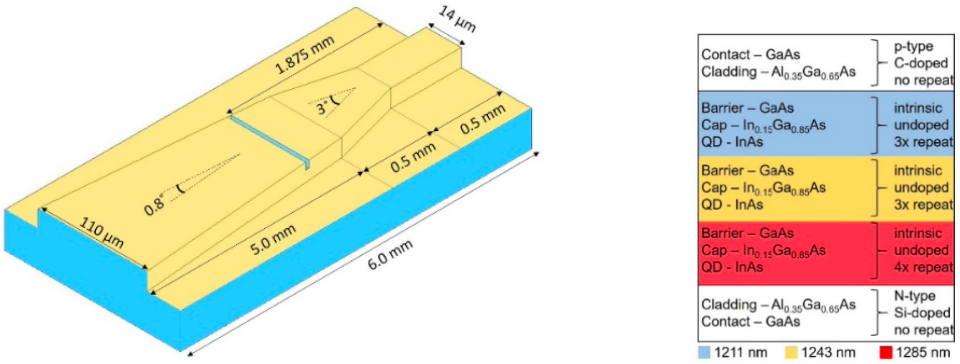

(a) **(b)**

Figure 4.1. (a) Structure of the device under test. (b) Composition of the QD layers of the device. Both images taken from reference [7].

Figure 4.2. Picture of the real device. The red arrows indicate the position of the insulation trench. Taken from reference [8].

4.1 Optical amplifier

Figure 4.1a shows a schematic of the device. In total, it is 6 mm long and it has three distinct sections: a 0.5 mm long straight ridge waveguide section (rear of the device), a 5 mm long tapered section, with full taper angle of 3°, and, finally, a 5 mm long tapered section, with full taper angle of 0.8° (front of the device). Therefore, we have that the front facet of the device has width of 110 µm, whereas the rear one has width of 14 µm. The tapered structure is important because it allows us to modify how light is guided through the device and it results in an enhanced output power. At 1.875 mm from the rear facet, a trench has been etched in the waveguide in order to form two electrically insulated contacts that can be biased independently for better versatility of the biasing conditions. Moreover, a shallow ridge was also etched into the GaAs contact layer, in order to introduce a slight index guiding and in order to achieve enhanced gain and better beam quality from the front facet, as pointed out by [7].
From Figure 4.2, which represents a picture of the actual device, it is also possible to appreciate the fact that the front and rear facets have a 7° angle with respect to the SOA waveguide. The facets are coated by an anti-reflection coating, in order to reduce as much as possible the reflectivity, thus suppressing lasing and optimizing the output. The system is kept at a fixed temperature of 20 °C by means of Peltier cells.
Concerning the composition of the active material, a summary is reported in Figure 4.1b. It is basically made up of ten chirped InAs QD layers. Each one of these layers is capped by a layer of $In_{0.15}Ga_{0.75}As$ and separated by a layer of GaAs. Above the structure we have also an $Al_{0.35}Ga_{0.65}As$ cladding and a p-doped GaAs layer representing the p-type contact; below the structure, likewise, we have an $Al_{0.35}Ga_{0.65}As$ cladding and a n-doped GaAs layer representing the n-type contact. The fact that the QD layers are *chirped* means that their GS emission wavelength is not perfectly matched. In particular, they can be subdivided as follows:

- 3 layers with GS target emission wavelength of $\lambda_{GS} = 1211$ nm (closest to p-contact);
- 3 layers with GS target emission wavelength of $\lambda_{GS} = 1243$ nm;
- 4 layers with GS target emission wavelength of $\lambda_{GS} = 1285$ nm (closest to n-contact).

As explained by [7], this chirp of the active material was introduced in order to broaden the gain spectrum bandwidth, exploiting their separate, detuned gain spectra.
In Table 4.1, some other physical parameters of the device are reported. These are the parameters that were employed in the models of [9]. For instance, note that

Symbol	Description	Value
η	Injection efficiency	0.65
N_l	Number of QD layers	4 + 3 + 3
μ_m	Degeneracy for GS, ES1, ES2	2 - 4 - 6
E_{iGS}	GS transition energies	1.0239-0.9976-0.9650 eV
E_{iES_1}	ES1 transition energies	1.0500-1.0265-0.9960 eV
E_{iES_2}	ES2 transition energies	1.0690-1.0508-1.0333 eV
E_{WL}	WL transition energy	1.1 eV
ΔE	FWHM homo. broad.	35 eV
N_D	QD surface density	$400\,\mu m^2$
g_i	GS, ES1, ES2 maximum gain	690 - 750 - 700 cm^{-1}
$\alpha^{\pm}$	Propagation losses	1.35 (+), 3.60 (-) cm^{-1}
K_p	Plasma losses coefficient	$1 \times 10^{-17}\,cm^2$
$\tau_{c,m}$	Capture times from GS, ES1, ES2, WL	1 - 5 - 5 - 12 ps
$\tau_{nr,m}$	Non-rad. times from GS, ES1, ES2, WL	10 ns
$\tau_{Aug,m}$	Auger times from GS, ES1, ES2, WL	0.44 - 2.2 - 3.3 - 10^{50} ns
h_{QD}	QD height	5 nm
h_{WL}	WL height	8 nm
h_{SCH}	SCH height	647 nm
n_r	Effective index	3.3445

Table 4.1. Physical parameters of the SOA, also used in the numerical simulations [9].

the propagation losses have two values, one for the forward propagation, one for the backward propagation. This was backed by the experimental evidences of the rear facet power being lower than the front facet one. The same is actually true for the confinement factor in the y direction Γ_y. It is also interesting to note that Γ_y changes in the propagation direction z, as it is possible to predict from the fact that the waveguide is not perfectly straight. The weak guiding and the tapering of the waveguide lead to an asymmetric confinement factor for the forward and backward propagating fields, as determined with BPM simulations [9]. On the other hand, the confinement factor in the x direction Γ_x is assumed to be constant ($\Gamma_x = 0.127$). The dependency of Γ_y on z will be discussed further in the next chapter.

In reality, since the models employed in that article are slightly different from the one that was employed in this work, some of the parameters had to be slightly adjusted in order to get good accordance with experimental results. This shouldn't be a problem, because the parameters in Table 4.1 were mostly obtained by fitting the sets of experimental data.

4.2 Laser source

This optical amplifier is of course used in order to amplify optical signals. During the experiments of [7], a multi-section mode-locked laser source (InAs QD active region) was used in order to produce ultrashort pulses. It was operated with constant biasing conditions in order to have pulses with 5 GHz emission rate and with emission wavelength of 1258 nm, that should fall in the gain spectral bandwidth of the amplifier. The pulses have duration of 2.3 ps and they are also assumed to have $sech^2$ shape. Lastly, the average optical power of the pulses emitted by this external source is 2.5 mW.
Notice that, in the simulations, the external laser source will be considered when reproducing the experimental results of [7], but it won't be when reproducing those of [9].

4.3 Single- and double-pass experimental setups

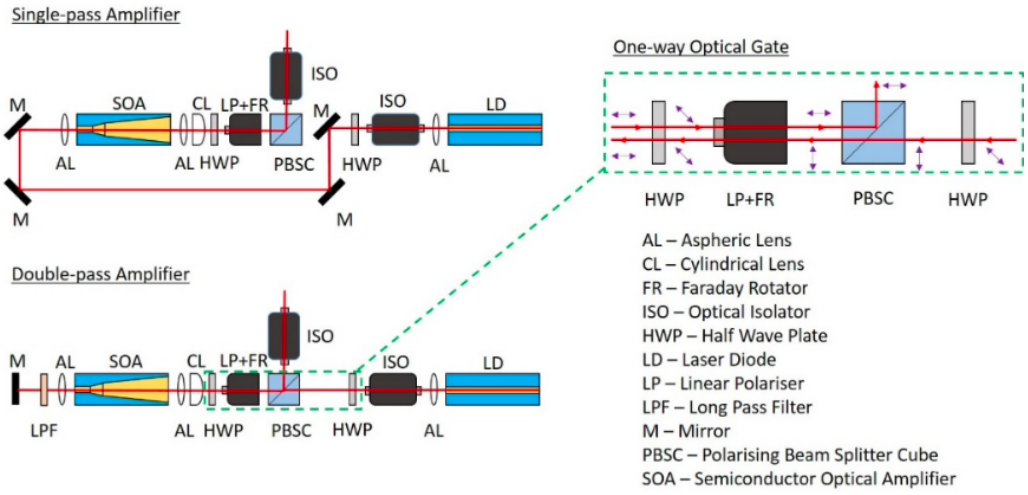

Figure 4.3. Experimental setup for the single- and double-pass configurations. Taken from reference [7].

For the **single-pass** amplification (the top one in Figure 4.3), the setup follows a typical master oscillator power amplifier configuration. The seed laser is coupled into the rear facet by a set of angled mirrors, it is amplified over a single passage through the device and the amplified signal is collected from the tapered front facet. An optical insulator is placed in front of the tapered front facet with the purpose of avoiding the output signal being coupled back into the light source.
For the **double-pass** amplification (the bottom one in Figure 4.3), instead, the amplified signal is collected from the same facet in which the optical source is

injected into. Indeed, the pulses from the seed laser are injected through the tapered front facet, they are amplified, they exit the device from the narrow rear facet and they are coupled back into the device into this same facet for the second amplification by means of a mirror. The presence of this highly reflective mirror creates an external cavity with the rear facet of the device. Since the input and output signals enter and exit through the same facet, some kind of one-way optical gate is needed to keep them separated. This component is created by means of a traditional polarization dependent insulator (dashed green box in Figure 4.3). The basic idea is to employ a Faraday rotator that rotates the polarization of the signals in a different way depending on the direction of the propagation (left to right or right to left). This allows the input and output signals to have perpendicular polarization with respect to each other and to have a different behaviour when reaching a polarising cube beam splitter (one is reflected, the other is transmitted).

Besides the implementation for the experiments of [7], in the context of commercial production, the double-pass configuration could also be directly integrated in the SOA by means of a highly reflective rear facet. This is of course convenient because the double-pass amplifier would have the same area occupation of the standard one, but it has also the advantage of requiring the alignment of the front facet exclusively, thus reducing the risk of coupling issues.

Both configurations need lenses to couple and collect the input and output signals, respectively. This optical apparatus introduces for sure losses, but it is not considered in the TDTW simulations.

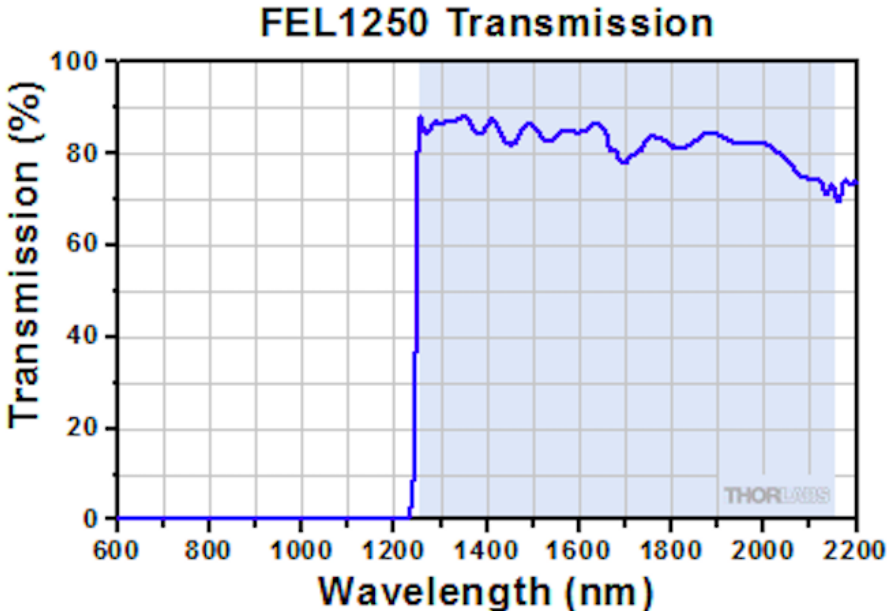

Figure 4.4. Transmission spectrum of the ThorLabs FEL1250 long-pass filter. Taken from reference [19].

According to [7], in the double-pass configuration, it is also necessary to include a long-pass filter in the external cavity in order to avoid an unwanted lasing at $\lambda = 1235\,\text{nm}$, detuned from the seed laser wavelength, that appears for high driving currents and effectively reduces the maximum available output power for this configuration. This lasing can be ascribed to the presence of some leftover spurious reflectivity at the facets of the device and it limits the operating current range of the device in double-pass configuration. For this reason, a long-pass filter with cut-off wavelength at $\lambda = 1250\,\text{nm}$ (Figure 4.4) is required, so to block the lasing frequency.
In reality, for the sake of simplicity, in the simulations the reflectivity of the facet is set to be identically zero. This means that this lasing phenomenon will not be observed and that the results of the TDTW simulations should correspond to the experimental results with the long-pass filter, minus the losses introduced by this component.

Chapter 5

Numerical implementation

In the previous chapter, we analysed the experimental setup that we aim to reproduce. In this new chapter, instead, the main points of the MATLAB implementation of the TDTW model will be presented. This is constituting the simulator that will be used in order to retrieve the numerical results that will be compared to the experimental ones.

First, let's briefly discuss the structure of the simulator. There are three main MATLAB files that are working together in order to implement the theory from the previous chapters:

- `DeviceData_SOA`: it contains the definitions of all the parameters of the device, based on those reported in Table 1 of [9]. This function produces a MATLAB structure called `Data`, containing all these parameters;

- `MainSOA`: it is the main function of the simulation. It calls the function `DeviceData_SOA` for the generation of the device parameters and it also generates a `Sim` structure, containing all the important simulation parameters (e.g. `TStart`, `TEnd`, `dt`, `ReferenceFrequency` and multiple flags for the simulation options). Of course, it is also calling the function for the physical simulation itself;

- `DDoSimulationOpt`: it is the function that is actually performing the simulation and that contains the rate equations and the time-discrete field propagation equations implementing the TDTW model.

In the next sections, we will highlight the prominent features of these three functions. Besides these important functions, there are many others that are used, for instance, for pre- or post-processing.

5.1 `DeviceData_SOA`

Let's start with the analysis of `DeviceData_SOA`. As mentioned before, it defines the main parameters of the device under test and it stores them in the `Data` structure to be used in the actual simulation.
First of all, let's analyse how the experimental data were modified in order to accommodate the fact that the model employed in the simulations for this thesis is not exactly the same as the one used in [9]. Table 5.1 shows the comparison between the parameters of the paper and the new parameters that were employed in order to have the best possible reproduction of the experimental results with the simulations. In particular, these values have been found with a trial-and-error approach, studying the logarithmic light-current characteristic of the device, in constant current density conditions.

Parameter	**Article value**	**New value**
η	0.65	0.55
g_i	690 - 750 - 700 cm^{-1} (max)	46 - 50 - 46.6 cm^{-1}
$\alpha^{\pm}$	1.35 (+) - 3.60 (-)	1.35 (+) - 4.60(-)
$\tau_{Aug,m}$	0.44 - 2.2 - 3.3 - 10^{50} ns	4.4 - 22 - 33 - 10^{50} ns

Table 5.1. List of the parameters that were modified in order to match the experimental results.

These parameters are used because:

1. the gain causes a rigid shift of the characteristic upwards or downwards at higher or lower powers;

2. the Auger characteristic time causes a modification of the shape of the characteristic, in particular, influencing at which current densities the saturation of the power starts to happen. This also causes an upward/downward shift, so we have to carefully pair the modification of the Auger time with the modification of the peak gain;

3. the forward and backward propagation losses set the relative distance between the curves associated to the front and rear facets, therefore causing the presence of the spectral asymmetry observed experimentally in [9];

4. the injection efficiency, in practice, causes a "rescaling" of the current density axis of the light-current characteristic. If we reduce the η, the light current characteristic results to be "stretched" because the same values of power will be reached at higher values of current density; if we increase the η, the light current characteristic results to be "compressed" because the same values of

power will be reached at lower values of current density. This can be used in order to finely tune the position of the power saturation.

The light-current characteristic will be presented in Chapter 6, as the other results.

5.1.1 Geometry of the device

Let's start with the modeling of the physical structure of the device. Taking Figure 4.1a as a reference, we have basically to model the SOA with its tapered sections. We already know that it has a 0.5 mm long straight ridge waveguide section, a 5 mm long tapered section, with full taper angle of 3°, and, finally, a 5 mm long tapered section, with full taper angle of 0.8°. This can be easily modelled using the following piece-wise function, exploiting simple geometrical rules:

$$W(z) = \begin{cases} W_{rear}, & z < z_1 \\ W_{rear} + 2(z - z_1)\tan\left(\dfrac{\theta_1}{2}\right), & z_1 \leq z < z_2 \\ W_{rear} + 2(z_2 - z_1)\tan\left(\dfrac{\theta_1}{2}\right) + 2(z - z_2)\tan\left(\dfrac{\theta_2}{2}\right), & z_2 \leq z < L \end{cases} \tag{5.1}$$

where $W_{rear} = 14\,\mu m$ is the width of the constant-width rear section, $z_1 = 500\,\mu m$, $z_2 = 1000\,\mu m$ and $L = 600\,\mu m$ are the first section length, second section length and device length respectively and $\theta_1 = 3°$ and $\theta_2 = 0.8°$ are the full taper angles of first and second tapered sections.
This is then modelled in MATLAB as follows:

```
function w=Width(z, IncludeExtFeedback)
%Waveguide width as a function of the longitudinal position
%Input:
%   z:  [1,NumSlices] slices positions [um]
%Output:
%   w:  [1,NumSlices] waveguide widths [um]

%[1,1] Rear section width [um]
RearW = 14;
%[1, NumSlices] Width of the structure [um]
w = RearW * ones(size(z));
%[1,1] Half flare angle of the first tapered section [degree->radian]
Theta1Halved = 1.5 * pi / 180;
%[1,1] Half flare angle of the second tapered section [degree->radian]
Theta2Halved = 0.4 * pi / 180;
%[1,1] Position of the beginning of the first tapered section [um]
Z1 = 500;
%[1,1] Position of the beginning of the first tapered section [um]
```

```
19 Z2 = 1000;
20
21 w(z>=Z1 & z<Z2) = RearW + 2 * (z(z>=Z1 & z<Z2) - Z1) *
       tan(Theta1Halved);
22 w(z>=Z2) = RearW + 2*(Z2-Z1)*tan(Theta1Halved) +
       2*(z(z>=Z2)-Z2)*tan(Theta2Halved);
23
24 if IncludeExtFeedback == 1 %Double Pass
25     %[1,NumSlices] Width of the structure [um]
26     w = flip(w);
27 end
28 end
```

Basically, this is simply the direct implementation of Equation 5.1. This is defined as a function because it will be called in `DDoSimulationOpt` after the definition of the discrete spatial step. The only point to be discussed is the last `if` statement: the flag `IncludeExtFeedback` is true whenever we work in the double-pass configuration. In that case, we flip the entire structure, since we want the optical excitation to be always fed in the first slice of the device. This is basically reproducing the experimental setup shown in Figure 4.3.
The width of the device computed and output by this function `Width` is represented in Figure 5.1, where the three sections are clearly visible.

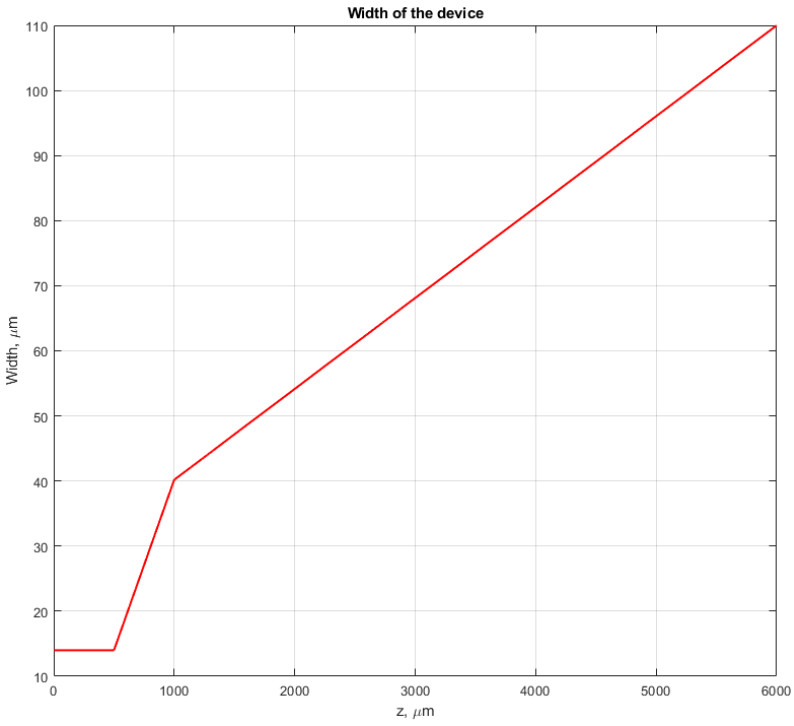

Figure 5.1. Width of the device under test.

5.1.2 QD chirp and broadening

Another fundamental feature of the `DeviceData_SOA` function consists in the definition of the chirp of the quantum dots. From the energy point of view, the system is described by means of the energy gaps, corresponding to the interband transition energies that also set the emission wavelength. In this case we have:

```
%[1, NumLayers] Multiplicity of layers belonging to the same kind of QD
    []
MultQDLayers          =     [4, 3, 3];
%[1,1] Energy gap between CB and VB band edges in the SCH [eV]
EnergyGapSCH          =      1.2797;
%[1,1] Energy gap between CB and VB band edges in the WL [eV]
EnergyGapWL           =      1.100;
%[NumStates,NumLayers] Characteristic interband transition energies for
    the QD central (most likely) QD population (ES2, ES1, GS) [eV]
EnergyGapQDCentralPop =    [1.0690, 1.0508, 1.0333 ; ...
                            1.0500, 1.0265, 0.9960 ; ...
                            1.0239, 0.9976, 0.9650];
```

These central energies, expressed in electronvolt, are directly taken from Table 4.1. Since we have multiple populations with different characteristics, the QD energies are defined by means of a matrix, where, on each row, we have the ES2, ES1 and GS central energies for a given QD population. The parameter `MultQDLayers` represents the number of QD layers that are characterised by the same transition energies (the total number is 10).

In the case of a non-chirped device, in order to model real behaviour, we would have to consider the so-called *inhomogeneous broadening*. Basically, since the production processes of real QDs are not that precise, in our devices, the QDs do not have exactly the same behaviour, due to the fact that their size and transition energies will be statistically distributed (more or less, with a Gaussian distribution). Therefore, the energy gap values of the confined states of the system will be broadened and, in order to model this, we consider a set subpopulations, with Gaussian existence probability described by Equation (2.10). Within these subpopulations, the QDs are considered to be characterised by the same properties, but differing from population to population.

In the case of a chirped device, the strategy is slightly different. We do not consider these gaussian subpopulations, but we assume that, within the same layer, the QDs have the same features. For this reason, the energy for each population is simply the central energy from before (`EnergyGapQDCentralPop`) and the existence probabilities are given by the inverse of the layer multiplicity (properly normalized so that their sum amounts to 1 as any other probability).

Inside the code, both strategies are implemented, so that the simulator can be adapted both for chirped and non-chirped simulations. Which one of the two is

employed is decided based on the dimensions of `EnergyGapQDCentralPop` (if it is a matrix, we are in the chirped case). This is done by means of the following code:

```
%[1,1] Number of QD layers []
NumDiffDotLayers      =     size(EnergyGapQDCentralPop,2);
%[NumStates,1] FWHM->sigma of inhomogeneous broadening of the QD
    ensemble (ES2, ES1, GS) [eV]
InhomDeltaE           =     [0.0350; 0.0350; 0.0350]/sqrt(8*log(2));

if NumDiffDotLayers == 1
    if NumQDPopulations==1
        EnergyGapQD=EnergyGapQDCentralPop;
    else
    %[NumStates,NumPops] Characteristic interband transition energies
        for the QD populations (ES2; ES1; GS) [eV]
    EnergyGapQD       =     [...
        linspace(EnergyGapQDCentralPop(1)+3*InhomDeltaE(1),
        EnergyGapQDCentralPop(1)-3*InhomDeltaE(1),NumQDPopulations);
        linspace(EnergyGapQDCentralPop(2)+3*InhomDeltaE(2),
        EnergyGapQDCentralPop(2)-3*InhomDeltaE(2),NumQDPopulations);
        linspace(EnergyGapQDCentralPop(3)+3*InhomDeltaE(3),
        EnergyGapQDCentralPop(3)-3*InhomDeltaE(3),NumQDPopulations);
        ];
    end
    %[NumStates,NumPops] Gaussian distribution of the existence prob. of
        each QD population [>=0]
    Inhomog_distribution=   ...
        exp(-(EnergyGapQD-repmat(EnergyGapQDCentralPop,1,NumQDPopulations
        )).^2./(2*repmat(InhomDeltaE,1,NumQDPopulations).^2));
elseif NumDiffDotLayers > 1
    %[NumStates,NumPops] Characteristic interband transition energies
        for the QD populations (ES2; ES1; GS) [eV]
    EnergyGapQD       =     EnergyGapQDCentralPop;
    %[NumStates,NumPops] Gaussian distribution of the existence prob. of
        each QD population [>=0]
    Inhomog_distribution=   repmat(MultQDLayers, NumDiffDotLayers, 1);
    NumQDPopulations=NumDiffDotLayers;
else
    error ([mfilename ':InvalidEnergyMatrixSize'], ...
        'The size of the central energy gap matrix is not valid.');
end

%[NumStates,NumPops] Normalized distribution of the existence prob. of
    each QD population. The sum (per rows) is 1 [>=0]
Inhomog_distribution  =     ...
```

```
37      Inhomog_distribution./repmat(sum(Inhomog_distribution,2),
38      1,NumDiffDotLayers);
```

In addition to the inhomogeneous broadening, we have also to consider the *homogeneous broadening*. This is basically taking into account the fact that the interband transition energy is homogeneously broadened according to a Lorentzian distribution. This can be simply modelled with two functions:

```
1  function H=Func_HomoBroadeningES(Ntoth)
2  %Homogeneous broadening of the ES as a function of the total carrier
       number per slice
3  %Input:
4  %   Ntoth: [1,NumSlices] total carrier number in each slice [>=0]
5  %Output:
6  %   H:  vector of homogeneous broadening values [rad/ns]
7
8  H=26600*ones(size(Ntoth));
9  end
10
11 function H=Func_HomoBroadeningGS(Ntoth)
12 %Homogeneous broadening of the GS as a function of the total carrier
       number per slice
13 %Input:
14 %   Ntoth: [1,NumSlices] total carrier number in each slice [>=0]
15 %Output:
16 %   H:      vector of homogeneous broadening values [rad/ns]
17
18 H=26600*ones(size(Ntoth));
19 end
```

The value $26\,600\,\mathrm{rad\,ns^{-1}}$ corresponds to the value $\Delta E = 35\,\mathrm{eV}$ of Table 4.1 in this new unit of measure, which is the one used in the program. This value is obtained with a conversion factor $1520\,\mathrm{rad\,eV^{-1}\,ns^{-1}}$. The input parameter `Ntoth` is the total number of carriers per slice. This can be used in order to have a carrier-dependent homogeneous broadening, which although will not be used in the analysis of this particular device.

A final point to be discussed about the energies of the system is related to the energy differences between the various confined states on the same band. While the energy gap of the states is fixed by the wavelength of emission and the energy difference between these states is fixed by their gaps, the proportion of how much of this difference is related to the conduction or valence bands is not set a priori. This, although, is very important since it is related to the escape rates from the energy states that regulate the behaviour of the device. We do not have experimental information related to this, but we can set them so that we get reasonable escape times. In this case, the following energy differences were set:

```
%[NumStates,NumPops] Energy difference between CB states
    (SCH-WL;WL-ES2;ES2-ES1;ES1-GS) [eV]
'DeltaEnergycb',...
    [(EnergyGapSCH-EnergyGapWL)*ones(1,NumQDPopulations)*0.4*3;
    (EnergyGapWL-EnergyGapQD(1,:))*0.77/1.4/2*2*2;
    (EnergyGapQD(1,:)-EnergyGapQD(2,:))*0.35;
    (EnergyGapQD(2,:)-EnergyGapQD(3,:))*0.62*1.3], ...
```

Note that `DeltaEnergycb` is a parameter contained in the `Data` structure.

5.1.3 Losses

According to the experimental data from [9], we have that the waveguide losses are characterised by different coefficients depending on the direction of propagation. This is obtained experimentally by observing an asymmetry of the output power in single-pass amplification depending on the considered output facet.
This can be modelled in the simulator with the following functions, contained in `DeviceData_SOA`:

```
function alpha_i=Alfa_i_prog(z, IncludeExtFeedback)
%Waveguide power losses as a function of the longitudinal position
%Input:
%   z:          [1,NumSlices] slices positions [um]
%Output:
%   alpha_i:    row vector of waveguide power losses [cm^-1]

if IncludeExtFeedback == 1   %Double pass
    alpha_i=ones(size(z))*3.60;
elseif IncludeExtFeedback == 0 %Single pass
    alpha_i=ones(size(z))*1.35;
else                          %Error
    error('IncludeExtFeedback can only be a boolean.')
end
end

function alpha_i=Alfa_i_regr(z, IncludeExtFeedback)
%Waveguide power losses as a function of the longitudinal position
%Input:
%   z:          [1,NumSlices] slices positions [um]
%Output:
%   alpha_i:    row vector of waveguide power losses [cm^-1]

if IncludeExtFeedback == 1   %Double pass
    alpha_i=ones(size(z))*1.35;
elseif IncludeExtFeedback == 0 %Single pass
```

```
27      alpha_i=ones(size(z))*3.60;
28  else                            %Error
29      error('IncludeExtFeedback can only be a boolean.')
30  end
31  end
```

Similarly to the `Width` function, in this case as well we have to modify the α coefficients depending on the `IncludeExtFeedback` flag, due to the fact that the progressive and regressive directions will change whether the device is working in double or single-pass configuration. These two functions as well will be called in `DDoSimulationOpt`, receiving the `z` vector and the `IncludeExtFeedback` flag.
In addition to the forward and backward propagating waveguide losses, also plasma losses are considered, using the same coefficient as Table 4.1. Instead, higher order effects like the Kerr effect losses are neglected.

5.1.4 Confinement factors

Another important aspect to be considered is the field confinement factors in the y direction. While in the x direction (growth direction), the confinement factor is assumed to be constant, we can easily understand that the Γ_y factor will change with the z position, due to the fact that the structure is tapered, which implies a variation of how the field is confined along the propagation direction. In order to model this feature, some experimental datasets are employed.

```
1  function Gy=GammaY(z,IncludeExtFeedback)
2  %Confinement factor in the y direction as a function of the total
       carrier number per slice
3  %Input:
4  %   z:  [1,NumSlices] slices positions [um]
5  %Output:
6  %   w:  vector of confinement factor values [>0]
7
8  GammaPlus = GetLateralConfinementFactorPlus(z);
9  GammaMinus = GetLateralConfinementFactorMinus(z);
10
11 Gy=(GammaPlus+GammaMinus)/2;
12
13 if IncludeExtFeedback == 1 %Double Pass
14     Gy = flip(Gy);
15 end
16 end
```

Once again, we have to flip the vector if we are in the double-pass configuration. `GetLateralConfinementFactorPlus` and `GetLateralConfinementFactorMinus` are two additional utility functions that are storing the Γ_y^+ and Γ_y^- datasets

obtained from BPM simulations and that fit them on vectors with size given by the number of z slices. Note that, in theory, we should consider two separate confinement factors and use them in the forward and backward field equations, but, for simplicity's sake, it was decided to use their average value.
In reality, as we can see from Figure 5.2, the forward and backward confinement factors are not so dissimilar from their average value, for what concerns both values and profile, so we can use the average Γ_y without losing too much precision.

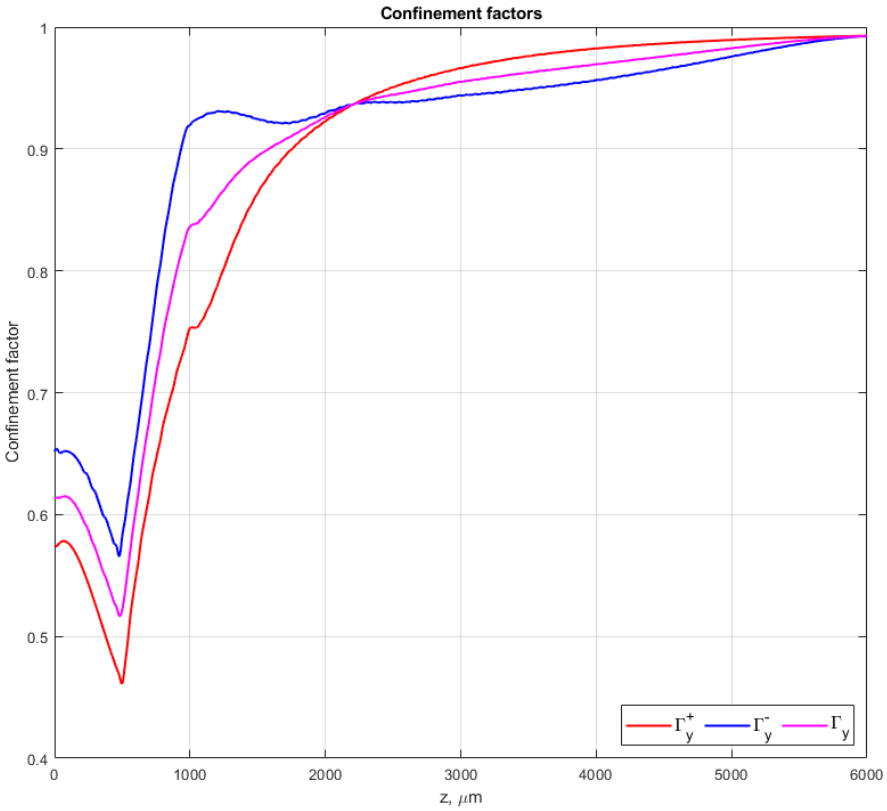

Figure 5.2. Γ_y confinement factor profiles with respect to the propagation direction.

5.1.5 Polarization of the device

Finally, the biasing of the device is the last important point to be discussed about `DeviceData_SOA`. We know from [9] that the device under test is built in such a way that its rear and front sections can be independently biased. This can be done thanks to an insulating trench placed at 1.875 mm from the rear facet. In order to specify the bias of the device, the following function is implemented:

```
1 function E=Electrode(z, IncludeExtFeedback)
2 %Function returning the index of the electrode
```

```
%In a multielectrode device, to any electrode with current injection a
%positive integer number is assigned, while a negative integer number is
%used to identify reversely polarized regions. The assigned indices can
    be
%used to define the current/voltage specified in the Sim.Pilot
    parameter.
%Input:
%   z:  [1,NumSlices] slices positions [um]
%Output:
%   E:  vector of electrodes numbers [integer <0 or >0]

E = zeros(size(z));

if IncludeExtFeedback == 0   %Single Pass
    %[1, 1] Position of the insulating trench (from rear facet) [um]
    zTrench = 1875;
    E = @(Z) 1 + 1 * (Z>zTrench);
    E = E(z);
elseif IncludeExtFeedback == 1 %Double Pass
    %[1, 1] Position of the insulating trench (from rear facet) [um]
    zTrench = 6000 - 1875;
    E = @(Z) 1 + 1 * (Z<zTrench);
    E = E(z);
else
    error('IncludeExtFeedback can only be a boolean.')
end
end
```

This is basically stating that we have two electrodes with current injection and they are identified with the labels 1 and 2. The two of them are separated in correspondence of $z = 1875\,\mu m$, which is the location of the insulating trench on the real device. Of course, we have to take into account the fact that, depending on the configuration, the device might have to be flipped (double-pass configuration).

5.1.6 External cavity feedback

We already know that, if using a double-pass configuration, many of the quantities described before have to be modified in order to accommodate the analysis of the different experimental setup. It has to be said that, in this configuration, we need an external mirror outside the output facet of the SOA, in order to reflect the light back inside the device for the second pass amplification. This is effectively creating an external cavity, with the following parameters:

Symbol	Description	Value
L_{ext}	Length of the external cavity	1000 µm
r_{ext}	Reflectivity of the mirror	1
n_{ext}	Refractive index of the caviy	1 (air)

Table 5.2. Parameters of the external cavity used during the simulation.

Note: The `Data` structure also contains the field `'Excitonic'`. This is basically a Boolean flag that allows us to choose whether we want to use the excitonic rate equation model (`'Excitonic' = true`) or the independent rate equation model (`'Excitonic' = false`). For this reason, since we are considering the excitonic model for our simulations, this variable is set to `true`.

5.2 `MainSOA`

The `MainSOA` function, of course, is the one that has to be run to launch the simulation, by calling the other notable functions. Indeed, first it calls the function `DeviceData_SOA` for the generation of the `Data` structure and then it calls `DDoSimulationOpt` for the solution of the differential equations at each time step, for each spatial slice. Let's analyse in detail what does `MainSOA` have to accomplish.

5.2.1 `Sim` structure

After calling `DeviceData_SOA` and saving the device data, `MainSOA` has to generate its own structure, called `Sim`. As the name suggests, it contains some significant parameters that will be important for the simulation in `DDoSimulationOpt`. This is implemented as follows:

```
% Numerical simulation parameters.
%Remark that the Pilot parameter will be replaced before the simulation
%is started using the values from a vector of currents
Sim= struct(...
    %[string] Reference Frequency []
    'ReferenceFrequency','GS-ES2'...
    %[1,1] Time interval between simulation state printings [ns]
    ,'PrintSimulationState',0.1 ...
    %[1,1] Simulation time step [ns]
    ,'dt',15e-6 ...
    %[1,1] Simulation start time. This is the origin for the time
        vector. [ns]
    ,'TStart',0 ...
    %[1,1] Simulation end time; it must be > TStart. [ns]
```

```
14    ,'TEnd',10 ...
15    %[1,1] or [f(e,t)->[NumSlices,1]] Injected current [mA]
16    ,'Pilot',0 ...
17    %[1,1] Flag indicating the level of displayed messages. []
18    ,'Verbose',1 ...
19    %[1,1] Time starting from which the sponateneous emission is set to
          0 [ns]
20    ,'TimeStopEsp',10000 ...
21    %[1,1] Flag; 1: the simulation must also solve for photon/field; 0:
          the simulation calculates carrier distribution without photons []
22    ,'considerphotons',1 ...
23    %[string or f(Data, Sim, FinalCurrent)->string]. Name of the file
          from which to load the simulation state.
24    ,'LoadState', [] ...
25    %[string or f(Data, Sim, FinalCurrent)->string]. Name of the file to
          save the simulation state to.
26    ,'StateFilename', [] ...
27    %[string or f(Data, Sim, FinalCurrent)->string]. Name of the file to
          save the simulation results to.
28    ,'ResFilename', [] ...
29     %[complex] Optical excitation [sqrt(mW)]
30    ,'OpticalExcitation', []...
31    %[1,1] Flag; 1: the optical excitation is included; 0: the optical
          excitation is not included []
32    ,'IncludeOpticalExcitation', false ...
33    %[1,1] Flag; 1: the external mirror is included; 0: the external
          mirror is not included []
34    ,'IncludeExtFeedback', false...
35    %[1,1] Flag; 1: filter included; 0: filter not included []
36    ,'FilterA', 0 ...
37    );
```

Let's analyse in detail the various variables contained in this structure:

- `ReferenceFrequency`: it is a string that can assume values `'GS'`, `'GS-ES1'` and `'GS-ES2'`, thus setting the choice of the reference frequency for the simulation. In the case of this simulator, where we do not only consider the emission from GS and ES1, but also from ES2, the average frequency between GS and ES2 is taken as reference;
- `PrintSimulationState`: it sets the time in nanoseconds that has to elapse before the simulator can print the simulation state. This includes the current time step, the power from rear and front facets, the elapsed time and the remaining time;
- `dt`: it is the simulation time step in nanoseconds, namely the minimum time

interval. It has to be set in order to have the best trade-off between simulation duration and precision of the results;

- `TStart`: it is the starting time of the simulation in nanoseconds;
- `TEnd`: it is the end time of the simulation in nanoseconds;
- `Pilot`: it is the parameter defining the injected current in mA in the device. It can be either a constant or a function, in the case of a multi-electrode device like this one. Here it is set to 0 because it will be defined later;
- `Verbose`: it is a Boolean flag that can be set to 1 in order to display the messages from the simulator (for instance, the simulation state every `PrintSimulationState` ns) or to 0 in order not to show any of them;
- `TimeStopEsp`: it is a parameter that allows us to set the time in nanoseconds after which the spontaneous emission is turned off. This could be useful in particular kinds of simulations, but this is not the case. That's why it is set to 10 µs, whereas the simulations are in the order of tens of nanoseconds;
- `considerphotons`: it is Boolean flag that can be set to 1 in order to run the simulation considering the effect of photons in the simulations or to 0 in order to solve the equations for the carriers distribution without considering photons;
- `LoadState`: it is a string that can contain the name of a file to be loaded. This can be used in order to continue the simulation starting from a previously saved simulation state;
- `StateFilename`: it is a string that contains the name to be used for the simulation state file. This is later set by the `MainSOA` to be in the format `State_DoublePass_FrontCurr%gmA_RearCurr%gmA_%gns.mat` or in the format `State_SinglePass_FrontCurr%gmA_RearCurr%gmA_%gns.mat`.
- `ResFilename`: it is a string that contains the name to be used for the file storing the simulation results. This is later set by the `MainSOA` to be in the format `Res_DoublePass_FrontCurr%gmA_RearCurr%gmA_From%gnsTo%gns.mat` or `Res_SinglePass_FrontCurr%gmA_RearCurr%gmA_From%gnsTo%gns.mat`.
- `OpticalExcitation`: it can be either a constant value or a function in square root of milliwatt that contains the definition of the external optical source to be amplified by the SOA. It can also be set to be empty if the simulation does not require an external excitation.

- `IncludeOpticalExcitation`: it is a Boolean flag that is responsible of including or not the optical excitation. It has to be set to `false` in order not to include the optical source, to `true` in order to include it. If `OpticalExcitation` is not defined, it will be automatically set to `false`.
- `IncludeExtFeedback`: it is a Boolean flag that is responsible of including or not the external cavity feedback. This means that it is basically setting the double-pass configuration when it is set to `true` (feedback mirror included) or the single-pass one when it is set to `false` (feedback mirror not included). For this reason, it is also the flag that is checked by the functions in `DeviceData_SOA` to establish whether we are running a single- or double-pass simulation.
- `FilterA`: it is a Boolean flag for the inclusion of the external cavity filter, used in the experiments of [7], as mentioned in Chapter 4. If it is 1, the filter will be included, if it is 0, it will not.

5.2.2 Optical source

The optical source can be defined and modelled as a function of time to be then used in `DDoSimulationOpt` for simulations including the external optical excitation. In particular, it will be important when reproducing the results of [7], where a pulsed laser source is employed. Indeed, it is a train of squared hyperbolic secant pulses with 5 GHz emission rate. As stated before in Chapter 4, the pulses have 2.3 ps duration and the source has 2.5 mW output power on the average.
In order to model this train of pulses, the `pulstran` function from the Signal Processing Toolbox is employed. The optical source is therefore modelled with the following lines of code:

```
if Sim.IncludeOpticalExcitation == 1
    %[1,1] Wavelength of emission of the seed laser [m]
    Lambda = 1258e-9;
    %[1,1] Frequency of emission of the seed laser [Hz->GHz]
    fLaser = 3e8/Lambda* (1e-9);
    %[1,1] Simulation reference frequency [Hz->GHz]
    ReferenceFrequency = ...
           ComputeReferenceFrequency(Data,Sim)* (1e-9);
    %[1,1] Pulse height [sqrt(W)]
    PulseHeight = sqrt(191.6);
    %[1,1] Pulse FWHM [ns]
    FWHM = 2.3e-3;
    %[1,1] Pulse Amplitude [ns]
    PulseAmplitude = FWHM/1.76;
    %[f(z)] Pulse shape []
    PulseShape = @(x) PulseHeight*sech(PulseAmplitude^-1*x);
```

```
17      %[1,1] Pulse Frequency [Hz]
18      f0 = 5e9;
19      %[1,1] Pulse Period [s->ns]
20      t0 = 1/f0 * (1/1e-9);
21      %[1,NumSamples] Time at which a pulse is centered [ns]
22      d = Sim.TStart+0.1:t0:Sim.TEnd+0.1;
23
24      %[complex] Optical excitation (sech pulses for the field)[sqrt(mW)]
25      Sim.OpticalExcitation = ...
26          @(t) pulstran(t',d',PulseShape).* ...
27              exp(1i*2*pi*(ReferenceFrequency-fLaser)*t)'.*(t>=10)';
28
29  elseif Sim.IncludeOpticalExcitation == 0
30      Sim.OpticalExcitation = [];
31
32  else
33      error('IncludeOpticalExcitation can only be a boolean.');
34  end
```

Basically, these lines of code define the `Sim.OpticalExcitation` as a function of time `t`, a vector of time instants that will be later defined in `DDoSimulationOpt`. The train of squared hyperbolic secant pulses is defined with $f_{rep} = 5\,\text{GHz}$, $\lambda_{laser} = 1258\,\text{nm}$ and $A = \sqrt{191.6}\sqrt{\text{mW}}$. The latter is employed because 191.6 mW is the peak power needed to reach an average power of 2.5 mW for a train of pulses with the specifics reported in [7], according to the formulae expressed in [20], which are relating the average power to the peak power through the pulse energy. Note that the pulse amplitude is expressed in square root of milliwatt, because this is the unit of measure required by the program. Moreover, in order to achieve a FWHM of 2.3 ps, according to [24], the hyperbolic secant function has to be defined as $sech(t/X)$, where X is what is called `PulseAmplitude` in the reported code. Then, the actual signal is defined by means of the function `pulstran`. Not only this, we also use a complex exponential in order to translate the spectrum around the λ_{laser} from the reference frequency of the simulation, hence the quantity `(ReferenceFrequency-fLaser)` in the exponential. There is also a logic operation `(t>10)`: this is basically making the source wait 10 ns before turning on, because in the real experiments the pulses were launched after the device reached a steady state. Another important point is the vector `d` that basically contains the set of time instants at which the pulses will be centered. Note that the pulses are skewed of 100 ps in order to avoid having the first and last ones halved.

Figure 5.3a shows an example of train of pulses generated with the function `Sim.OpticalExcitation` (in modulus square to have dimensionally a power), given a vector of time instants. Figure 5.3b, instead, shows the detail of one of the squared hyperbolic pulses creating the train.

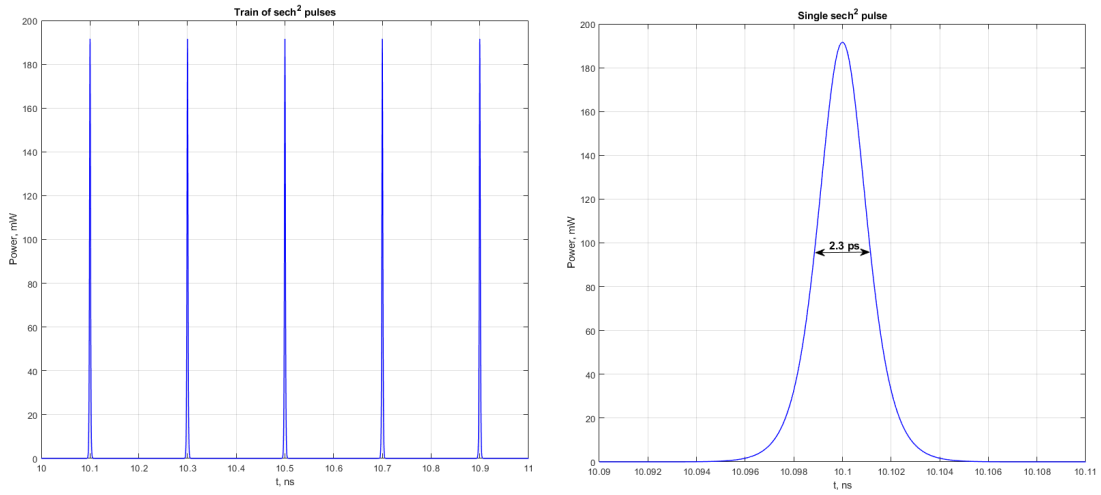

(a) **(b)**

Figure 5.3. (a) Pulse of squared hyperbolic secant pulses between 10 ns and 11 ns. (b) Detail of one of the squared hyperbolic secant pulses making up the train.

5.2.3 Driving currents and call to `DDoSimulationOpt`

Another important point is the definition of the `Sim.Pilot` variable, which is the one that sets the driving current in the two sections of the device. For this purpose, we use the following piece of code:

```
%[N,1] Vector of rear section currents [mA]
IRear = [0.1, 0.1]*1e3;
%[N,1] Vector of front section currents [mA]
IFront = [1, 3.5]*1e3;

Simv = repmat(Sim, 1, length(IFront));
for kInd = 1:length(IFront)
    DrivingCurr = @(e,t) IRear(kInd)*(e==1)+IFront(kInd)*(e==2);
    Simv(kInd).Pilot = DrivingCurr;
end
```

Basically, we define the vectors of front and rear section currents to be simulated. These can of course be made up of single elements if we want to simulate only a pair of front/rear currents. The `Simv` variable is simply an array of `Sim` structures, to be used if we are simulating multiple current pairs. By means of the for loop, we build the `Pilot` function and, if we have multiple elements inside the current vectors, we store them inside `Simv`.

Finally, we have to call the `DDoSimulationOpt` function in order to launch the actual simulation. This can be done with this line:

```
DoSimsParallelMPRE(Simv,Data,'',8);
```

`DoSimsParallelMPRE` is basically a function that calls `DDoSimulationOpt` by launching a `parfor` loop, if `Simv` has more than one element. This parallel for loop allows us to run multiple simulations in parallel, thus reducing the overall computational time.

5.3 DDoSimulationOpt

Finally, we can analyse `DDoSimulationOpt`, which constitutes the main part of the simulator. As already said, this function contains the implementation of the TDTW model that has been studied in Chapter 3. It receives the `Data` and `Sim` structures as inputs and, based on their content, it computes the evolution of the field in each slice for each time step, solving the propagation equations for that particular device. Of course, this can be done only if we also compute the evolution of the carrier populations inside the QD energy states.
Let's highlight some noteworthy portions of the code.

5.3.1 Energy reference choice

As mentioned in the theoretical section of this work, the choice of a proper reference frequency is fundamental in order to retrieve the best possible results for our system, since, if the distance between the frequency associated to the QD states and the reference is too large, the slowly varying envelope approximation on which we built our model might not be valid. The choice of the reference frequency is implemented in `DDoSimulationOpt` as follows:

```
if Data.NumDiffDotLayers == 1 % not chirped
    %[1,1] Transition energy for the ES2 of the central population [eV]
    PeakEnergyES2 = Data.EnergyGapQDCentralPop(end-2);
    %[1,1] Transition energy for the ES1 of the central population [eV]
    PeakEnergyES1 = Data.EnergyGapQDCentralPop(end-1);
    %[1,1] Transition energy for the GS of the central population [eV]
    PeakEnergyGS = Data.EnergyGapQDCentralPop(end);
elseif Data.NumDiffDotLayers > 1 % chirped
    %[1,1] Transition energy for the ES2 of the central population [eV]
    PeakEnergyES2
        =sum(Data.EnergyGapQDCentralPop(1,:))/Data.NumDiffDotLayers;
    %[1,1] Transition energy for the ES1 of the central population [eV]
    PeakEnergyES1
        =sum(Data.EnergyGapQDCentralPop(2,:))/Data.NumDiffDotLayers;
    %[1,1] Transition energy for the GS of the central population [eV]
    PeakEnergyGS
        =sum(Data.EnergyGapQDCentralPop(3,:))/Data.NumDiffDotLayers;
```

```
15 else
16     error('The number of different layers can only be 1 or more.')
17 end
18
19
20 %% Choice of the SVEA reference frequency
21 if strcmp(Sim.ReferenceFrequency,'GS')
22     %[1,1] Flag indicating the reference energy [bool]
23     %Reference frequency @ GS characteristic interband transition
24     %energy of the central (most probable) QD population
25     ReferenceFreq=0;
26     %[1,1] Reference energy [eV]
27     ReferenceEnergy=PeakEnergyGS;
28
29 elseif strcmp(Sim.ReferenceFrequency,'GS-ES1')
30     %[1,1] Flag indicating the reference energy [bool]
31     % Reference energy as average between GS and ES1 characteristic
32     %interband transition energy of the central (most probable) QD
           population
33     ReferenceFreq=1;
34      %[1,1] Reference energy [eV]
35     ReferenceEnergy=(PeakEnergyES1+PeakEnergyGS)/2;
36
37 elseif strcmp(Sim.ReferenceFrequency,'GS-ES2')
38     %[1,1] Flag indicating the reference energy [bool]
39     % Reference energy as average between GS and ES2 characteristic
40     %interband transition energy of the central (most probable) QD
           population
41     ReferenceFreq=2;
42     %[1,1] Reference energy [eV]
43     ReferenceEnergy=(PeakEnergyES2+PeakEnergyGS)/2;
44
45 else
46     error('An invalid reference frequency label was passed.')
47 end
48
49 %[1,1] Simulation reference wavelength [um]
50 ReferenceWavelength=Constants.h*Constants.c/ReferenceEnergy;
```

First, we have to compute the energies associated to GS, ES1 and ES2. This has to be done differently for the non-chirped and chirped cases. In the first instance, we set the central population energy gap as peak energy, since we are considering N populations of QD with gap distributed around this value. Instead, in the second, we compute the peak energy as the arithmetic average value between the energy gaps of the three kinds of QD.

Then, instead of computing the frequency, we compute the reference energy. Of course, the reference energy changes depending on our choice. We use:

$$E_{ref}^{(GS)} = E_{peak}^{GS} \tag{5.2}$$

$$E_{ref}^{(GS-ES_1)} = \frac{E_{peak}^{GS} + E_{peak}^{ES_1}}{2} \tag{5.3}$$

$$E_{ref}^{(GS-ES_2)} = \frac{E_{peak}^{GS} + E_{peak}^{ES_2}}{2} \tag{5.4}$$

Just like it was discussed before, since in this model we are considering also the emission from the second excited state, the most reasonable reference choice is represented by $E_{ref}^{(GS-ES_2)}$, otherwise ES2 would be too far away from the reference. Finally, we also compute the wavelength associated to this reference energy, by using the equivalences $E = h \cdot f$ and $c = \lambda \cdot f$. In Table 5.3, the resulting reference energies and wavelengths for all the possible reference choices are reported, together with the percentage error with respect to ES2.

Reference	**Energy [eV]**	**Wavelength [nm]**	**Distance from ES2**
`'GS'`	0.9955	1245.5	5.6%
`'GS-ES1'`	1.0098	1227.8	4.1%
`'GS-ES2'`	1.0233	1211.7	2.8%

Table 5.3. Reference energies, wavelengths and errors with respect to the ES2 peak energy for all the possible reference choices.

It turns out that the only viable choice is to use `'GS-ES2'` as reference, in order to avoid aliasing problems related to the presence of the second excited state in the model. This is reasonable, since `'GS-ES2'` is the reference giving the lowest errors with respect to the peak energies of the three confined states, since $E_{ref}^{(GS-ES_2)}$ is located quite close to $E_{peak}^{ES_1} = 1.0242\,\text{eV}$.
In the code, the possibility of choosing the other references is maintained anyway, in order to have the best possible flexibility for our simulator, so that it could be used to simulate also devices where the ES2 contribution is less relevant.

5.3.2 Carrier rate equations

After many lines of code doing input checks and variable definition, we finally start with the main loop over the time vector. The first important point of this loop is the computation of the variation of the carriers in each slice at each time step of the loop itself. This of course is done by means of the rate equations presented in Chapter 3.

Let's now analyse of Equations (3.40a)-(3.40e) are implemented. Starting from the Separate Confined Heterostructure (SCH) rate equation, we know that it contains all the contribution adding or subtracting carrier from the SCH:

$$\frac{\partial N_{SCH}}{\partial t} = +\eta_i \frac{J}{e} W - \frac{N_{SCH}}{\tau_{c,WL}} + \frac{N_{WL}}{\tau_{e,WL}} - \\ - \frac{B_{SCH}}{W h_{SCH}} N_{SCH}^2 - \frac{N_{SCH}}{\tau_{nr,SCH}}$$

Here we can recognise the current injection, the capture from the WL, the escape towards the WL, the spontaneous emission and the non-radiative components. This equation, describing the variation of the SCH population, is implemented in MATLAB as follows:

```
%%%%% Variation of SCH carriers in each slice in dt %%%%%

%[1,NumSlices] Net Current in cb including drift sweep out [ns^-1]
NetCurrentCB=I.*NetCurrentCoeff+NcbSCH.*NetCurrentCBCoeff2;
%[1,NumSlices] Net Current in vb including drift sweep out [ns^-1]
NetCurrentVB=I.*NetCurrentCoeff+NvbSCH.*NetCurrentVBCoeff2;
%[1,NumSlices] Product of carrier in cb and vb in SCH [ns^-1]
NcbvbSCH=NcbSCH.*NvbSCH;
%[1,NumSlices] Non radiative recombination in SCH [ns^-1]
NonRadiativeRecombinationSCH=sqrt(NcbvbSCH).*OneOverTauNRcbSCH;
%[1,NumSlices] Capture from SCH to WL [ns^-1]
CaptureFromSCH2WL=...
    NcbSCH.*(1-NcbWL.*Number2ProbWLcb).*OneOverTauCapcbSCH2WL;
%[1,NumSlices] Escape from WL to SCH [ns^-1]
EscapeFromWL2SCH=...
    NcbWL.*OneOverTauEsccbSCH2WL.*ThermEsc_Barrier_reductionSCH;
%[1,NumSlices] Tunneling processes from WL to SCH in reversely biased
    slices [ns^-1]
TunnelingFromWL2SCH=Tunneling_esc_rateWELL_cb.*NcbWL;
%[NumPops,NumSlices] Tunneling processes from ES2 to WL in reversely
    biased slices [ns^-1]
TunnelingFromES22SCH=TunnelingEscapeRatecbES2.*NcbES2;
%[NumPops,NumSlices] Tunneling processes from ES1 to ES2 in reversely
    biased slices [ns^-1]
TunnelingFromES12SCH=TunnelingEscapeRatecbES1.*NcbES1;
%[NumPops,NumSlices] Tunneling processes from GS to ES1 in reversely
    biased slices [ns^-1]
TunnelingFromGS2SCH=TunnelingEscapeRatecbGS.*NcbGS;

%[1,NumSlices] Variation of carriers in the cb SCH [ns^-1]
dNcbSCH= ...
     %[1,NumSlices] Net Current in cb including drift sweep out [ns^-1]
```

```
    NetCurrentCB ...
    %[1,NumSlices] Non radiative recombination [ns^-1]
    -NonRadiativeRecombinationSCH ...
    %[1,NumSlices] Capture from SCH to WL [ns^-1]
    -CaptureFromSCH2WL ...
    %[1,NumSlices] Escape from WL [ns^-1]
    +EscapeFromWL2SCH ...
    %[1,NumSlices] Tunneling processes from WL to SCH [ns^-1]
    +TunnelingFromWL2SCH...
    +sum(...
        %[NumPops,NumSlices] tunneling process from GS states [ns^-1]
        TunnelingFromGS2SCH...
        %[NumPops,NumSlices] tunneling process from ES1 states [ns^-1]
        +TunnelingFromES12SCH...
        %[NumPops,NumSlices] tunneling process from ES2 states [ns^-1]
        +TunnelingFromES22SCH);
```

In `dNcbSCH`, we can recognize the various components of the theoretical equation. We can also see that there are some tunneling components, that are not present in the theoretical formula. These represent the carriers that are able to tunnel from the SCH directly to all the other states of the QD. These contributions are introduced even though they are not that significant with respect to the others.

Let's continue with the rate equation for the Wetting Layer (WL). From the theoretical analysis of Chapter 3, we know that the equation reads:

$$\frac{\partial N_{WL}}{\partial t} = +\frac{N_{SCH}}{\tau_{c,WL}} - \frac{N_{WL}}{\tau_{e,WL}} - \frac{B_{WL}}{Wh_W}N_{WL}^2 - \frac{N_{SCH}}{\tau_{nr,SCH}} - \\ - \frac{N_{WL}^3}{\tau_{Aug,ES_2}} - \sum_{i=1}^{N}\frac{G_i}{\tau_{c,ES_2}}N_{WL}(1-\rho_{iES_2}) + \sum_{i=1}^{N}\frac{N_{iES_2}}{\tau_{e,ES_2}}$$

Here we have the capture from and escape to the SCH, the spontaneous emission, the non-radiative and the Auger contributions. Moreover, the two summations represent the capture and escape contributions from and to the QD confined energy states, considering the chirp and the inhomogeneous distribution. This equation is implemented in the program as follows:

```
 %%%%% Variation of WL carriers %%%%%

%[1,NumSlices] Product of carrier in cb and vb in SCH [ns^-1]
NcbvbWL=NcbWL.*NvbWL;
%[1,NumSlices] rate of non radiative recomb. in WL [ns^-1]
NonRadiativeRecombinationWL=sqrt(NcbvbWL).*OneOverTauNRcbWL;
%[1,NumSlices] rate of spontaneous emission in WL [ns^-1]
SpontaneousEmissionWL=Bsp.*NcbvbWL;
```

```
%[1,NumSlices] rate of Auger recomb. in WL [ns^-1]
AugerRecombinationWL=NcbWL.^3.*OneOverTauAugerWL;
%[NumPops,NumSlices] rate of capture from ES2 to WL [ns^-1]
CaptureFromES22WL=...
    ((1-RhocbES2).*OneOverTauCapcbWL2ES2).*(InhomDensityES2*NcbWL);
%[NumPops,NumSlices] rate of escape from ES2 to WL [ns^-1]
EscapeFromES22WL=...
    NcbES2.*OneOverTauEsccbES22WL.*ThermEsc_Barrier_reductionWL;
%[1,NumSlices] rate of recombinations in the WL [ns^-1]
RecombinationWL=...
    %[1,NumSlices] rate of non radiative recomb. in WL [ns^-1]
    NonRadiativeRecombinationWL+...
     %[1,NumSlices] rate of spontaneous emission in WL [ns^-1]
    SpontaneousEmissionWL+...
    %[1,NumSlices] rate of Auger recomb. in WL [ns^-1]
    AugerRecombinationWL;

 %[1,NumSlices] Variation of carriers in the cb WL [ns^-1]
dNcbWL=...
    %[1,NumSlices] rate of capture from SCH to WL [ns^-1]
    CaptureFromSCH2WL ...
    %[1,NumSlices] rate of escape from SCH to WL [ns^-1]
    -EscapeFromWL2SCH ...
     %[1,NumSlices] rate of recombinations in the WL [ns^-1]
    -RecombinationWL ...
    +sum(...
        %[NumPops,NumSlices] rate of escape from ES2 to WL [ns^-1]
        EscapeFromES22WL ...
        %[NumPops,NumSlices] rate of capture from ES2 to WL [ns^-1]
        -CaptureFromES22WL) ...
    %[1,NumSlices] Tunneling processes from WL to SCH [ns^-1]
    -TunnelingFromWL2SCH;
```

In `dNcbWL`, we can recognise all the contributions present in the equation. We have indeed the term `CaptureFromSCH2WL` representing the capture rate from the SCH, `EscapeFromWL2SCH` representing the escape rate from the WL to the SCH, `RecombinationWL` containing the spontaneous, non-radiative and Auger contributions and, finally, `sum(EscapeFromES22WL-CaptureFromES22WL)` corresponding to the two summations in the theoretical equation, which represent the capture and escape rates from and to the QD confined states. In additions to these, we have also `TunnelingFromWL2SCH` that is linked to tunneling processes between WL and SCH, which is not reported in the theoretical equation and which describes tunneling processes that may be relevant when simulating reversely biased sections.

Continuing on with the rate equations, let's concentrate on the one for the second

excited state (ES2), the considered QD confined state with the highest energy. From the theoretical model, we know that:

$$\begin{aligned}\frac{\partial N_{iES_2}}{\partial t} = &+\frac{G_i}{\tau_{c,ES_2}} N_{WL}(1-\rho_{iES_2}) - \frac{N_{iES_2}}{\tau_{e,ES_2}} - \\ &- \frac{N_{iES_2}}{\tau_{c,ES_1}}(1-\rho_{iES_1}) + \frac{N_{iES_1}}{\tau_{e,ES_1}}(1-\rho_{iES_2}) - \\ &- \frac{N_{iES_2}\rho_{iES_2}}{\tau_{sp,ES_2}} - \frac{\rho^2_{iES_2}}{\tau_{Aug,ES_2}} N_{iES_2} - \frac{N_{iES_2}}{\tau_{nr,ES_2}} - \mathcal{R}_{st,iES_2}\end{aligned}$$

Here we can see the capture and escape rates between WL and ES2 and between ES1 and ES2. There are also the spontaneous emission, Auger, non-radiative and stimulated emission contributions.
This is implemented in `DDoSimulationOpt` with these lines of code:

```
%%%%% Variation ES2 carriers %%%%%
%%%%% I assume no stimulated emission/absorption processes %%%%%

 %[1,1] false: solve CB and VB separately, true: use eccitonic model
     [bool]
if Data.Excitonic==0
    %[NumPops,NumSlices] rate of Auger recombination in ES2 [ns^-1]
    AugerRecombES2=...
        RhovbES2.*RhocbES2.*RhocbES2.* ...
        (DotNumberTimesDegOverTauAugercbES2);
    %[NumPops,NumSlices] rate of spontaneous emission in ES2 [ns^-1]
    SpontaneousEmissionES2=NcbES2.*RhovbES2*OneOverTauSpontES2;
else
    %[NumPops,NumSlices] rate of Auger recombination in ES2 [ns^-1]
    AugerRecombES2=...
        (RhocbES2.*RhocbES2.*RhocbES2).* ...
        (DotNumberTimesDegOverTauAugercbES2);
    %[NumPops,NumSlices] rate of spontaneous emission in ES2 [ns^-1]
    SpontaneousEmissionES2=NcbES2.*RhocbES2*OneOverTauSpontES2;
end

%[NumPops,NumSlices] Non radiative recomb. from ES2 [ns^-1]
NonRadiativeRecombES2=NcbES2.*OneOverTauNRcbES2;
%[NumPops,NumSlices] rate of escape from ES1 to ES2 [ns^-1]
EscapeFromES12ES2=NcbES1.*(1-RhocbES2).*OneOverTauEsccbES12ES2;
%[NumPops,NumSlices] capture rate from ES2 to ES1 [ns^-1]
CaptureFromES22ES1=NcbES2.*(1-RhocbES1).*OneOverTauCapcbES22ES1;
%[NumPops,NumSlices] Stimulated emission from ES2 [ns^-1]
StimulatedEmissionES2=...
    StimulatedEmissionCoeffES2XY.*GainES2(:,:,cc).*DeltaEnergyES2;
```

```
%[NumPops,NumSlices] rate of recombinations in the ES2 [ns^-1]
RecombinationsES2=...
    %[NumPops,NumSlices] Non radiative recomb. from ES2 [ns^-1]
    NonRadiativeRecombES2+ ...
    %[NumPops,NumSlices] rate of spontaneous emission in ES2 [ns^-1]
    SpontaneousEmissionES2+ ...
    %[NumPops,NumSlices] rate of Auger recombination in ES2 [ns^-1]
    AugerRecombES2+ ...
    %[NumPops,NumSlices] Stimulated emission from ES2 [ns^-1]
    StimulatedEmissionES2;

%[NumPops, NumSlices] Variation of carriers in the cb ES2 [ns^-1]
dNcbES2= ...
    %[NumPops,NumSlices] rate of capture from ES2 to WL [ns^-1]
    CaptureFromES22WL ...
    %[NumPops,NumSlices] rate of recombinations in the ES2 [ns^-1]
    -RecombinationsES2...
    %[NumPops,NumSlices] rate of escape from ES2 to WL [ns^-1]
    -EscapeFromES22WL ...
    %[NumPops,NumSlices] rate of escape from ES1 to ES2 [ns^-1]
    +EscapeFromES12ES2...
    %[NumPops,NumSlices] capture rate from ES2 to ES1 [ns^-1]
    -CaptureFromES22ES1...
    %[NumPops,NumSlices] tunneling process from ES2 states [ns^-1]
    -TunnelingFromES22SCH;
```

In this portion of code, we can see that, first of all, depending on the value of `Data.Excitonic`, we can either adopt the independent rate equation model or the excitonic one for the computation of the Auger and spontaneous emission rates. The choice is still maintained, even though the simulations will be carried out only considering the excitonic model with `Data.Excitonic = 1`. After the computation of the various terms, we compute the variation of the carriers in the conduction band ES2 (`dNcbES2`). In `dNcbES2`, we can recognize `CaptureFromES22WL` and `EscapeFromES22WL` representing respectively the capture rate from WL and the escape rate from ES2 to WL. Then there are `CaptureFromES22ES1` and `EscapeFromES22ES1`, that represent the capture and escape rates between ES2 and ES1. Moreover, we have once again the variable `RecombinationsES2`, that contains the rates for all the recombination phenomena affecting ES2, namely the spontaneous and stimulated emission and the non-radiative and Auger recombination rates. In particular, if we concentrate on the stimulated emission term (`StimulatedEmissionES2`), it is in a slightly different form with respect to the one employed in Chapter 4 in Equation (3.36). Indeed, it is closer to the expression presented in [9], where we have the gain, the confinement factor and a factor A_m

containing some important constants:

$$\mathcal{R}_{st,im} = v_g \mu_m N_D \frac{\Gamma^+ + \Gamma^-}{2} A_m \frac{V_{QD}}{h_{QD}} (2\rho_{im} - 1) dz \tag{5.5}$$

Note that a tunneling contribution (`TunnelingFromES22SCH`) is present. This represents the possible carriers escaping ES2 towards the SCH by means of tunneling phenomena.

For the first excited state ES1, we will have similar contributions, taking into account its interactions with ES2 and GS. The theoretical model, as we know from Chapter 3, tells us that the variation of the carriers in ES1 is regulated by the following equation:

$$\begin{aligned}\frac{\partial N_{iES_1}}{\partial t} = &+\frac{N_{iES_2}}{\tau_{c,ES_1}}(1-\rho_{iES_1}) - \frac{N_{iES_1}}{\tau_{e,ES_1}}(1-\rho_{iES_2}) - \\ &- \frac{N_{iES_1}}{\tau_{c,GS}}(1-\rho_{iGS}) + \frac{N_{iGS}}{\tau_{e,GS}}(1-\rho_{iES_1}) - \\ &- \frac{N_{iES_1}\rho_{iES_1}}{\tau_{sp,ES_1}} - \frac{\rho_{iES_1}^2}{\tau_{Aug,ES_1}} N_{iES_1} - \frac{N_{iES_1}}{\tau_{nr,ES_1}} - \mathcal{R}_{st,iES_1}\end{aligned}$$

In this equation we can recognize the escape and capture rates between ES1 and ES2, the escape and capture rates between GS and ES1 and the various recombination phenomena (spontaneous, Auger, non-radiative and stimulated). This is then implemented in the simulator as follows:

```
%%%%% Variation ES1 carriers %%%%%

%[1,1] false: solve CB and VB separately, true: use eccitonic model
    [bool]
if Data.Eccitonic==0
    %[NumPops,NumSlices] rate of Auger recombination in ES1 [ns^-1]
    AugerRecombES1=...
        RhovbES1.*RhocbES1.*RhocbES1.* ...
        DotNumberTimesDegOverTauAugercbES1;
    %[NumPops,NumSlices] rate of spontaneous emission in ES1 [ns^-1]
    SpontaneousEmissionES1=NcbES1.*RhovbES1*OneOverTauSpontES1;
else
    %[NumPops,NumSlices] rate of Auger recombination in ES1 [ns^-1]
    AugerRecombES1=...
        (RhocbES1.*RhocbES1.*RhocbES1).* ...
        DotNumberTimesDegOverTauAugercbES1;
    %[NumPops,NumSlices] rate of spontaneous emission in ES1 [ns^-1]
    SpontaneousEmissionES1=NcbES1.*RhocbES1*OneOverTauSpontES1;
```

```
end

%[NumPops,NumSlices] rate of escape from GS to ES1 [ns^-1]
EscapeFromGS2ES1=NcbGS.*(1-RhocbES1).*OneOverTauEsccbGS2ES1;
%[NumPops,NumSlices] capture rate from ES1 to GS [ns^-1]
CaptureFromES12GS=NcbES1.*(1-RhocbGS).*OneOverTauCapcbES12GS;
%[NumPops,NumSlices] Non radiative recomb. from ES1 [ns^-1]
NonRadiativeRecombES1=NcbES1*OneOverTauNRcbES1;
%[NumPops,NumSlices] Stimulated emission from ES1 [ns^-1]
StimulatedEmissionES1=...
    StimulatedEmissionCoeffES1XY.*GainES1(:,:,cc).*DeltaEnergyES1;
 %%[1,NumSlices] rate of recombinations in the ES1 [ns^-1]
RecombinationsES1=...
    %[NumPops,NumSlices] Non radiative recomb. from ES1 [ns^-1]
    NonRadiativeRecombES1+ ...
    %[NumPops,NumSlices] rate of Auger recombination in ES1 [ns^-1]
    AugerRecombES1+ ...
    %[NumPops,NumSlices] rate of spontaneous emission in ES1 [ns^-1]
    SpontaneousEmissionES1+ ...
    %[NumPops,NumSlices] Stimulated emission from ES1 [ns^-1]
    StimulatedEmissionES1;

%[NumPops, NumSlices] Variation of carriers in the cb ES1 [ns^-1]
dNcbES1= ...
    %[NumPops,NumSlices] capture rate from ES2 to ES1 [ns^-1]
    CaptureFromES22ES1 ...
    %[NumPops,NumSlices] rate of recombinations in the ES1 [ns^-1]
    -RecombinationsES1 ...
     %[NumPops,NumSlices] rate of escape from ES1 to ES2 [ns^-1]
    -EscapeFromES12ES2 ...
    %[NumPops,NumSlices] rate of escape from GS to ES1 [ns^-1]
    +EscapeFromGS2ES1 ...
    %[NumPops,NumSlices] capture rate from ES1 to GS [ns^-1]
    -CaptureFromES12GS...
    %[NumPops,NumSlices] tunneling process from ES1 states [ns^-1]
    -TunnelingFromES12SCH;
```

Once again, we can see that the various contributions are computed (the Auger and spontaneous emission ones change whether we are considering the excitonic approximation or not). Then, in `dNcbES1`, representing the variation of the carrier in the conduction band ES1 state at the current time step, we can recognize the various terms that were present in the theoretical equation. Indeed, we can recognize `CaptureFromES22ES1` and `EscapeFromES12ES2` representing respectively the capture rate from ES2 and the escape rate from ES1 to ES2, that

were already present, with opposite sign, in the ES2 rate equation. Then there are `CaptureFromES12GS` and `EscapeFromGS2ES1`, that represent the capture and escape rates between ES1 and GS. Moreover, we have once again the variable `RecombinationsES1`, that contains the rates for all the recombination phenomena affecting ES1, namely the spontaneous and stimulated emission and the non-radiative and Auger recombination rates. In this case as well, we have a tunneling contribution `TunnelingFromES12SCH`, representing the carriers that escape ES1 toward the SCH by means of tunneling phenomena. Note that the stimulated emission rate is in the form of Equation (5.5).

Finally, let's analyse how the ground state GS rate equation is implemented in the `DDoSimulationOpt` simulator. From theory, we know that the variation of the number of carriers in GS is described by:

$$\frac{\partial N_{iGS}}{\partial t} = +\frac{N_{iES_1}}{\tau_{c,GS}}(1-\rho_{iGS}) - \frac{N_{iGS}}{\tau_{e,GS}}(1-\rho_{iES_1}) - \\ - \frac{N_{iGS}\rho_{iGS}}{\tau_{sp,GS}} - \frac{\rho_{iGS}^2}{\tau_{Aug,GS}}N_{iGS} - \frac{N_{iGS}}{\tau_{nr,GS}} - \mathcal{R}_{st,iGS}$$

Here, the escape and capture rates between ES1 and GS and the various recombination phenomena (spontaneous, Auger, non-radiative and stimulated) are present, similarly to what we had before for the other QD confined states. This is then implemented in the MATLAB program as follows:

```
%%%%% Variation of the GS carriers %%%%%

%[1,1] false: solve CB and VB separately, true: use eccitonic model
    [bool]
if Data.Eccitonic==0
    %[NumPops,NumSlices] rate of Auger recombination in GS [ns^-1]
    AugerRecombGS=...
        RhovbGS.*RhocbGS.*RhocbGS.* ...
        DotNumberTimesDegOverTauAugercbGS;
    %[NumPops,NumSlices] rate of spontaneous emission in GS [ns^-1]
    SpontaneousEmissionGS=NcbGS.*RhovbGS*OneOverTauSpontGS;
else
    %[NumPops,NumSlices] rate of Auger recombination in ES2 [ns^-1]
    AugerRecombGS=...
        (RhocbGS.*RhocbGS.*RhocbGS).* ...
        DotNumberTimesDegOverTauAugercbGS;
    %[NumPops,NumSlices] rate of spontaneous emission in WL [ns^-1]
    SpontaneousEmissionGS=NcbGS.*RhocbGS*OneOverTauSpontGS;
end

%[NumPops,NumSlices] Stimulated emission from GS [ns^-1]
```

```
StimulatedEmissionGS=...
    StimulatedEmissionCoeffGSXY.*GainGS(:,:,cc).*DeltaEnergyGS;
%[NumPops,NumSlices] Non radiative recomb. from GS [ns^-1]
NonRadiativeRecombGS1=NcbGS*OneOverTauNRcbGS;
%[NumPops,NumSlices] rate of recombinations in the GS [ns^-1]
RecombinationsGS=...
    %[NumPops,NumSlices] Non radiative recomb. from GS [ns^-1]
    NonRadiativeRecombGS1+ ...
    %[NumPops,NumSlices] rate of spontaneous emission in GS [ns^-1]
    SpontaneousEmissionGS+ ...
    %[NumPops,NumSlices] Stimulated emission from GS [ns^-1]
    StimulatedEmissionGS+ ...
    %[NumPops,NumSlices] rate of Auger recombination in GS [ns^-1]
    AugerRecombGS;

%[NumPops, NumSlices] variation of GS carriers [ns^-1]
dNcbGS=...
    %[NumPops,NumSlices] capture rate from ES1 to GS [ns^-1]
    CaptureFromES12GS...
    %[NumPops,NumSlices] rate of recombinations in the GS [ns^-1]
    -RecombinationsGS ...
    %[NumPops,NumSlices] rate of escape from GS to ES1 [ns^-1]
    -EscapeFromGS2ES1...
    %[NumPops,NumSlices] Tunneling processes from GS to ES1 in reversely
        biased slices [ns^-1]
    -TunnelingFromGS2SCH;
```

Unsurprisingly, we have here as well the computation of the various terms and, finally, in `dNcbGS`, we can find the terms that are making up the theoretical formula. There are of course `CaptureFromES12GS` and `EscapeFromGS2ES1`, that represent the capture and escape rates between ES1 and GS. They were already present in `dNcbES1`, but with opposite sign. Moreover, we have once again a variable `RecombinationsGS`, that contains the rates for all the recombination phenomena affecting GS, namely, just like for the other confined QD states, the spontaneous and stimulated emission and the non-radiative and Auger recombination rates. Finally, we have also the tunneling term `TunnelingFromGS2SCH`, with the same meaning as that of its ES1 and ES2 counterparts.

Up to now, we computed only the variation of the carriers in each considered energy state. These variation terms are then used in order to compute the total number of carriers in each slice, at the current time step, for all the considered QD states. This is simply done by summing the computed variation terms to the total number of carriers at the previous time step.

```
% I compute the new values for carriers in each slice at time t
```

```
%[1,NumSlices] Number of carriers for SCH in cb [-]
NcbSCH=NcbSCH+Sim.subsampleRE*Sim.dt*dNcbSCH;
%[1,NumSlices] Number of carriers for WL in cb [-]
NcbWL=NcbWL+Sim.subsampleRE*Sim.dt*dNcbWL; NcbWL(NcbWL<0)=0;
%[NumPops,NumSlices] Number of carriers for ES2 in cb [-]
NcbES2=NcbES2+Sim.subsampleRE*Sim.dt*dNcbES2;
%[NumPops,NumSlices] Number of carriers for ES1 in cb [-]
NcbES1=NcbES1+Sim.subsampleRE*Sim.dt*dNcbES1;
%[NumPops,NumSlices] Number of carriers for GS in cb [-]
NcbGS=NcbGS+Sim.subsampleRE*Sim.dt*dNcbGS;

% I calculate the occupation probabilities in the QD states
%[NumPops,NumSlices] Occupation probability for ES2 in cb [-]
RhocbES2=NcbES2./DotNumberByDegeneracyES2;
%[NumPops,NumSlices] Occupation probability for ES1 in cb [-]
RhocbES1=NcbES1./DotNumberByDegeneracyES1;
%[NumPops,NumSlices] Occupation probability for GS in cb [-]
RhocbGS=NcbGS./DotNumberByDegeneracyGS;

[...]

%[1,1] false: solve CB and VB separately, true: use eccitonic model
    [bool]
if Data.Excitonic % EXCITONIC MODEL
    %[1,NumSlices] Number of carriers for SCH [-]
    NvbSCH=NcbSCH;
    %[1,NumSlices] Number of carriers for WL in cb [-]
    NvbWL=NcbWL;
    %[NumPops,NumSlices] Number of carriers for ES2 in cb [-]
    NvbES2=NcbES2;
    %[NumPops,NumSlices] Number of carriers for ES1 in vb [-]
    NvbES1=NcbES1;
    %[NumPops,NumSlices] Number of carriers for GS in vb [-]
    NvbGS=NcbGS;
    %[NumPops,NumSlices] Occupation probability for ES2 in vb [-]
    RhovbES2=RhocbES2;
    %[NumPops,NumSlices] Occupation probability for ES1 in vb [-]
    RhovbES1=RhocbES1;
    %[NumPops,NumSlices] Occupation probability for GS in vb [-]
    RhovbGS=RhocbGS;
    %[1,NumSlices] Net Current in vb [ns^-1]
    NetCurrentVB=NetCurrentCB;
else          % INDEPENDENT MODEL

[...]
```

```
46
47 end
```

Note that, in this code, we use directly the number of carriers (adimensional quantity) instead of the density of carriers, which is perhaps of more common use in the theoretical treatment. For this reason, since the variation terms that we computed before are expressed in ns^{-1}, we multiply those by the time step of the simulation `dt`, before adding them to the number of carriers computed in the previous step. We also compute the occupation probability ρ in conduction band, by normalizing the number of carriers in each confined state by the total number of available states (number of QDs times the degeneracy for that particular energy state).
Then, of course, since we are employing the excitonic approximation, both the number of carriers and the occupation probabilities in valence band are set to be equal to those in conduction band. Inside the `else` statement, the computations for the independent rate equation model are contained. This is not reported for the sake of brevity, but, for instance, in that case, the probability distributions are expressed by means of the Fermi-Dirac probability distribution.
This is the last step of the computation of the number of carriers following the rate equation model, except for the models of the phase noise of the field and the spontaneous emission noise, both modelled as random noise sources. Therefore, in order to conclude the numerical implementation of the model, given the number of carriers in each QD state at the current time step, of course we have to implement the solution of the field propagation equations in order to compute the values of the forward and backward components of the field inside the device, at the current time step.

5.3.3 Field propagation equations

As anticipated, the rate equations only describe the carrier dynamics, but we have also to include the implementation of the equations modelling the propagation of the progressive and regressive components of the field, according to what has been obtained in Chapter 3. In particular, we want to implement the time stepped solution of the travelling wave equation, that is represented by Equation (3.24) and that is reported here for the sake of clarity:

$$\begin{aligned} E^{\pm}(z_0 \pm \Delta z, t) = &+ S^{\pm}_{sp}(z_0, t) + E^{\pm}(z_0, t - \Delta t) - \frac{\alpha^{\pm}_w}{2} E^{\pm}(z_0, t - \Delta t)\Delta z + \\ &+ \Delta z \sum_m g^0_{im}(2\rho_{im}(z_o, t - \Delta t) - 1) I^{\pm}_{im}(z_0, t - \Delta t) \end{aligned}$$

This equation was implemented by means of a set of coefficients, using a similar approach to the one of the appendix of [1]. This set includes `A` (progressive and regressive), `B` (progressive and regressive, in micrometer times square root of

electronvolt), `Tmp` (progressive and regressive, in micrometers time square root of electronvolt) and `sumEsp` (progressive and regressive, in square root of electronvolt), which is related to the spontaneous emission. These coefficients include the field filtered by a Lorentzian filter, the gain and the field at the previous temporal step, which are, of course, also the building blocks of Equation (3.24). The final implementation for the field at the current time step (`Sprog` and `Sregr`, in square root of electronvolt) also include a variable taking into account losses (`ComplexLossesProg` and `ComplexLossesRegr`, in one over micrometer).

All of this is implemented in MATLAB as follows:

```
 %[NumPops,NumSlices COMPLEX] Expanded forward field [sqrt(eV)]
SProgccExpanded=onesNumQDPopulations*Sprog(cc,:);
%[NumPops,NumSlices COMPLEX] Expanded backward field [sqrt(eV)]
SRegrccExpanded=onesNumQDPopulations*Sregr(cc,:);

%[1,1] Include the Kerr effect? [bool]
if KerrCoefficient==0
    %[1,NumSlices] Forward field material losses [um^-1]
    MaterialKerrLossesProg=MaterialLossesHalfedProg;
    %[1,NumSlices] Backward field material losses [um^-1]
    MaterialKerrLossesRegr=MaterialLossesHalfedRegr;
else
    %[1,NumSlices COMPLEX] Forward field material losses [um^-1]
    MaterialKerrLossesProg=...
        complex(MaterialLossesHalfedProg, ...
        -KerrCoefficient*(PowerRegr+PowerRegr));
    %[1,NumSlices COMPLEX] Backward field material losses [um^-1]
    MaterialKerrLossesRegr=...
        complex(MaterialLossesHalfedRegr, ...
        -KerrCoefficient*(PowerRegr+PowerRegr));
end
%[1, NumSlices COMPLEX] Forward complex losses [um^-1]
ComplexLossesProg=...
    -(MaterialKerrLossesProg+LossesPlasmaEffect(pp,:)+ ...
      1i*dn_plasma(pp,:));
%[1, NumSlices COMPLEX] Backward complex losses [um^-1]
ComplexLossesRegr=...
    -(MaterialKerrLossesRegr+LossesPlasmaEffect(pp,:)+ ...
      1i*dn_plasma(pp,:));

if ReferenceFreq == 0    % GS reference

[...]

elseif ReferenceFreq == 1 % reference between ES1 and GS
```

```
36
37 [...]
38
39 elseif ReferenceFreq == 2 % reference between ES2 and GS
40     %[1,NumSlices COMPLEX] A coefficient for the forward field [-]
41     Aprog=(...
42         sum(...
43             ModalGainGSpp.*RatioExpGS...
44             +ModalGainES1pp.*RatioExpES1...
45             +ModalGainES2pp.*RatioExpES2 ...
46             )...
47         +ComplexLossesProg...
48         )*Halfdz;
49
50     %[1,NumSlices COMPLEX] A coefficient for the backward field [-]
51     Aregr=(...
52         sum(...
53             ModalGainGSpp.*RatioExpGS...
54             +ModalGainES1pp.*RatioExpES1...
55             +ModalGainES2pp.*RatioExpES2 ...
56             )...
57         +ComplexLossesRegr...
58         )*Halfdz;
59
60     %[1,NumSlices COMPLEX] B coeff for the forward field [um^-1 sqrt(eV)]
61     Bprog=sum(...
62             ModalGainGSpp.*(FilterCoeffGS.*IfieldGSprog(:,:,cc)+...
63             RatioExpGS.*FilterCoeffGS.*SProgccExpanded)...
64             +ModalGainES1pp.*(FilterCoeffES1.*IfieldES1prog(:,:,cc)+...
65             RatioExpES1.*FilterCoeffES1.*SProgccExpanded)...
66             +ModalGainES2pp.*(FilterCoeffES2.*IfieldES2prog(:,:,cc)+...
67             RatioExpES2.*FilterCoeffES2.*SProgccExpanded)...
68             );
69
70     %[1,NumSlices COMPLEX] B coeff for the backward field[um^-1 sqrt(eV)]
71     Bregr=sum(...
72             ModalGainGSpp.*(FilterCoeffGS.*IfieldGSregr(:,:,cc)+...
73             RatioExpGS.*FilterCoeffGS.*SRegrccExpanded)...
74             +ModalGainES1pp.*(FilterCoeffES1.*IfieldES1regr(:,:,cc)+...
75             RatioExpES1.*FilterCoeffES1.*SRegrccExpanded)...
76             +ModalGainES2pp.*(FilterCoeffES2.*IfieldES2regr(:,:,cc)+...
77             RatioExpES2.*FilterCoeffES2.*SRegrccExpanded)...
78             );
79 end
80
```

```
81  if sum(Aprog>1)>0
82      disp('Warning: too large time step')
83  end
84  if sum(Aregr>1)>0
85      disp('Warning: too large time step')
86  end
87
88  %[1,NumSlices] Field material losses [um^-1]
89  ComplexLossesProg=...
90      4/dz/2-(MaterialKerrLossesProg+
            LossesPlasmaEffect(pp2,:)+1i*dn_plasma(pp2,:));
91  %[1,NumSlices] Field material losses [um^-1]
92  ComplexLossesRegr=...
93      4/dz/2-(MaterialKerrLossesRegr+
            LossesPlasmaEffect(pp2,:)+1i*dn_plasma(pp2,:));
94
95  %[1,NumSlices COMPLEX] Tmp coeff for the forward field [um^-1 sqrt(eV)]
96  TmpProg=(...
97      ComplexLossesProg.*Sprog(pp2,:)...
98      +ComplexLEFGS*sum(ModalGainGS(:,:,pp2).*IfieldGSprog(:,:, pp2)) ...
99      +ComplexLEFES1*sum(ModalGainES1(:,:,pp2).*IfieldES1prog(:,:,pp2))...
100     +ComplexLEFES2*sum(ModalGainES2(:,:,pp2).*IfieldES2prog(:,:,pp2))...
101     );
102 %[1,NumSlices COMPLEX] Tmp coeff for the backward field [um^-1 sqrt(eV)]
103 TmpRegr=(...
104     ComplexLossesRegr.*Sregr(pp2,:)...
105     +ComplexLEFGS*sum( ModalGainGS(:,:,pp2).*IfieldGSregr(:,:, pp2))...
106     +ComplexLEFES1*sum(ModalGainES1(:,:,pp2).*IfieldES1regr(:,:,pp2))...
107     +ComplexLEFES2*sum(ModalGainES2(:,:,pp2).*IfieldES2regr(:,:,pp2))...
108     );
109
110 %[NumSavedStates,NumSlices COMPLEX] New forward field [sqrt(ev)]
111 Sprog(pp,2:end)=...
112     Halfdz./(1-Aprog(2:end)).* ...
113     (TmpProg(1:end-1)+Bprog(2:end))+sumEspProg(1:end-1);
114 %[NumSavedStates,NumSlices COMPLEX] New backward field [sqrt(ev)]
115 Sregr(pp,1:end-1)=...
116     Halfdz./(1-Aregr(1:end-1)).* ...
117     (TmpRegr(2:end)+Bregr(1:end-1))+sumEspRegr(2:end);
```

Note that here only the implementation of the solution for the ES2 reference is reported for the sake of brevity, but the code still offers the possibility of choosing the other two frequency references, each with their slightly different solution for the time-stepped travelling wave equation. If all the coefficients in `Sprog` and `Sregr` and all the terms in the coefficients themselves are expanded, we get two equations

that are indeed very similar to Equation (3.24), despite some small differences due to the fact that the implemented model is less approximated with respect to that of the theory.
Another aspect that is missing is the enforcement of the boundary conditions given by the residual reflectivity of the facets, according to Equations (3.4) and (3.5), that couple the forward and backward components in $z = 0$ and $z = L$ through r_0 and r_L. In reality, in the code, contrary to these equations, the boundary conditions and the optical excitation are included separately.

```
%[NumSavedStates,NumSlices COMPLEX] Forward field BC [sqrt(eV)]
Sprog(pp,1)=Halfdz./(1-Aprog(1)/2).*...
            (...
            Bprog(1) ...
            +r0.*(TmpRegr(1)+Sregr(pp2,1)/Halfdz))/2;

%[NumSavedStates,NumSlices COMPLEX] Backward field BC [sqrt(eV)]
Sregr(pp,end)=Halfdz./(1-Aregr(end)/2).*...
            (...
            Bregr(end) ...
            +rL.*(TmpProg(end)+Sprog(pp2,end)/Halfdz))/2;
```

Indeed, `Sregr(pp2,1)` in `Sprog(pp,1)` represents the regressive component in the first slice, at the previous time instant; `Sprog(pp2,end)` in `Sregr(pp,end)` represents the regressive component in the last slice, at the previous time instant.

5.3.4 Optical excitation and external feedback

Finally, even though the external optical source and the external feedback have been introduced in the previous sections about `DeviceData_SOA` and `MainSOA`, it is still necessary to model them in `DDoSimulationOpt`, by implementing how they change the propagation of the progressive and regressive components of the field.
Starting from the optical excitation, first it is important to define the signal coming out of the source. This is done simply by using the handle function defined in `MainSOA`, passing the vector `t` containing the discrete time instants the simulation runs upon. Since this function is defined in square root of milliwatt as unit of measure, but the simulator mostly employs the electronvolt, it is mandatory to use a properly-defined conversion factor between them. After its definition earlier in the code, after the computation of the solution of the progressive and regressive components of the field in the device, we have to include the optical excitation in `Sprog`. This is simply done by summing the value of the optical excitation at the current time instant to the modulus of the progressive field in first slice of the device, at the current time instant. Incidentally, this is also why we have to flip the structure in the double-pass configuration: we employ the experimental configuration and the optical excitation has to be fed to the first slice of the device.

```
if Sim.IncludeOpticalExcitation            %External excitation
    %[1,NumSlices] update first slice forward propagating field with
        external excitation [eV^0.5]
    Sprog(pp,1) = Sprog(pp,1)+OpticalExcitation(it);
end
```

This is indeed just the sum of `OpticalExcitation(it)` to the progressive component of the field in the first slice.

Concerning the external feedback, it is what allows us to use the double-pass configuration. This is pretty much just a mirror placed outside the device output facet. Therefore, from the standpoint of the field, we have to consider the forward propagating field exiting the device and we have to compute the field that is then coupled back in the device after a reflection on the external mirror. Of course, this field in the external cavity has to be summed to the regressive component of the field in the device. The implementation of these concepts is reported here:

```
if IncludeExtFeedback        %External feedback injected in the cavity
    if isnumeric(rF)
        %field just after the feedback external facet
        EFilteredFeedback(kFeedback)=...
            EFeedback(kFeedback)*rF;
        Res.Field.Ext(nextindextosavefield)=...
            EFeedback(kFeedback)*tF;
    else
        EFilteredFeedback(kFeedback)=...
            rF(EFeedback,EFilteredFeedback,kFeedback);
        Res.Field.Ext(nextindextosavefield)=...
            sqrt(abs(EFeedback(kFeedback)).^2 ...
            -abs(EFilteredFeedback(kFeedback)).^2);
    end
    Res.Field.Ext(nextindextosavefield)= ...
        sqrt(abs(EFeedback(kFeedback)).^2-...
        abs(EFilteredFeedback(kFeedback)).^2);
    Sregr(pp,end)= Sregr(pp,end)+ ...
        EFilteredFeedback(kFeedback)*FeedbackPropagationSingle*tL;
    EFeedback(kFeedback) = (Sprog(pp,end)*tL+...
    EFilteredFeedback(kFeedback)*FeedbackPropagationSingle*...
        (-rL))*FeedbackPropagationSingle;

    if kFeedback==NumSlicesF
        kFeedback=1;
    else
        %[1,1] Position in EFeedback for the next iteration [#]
        kFeedback=kFeedback+1;
    end
```

```
30 end
```

This concludes the analysis of the MATLAB simulator: after this we only have the set up of the variables for the next iteration of the loop and, once we are out of the loop, we have the storing of the results in the `Res.mat` and `State.mat` files. At this point we are ready to tackle the actual simulations of the device in the various configurations and their results.

Chapter 6

Simulation results

In the previous chapter, we extensively examined the MATLAB implementation of the theoretical model presented in Chapter 3. In this final chapter, we are ready to dive into the results of the simulations, in order to assess how well the simulator is reproducing the experimental results of the articles. In particular, three main sets of experiments will be carried out:

- **continuous wave** (CW) experiments, where the device is simply biased through the two-section electrodes by means of CW currents, without an external optical excitation. The device is operated in single-pass configuration and its behaviour corresponds to a superluminescent diode. This is used in order to investigate the spectral asymmetry features of the device under test. The obtained results are compared to the results of [9] and [8];
- **single-pass** experiments in presence of an optical excitation. This kind of simulations can be for instance exploited in order to inspect the effects of this device on the amplification of picosecond optical pulses. The obtained results are compared to those of [7];
- **double-pass** experiments in presence of an optical excitation. This kind of simulations can be used in order to compare the performances of the device in this double-pass configuration, with respect to those of the same device in a single-pass configuration. The obtained results are compared to those of [7].

The data describing the device employed for these simulations are of course the same that have been presented in Chapter 5, but, depending on the kind of simulation (single- or double-pass configuration), longer-lasting simulations might be mandatory to get stable results. For instance, for the simulations of the first group, 10 ns of duration are sufficient, because it is enough for the device to get to a steady average output power level. On the contrary, for the pulse analysis, this duration is not sufficient because, before turning on the pulsed optical source, we

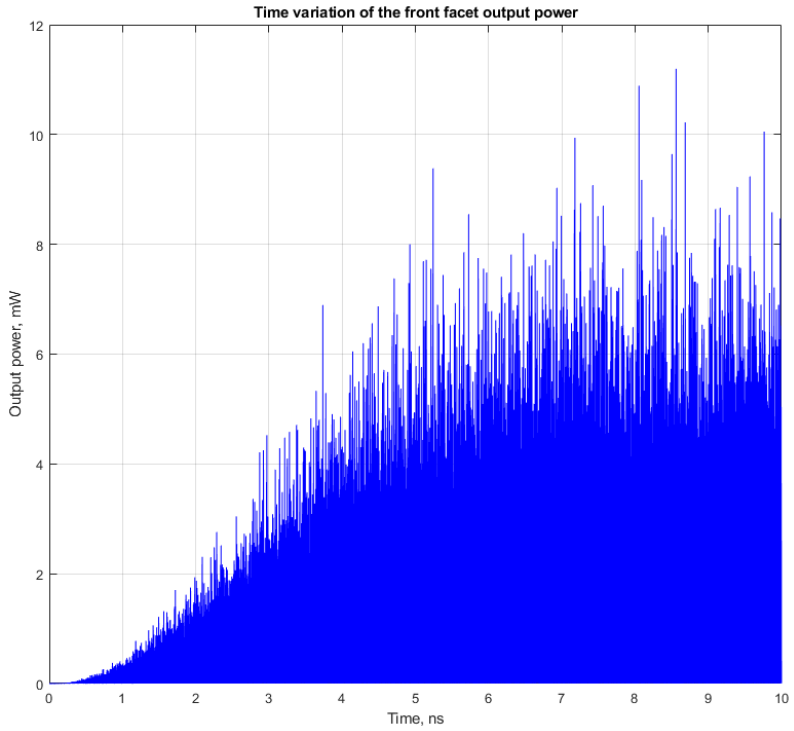

Figure 6.1. Simulated time evolution of the output power at the front facet, with $I_{Front} = 1\,\text{A}$ and $I_{Rear} = 0.2\,\text{A}$, without optical excitation.

must make sure that the device in the steady state. The simulation time step, by contrast, is kept fixed to 15 fs, because it is a good compromise between simulation speed and simulation precision.

6.1 CW simulations

In this section, we concentrate on the CW experiments, where the device is operated by applying a proper driving current to each of the two electrodes, without injecting an external light source. In this case, it is basically working as a superluminescent diode (SLED), which is emitting mostly through spontaneous emission like any other LED, but reaching much higher values of output power, thanks to the length of the structure. Indeed, thanks to the more sizeable dimensions with respect to a canonical pn junction, the spontaneously-emitted light is also amplified, thus allowing the emission of higher output powers. These simulations aim to reproduce the experiments performed in [8] and [9].
For this first class of simulations, the `TEnd` is set to 10 ns, because it is sufficient to obtain stable values of output power (on the average). This is simply proved by comparing the results of simulations with variable duration and observing that

they do not change that much if we consider longer-lasting ones. For instance, in Figure 6.1, it is possible to see that, after 10 ns, the output power is already stable on the average, despite some outliers caused by the spontaneous emission random noise.
First, in order to understand if the behaviour of the simulated device is in accordance with the experimental results, we analyse the light-current characteristic, namely the evolution of the power at the facets of the device with respect to the current density. In particular, for this first plot, let's consider a situation in which the two electrodes are driven in such a way that the current density is constant throughout the device (uniform injection). According to [9], the front and rear sections have a contact area of $3.3 \times 10^{-3}\,\mathrm{cm}^2$ and $6 \times 10^{-4}\,\mathrm{cm}^2$ respectively, meaning that the rear section current has to be 5.5 times smaller than the front section one in order to have a constant current density.

Note: This light-current characteristic has been employed in order to determine the modified parameters of Table 5.1. As already mentioned, this was done with a trial-and-error approach, modifying the parameters of interest and looking at the light-current characteristic, until finding a set of parameters giving good agreement with the experimental data.

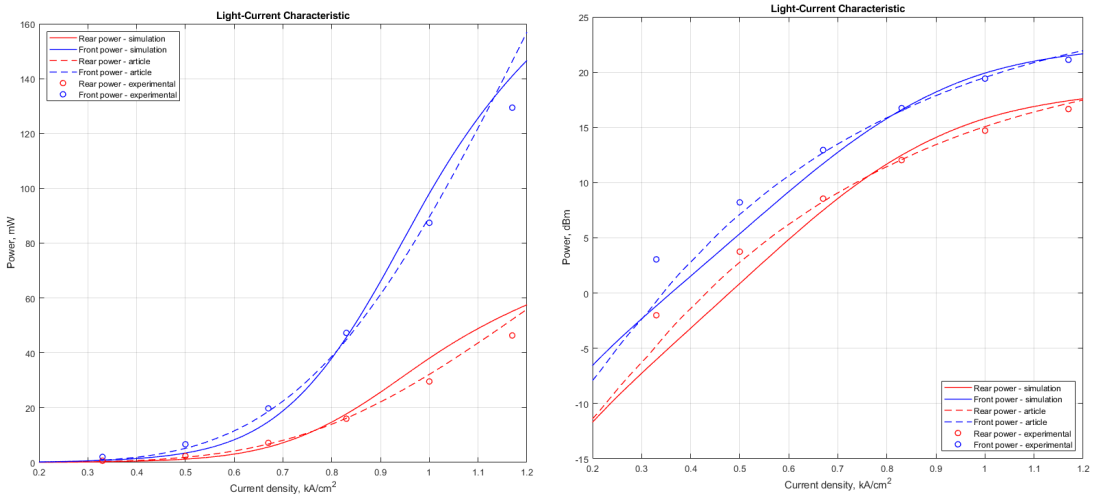

(a) **(b)**

Figure 6.2. (a) Light-current characteristic with constant current density, in linear scale. (b) Light-current characteristic with constant current density, in logarithmic scale. Experimental data of [9] taken from [23].

Figures 6.2a and 6.2b represent the light-current characteristic with constant current density in linear and logarithmic scales, respectively. In these graphs, the solid lines represent the results of the performed simulations, while the dashed lines and the dots are associated to the simulations and the experimental data of [9]. The red

lines are linked to the rear facet power, while the blue ones to the front facet. If we concentrate on Figure 6.2b, there is quite good agreement with the experimental data. The characteristic, indeed, has almost linear behaviour for lower current densities (exponential growth in linear scale), but then the growth is slower. It is possible to take notice that, at lower current densities between $0.3\,\mathrm{kA/cm^2}$ and $0.8\,\mathrm{kA/cm^2}$, the agreement between the results of the simulations and those of [9] is lower. This should not constitute that much of a problem since this kind of devices is usually operated at higher current densities, since, there, we have higher gain – and output power. This is supported by the fact that, in Figure 6.2a, in that range of currents, the difference is not that substantial. In general, the profile in the linear plot is reproducing quite well the one of the data.
In reality, it should be possible to achieve even better agreement by modifying further the parameters of Table 5.1 with the usual trial-and-error approach that was already employed to get to the results of Figure 6.2a and 6.2b.

It could be also interesting to investigate the evolution of the occupation probability with respect to the current density. Of course, increasing the current, we expect to have a higher occupation probability, since we have a higher number of available carriers that can occupy the states. In particular, we expect to have a higher probability for the lower energy states, both within the same layer (ground state vs. excited states) and between the different layers (the lowest ground state vs. the other two).
Figures 6.3a, 6.3b and 6.3c, represent the evolution of the occupation probabilities with respect to the current density. Just like in the previous plots, the red and blue lines are associated to the rear and front facets respectively. On these images we also distinguish the behaviour of the three QD layers creating the active material of the device (solid, dashed and dash-dotted lines). We can see that the behaviour of the occupation probability follows the expectations: given a value of current density, the ground state probability is higher with respect to the one of the first excited state, which is higher than that of the second excited state in its turn. Not only this, we can also see that, for a given energy state and a given current density value, the probability is higher for the QD layer with lower central energy. This doesn't come as a surprise since the carrier should start to occupy the energy states from the one at lowest energy. In general, the occupation probability tends to increase quite rapidly at lower current densities and to subsequently saturate to a constant value, however it is also possible to notice in all three images that the red curves reach a maximum and decrease before saturating. This phenomenon is linked to the fact that, at such high current densities, we have an output power so high that the carriers populations are depleted faster than they are able to be replenished. This is the reason why we obtain this decrease of the occupation probability and it is also congruent with the saturation of the output power for both facets.

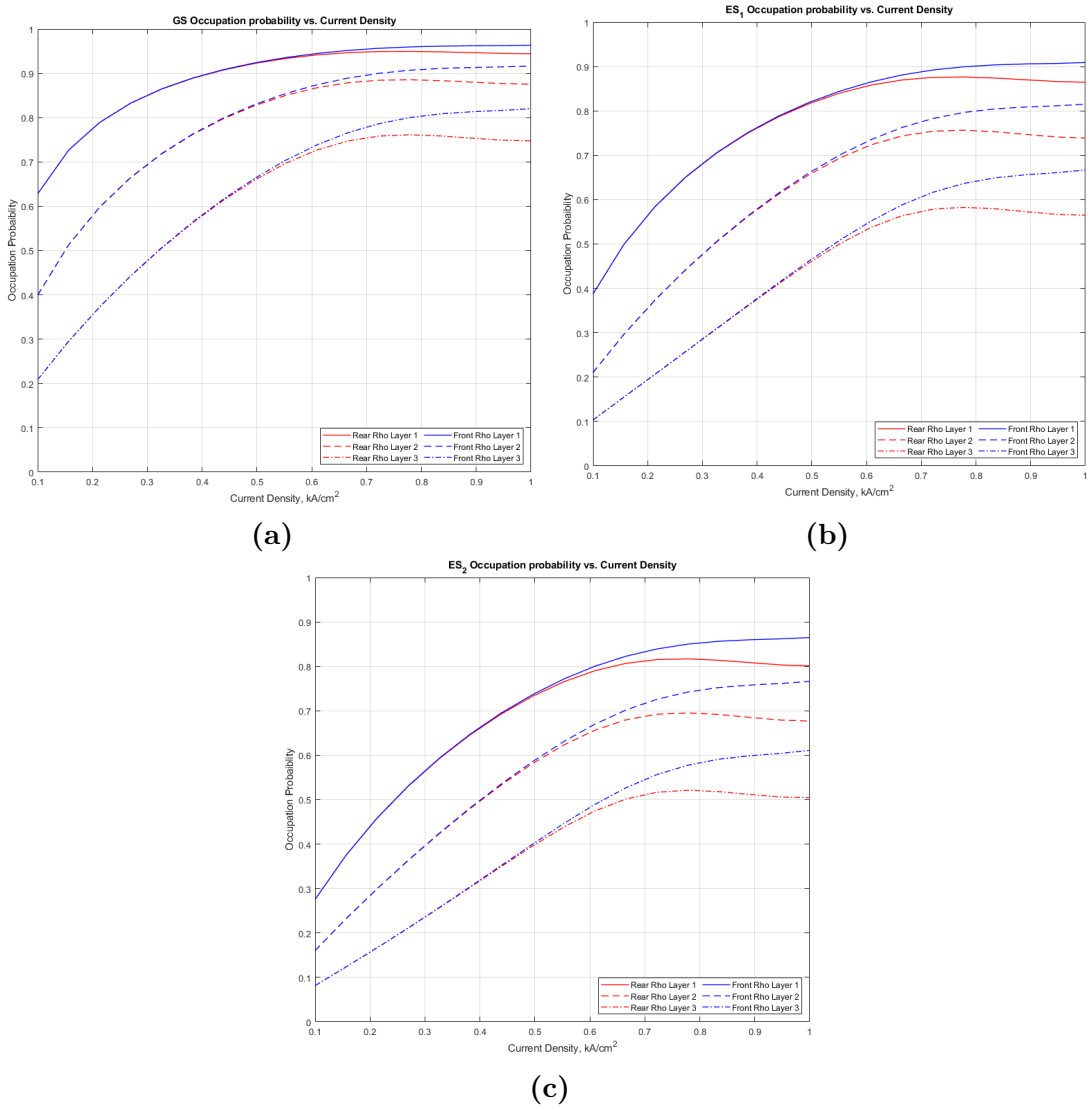

Figure 6.3. (a) Evolution of the GS occupation probability with respect to the current density. (b) Evolution of the ES1 occupation probability with respect to the current density. (c) Evolution of the ES2 occupation probability with respect to the current density.

We can now continue on with the analysis of the device under asymmetric biasing conditions: in this case the two electrodes are not driven in order to have a constant current density in the device, but with two different values of current in the two sections. First, let's study again the light-current characteristic in this configuration. In this case, the idea is to choose some fixed values for the rear section current and simulate multiple values of front section current for each one of them, thus obtaining a light-current characteristic for each one of these fixed values of rear section current.

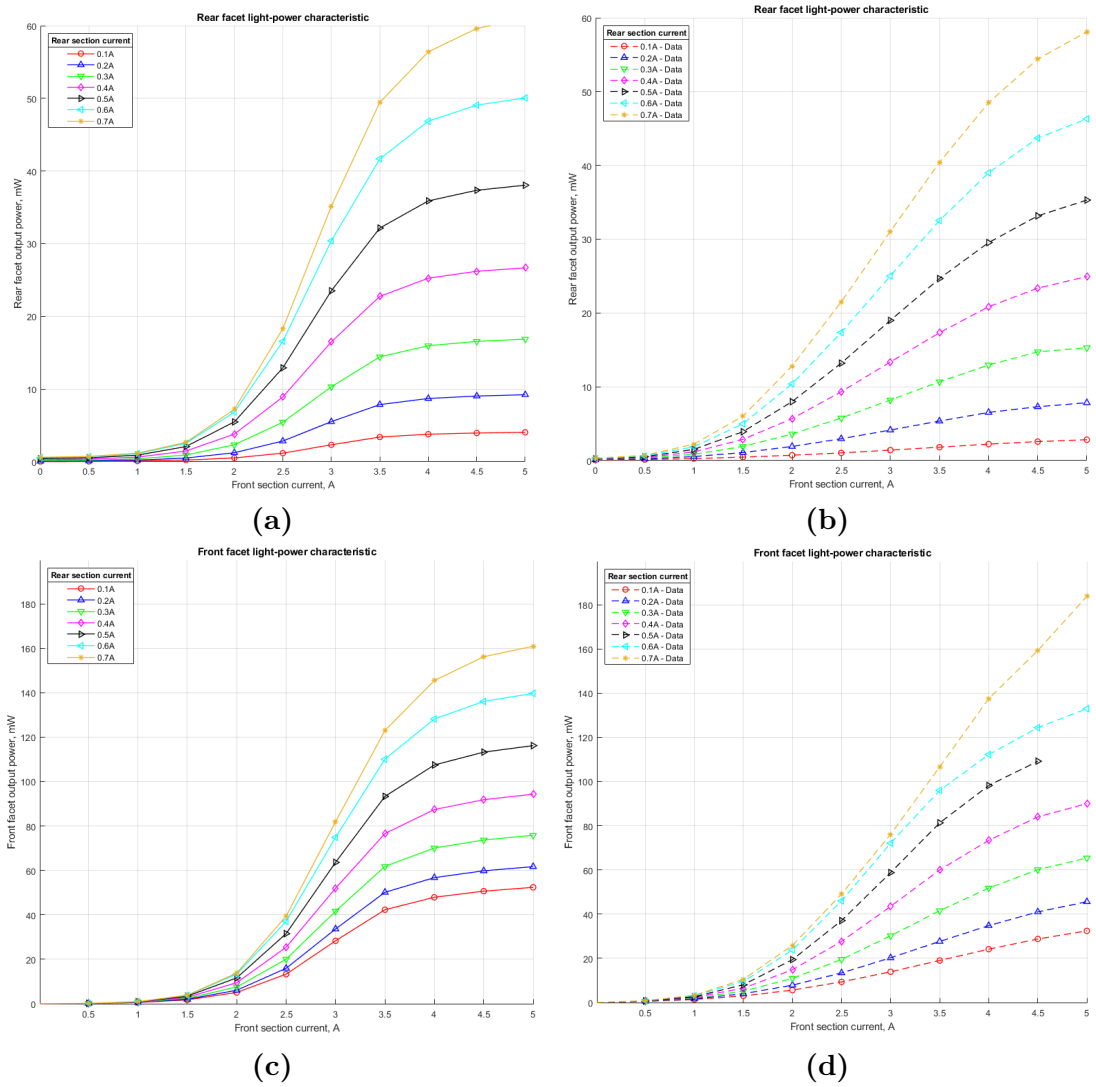

Figure 6.4. (a) Simulated light-current characteristic for the rear facet power. (b) Light-current characteristic for the rear facet power from [9], data taken from [23]. (c) Simulated light-current characteristic for the front facet power. (d) Light-current characteristic for the front facet power from [8], data taken from [22].

Figures 6.4 contain the light current characteristics for rear and output power resulting from the performed simulations (left column) and from the experimental measurements of [8] and [9] (right column). On these, the curves with different colours represent the light-current characteristic for a specific value of rear section current. By comparing the rear facet and front facet powers of Figures 6.4a and 6.4c, we can see that, of course, the latter is characterised by higher values, as we already know from the constant density light-current characteristic of Figure 6.2b.

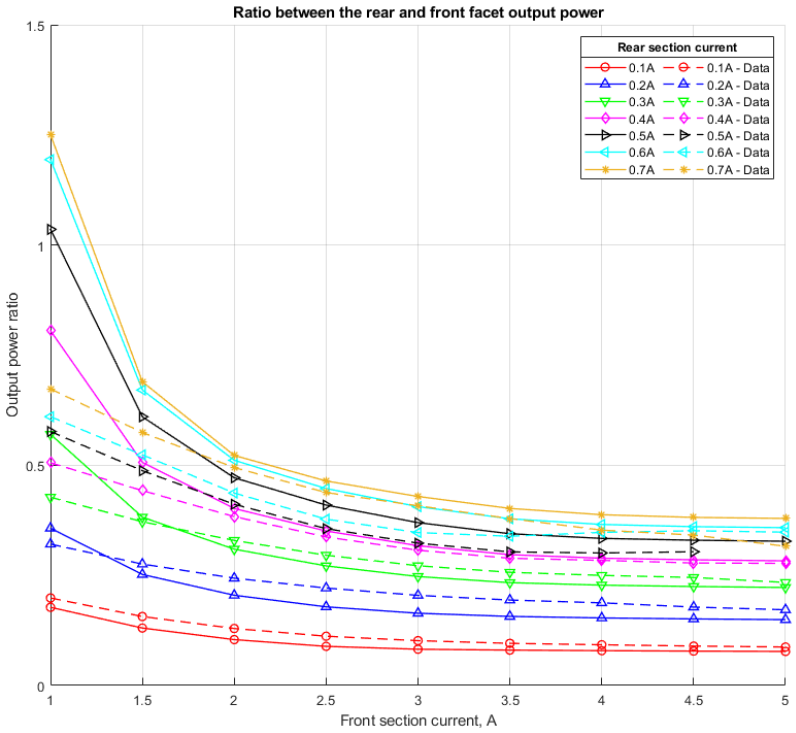

Figure 6.5. Simulated current characteristic of the ratio between front and rear facet output power. Data taken from [22] and [23].

Furthermore, if we compare the simulation results with the experimental data, we can see that the profiles in the two cases are basically the same. However, it is easy to observe that the results of the simulations are characterised in general by higher values of output power (mostly within 3 dB). This could be due to the fact that the experimental measurements are done with involved setups (Figure 4.3), made of multiple non-ideal components that could easily introduce some degree of loss, that of course is not present in the simulated device.

For this reason, the profile of the ratio between the two output powers could be a more insightful indicator. In theory, if the simulated profiles of front and rear facet output powers are reproducing well those of the experimental data, only with higher values, the experimental ratio should be well reproduced. If we analyse Figure 6.5, it is possible to state that this is true especially for low values of rear section current (0.1-0.4 A). Then the accordance is slightly worsened, particularly with high rear section current and low front section current. This is reflecting what we already had in the constant current density analysis of Figure 6.2b. In this particular case, we have that the ratio is higher for small front section currents (especially 1 A) with respect to the experimental data. This means that, there, the increase of front section power relative to its experimental counterpart is smaller than the one of rear section power. This is in line with the results of the constant

current density analysis.

After this extensive analysis of the output power characteristic, it is also important to analyse the behaviour of the device in the frequency domain, namely its spectrum. In order to study the power spectrum, the Discrete Fourier Transform is employed. After the conversion to the frequency domain, a convolution operation is performed between the power spectrum and a vector of constant values in order to smooth out the otherwise noisy spectrum.
As discussed in [9], this device is characterised by a particular feature: a spectral asymmetry is observed between the front and rear facet output and, by driving the two electrodes separately, it is possible to tune this asymmetry, effectively enhancing it. This feature introduces the possibility of an additional degree of freedom for bandwidth engineering, multiplexing the output of the two facets in the optical domain. Now, we can exploit the TDTW simulator and check whether it can predict this wide tunable spectral asymmetry or not. The idea is basically to keep the rear current fixed but varying the front section current and study the spectrum.

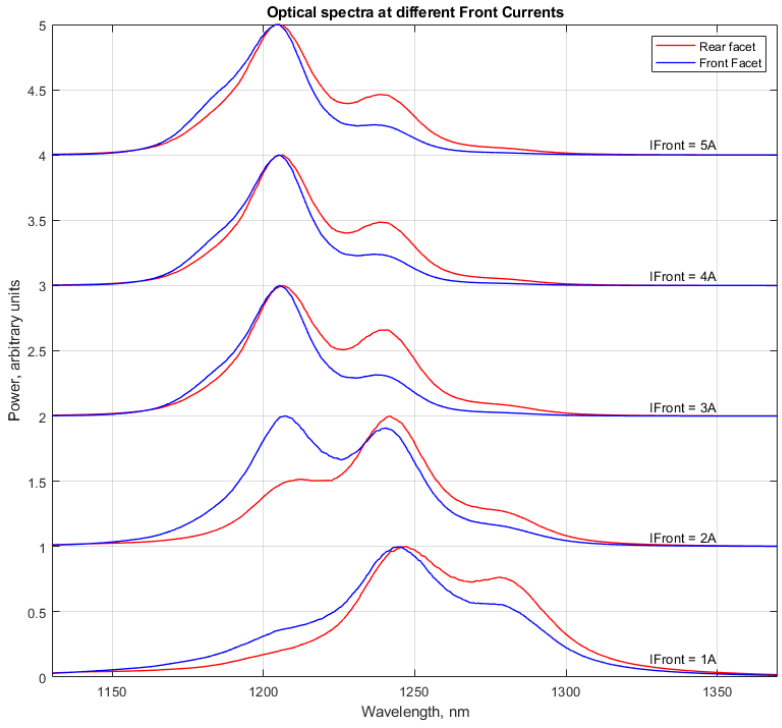

Figure 6.6. Simulated front and rear output spectra with fixed $I_{Rear} = 0.1\,\text{A}$, varying the I_{Front} between 1 A and 5 A. The spectra have been normalized and plotted one on top of the other for graphical clarity.

In particular, the rear section current is kept fixed at 0.1 A, while the front section one is increased with steps of 1 A from 1 A to 5 A. These values should give us

insight on the spectral asymmetry and the simulation results are already available from the non-constant current density light-current characteristic analysis. The results of the analysis are reported in Figure 6.6, where, as always, the red curves are associated to the rear facet, while the blue ones to the front one. Note that the plots in this picture are normalized (arbitrary units) and represented together for a better comparison. From Figure 6.6, it is clear that the tunability effect is present. Indeed, increasing the front section current, the spectrum seems to be shifted toward lower wavelengths, because of the modification of which states are occupied and contribute to the emission. The spectral asymmetry, namely the different profile of the spectra associated to the front and rear facet, although present, it doesn't seem to be enhanced by the increased asymmetry between the two driving currents, contrary to the experimental results. Concerning the spectral components that are giving their contribution, it is possible to say that they are in line with the experimental results: for $I_{Rear} = 0.1\,\mathrm{A}$ and $I_{Front} = 1\,\mathrm{A}$, there are two main peaks at $\simeq 1245\,\mathrm{nm}$ and at $\simeq 1280\,\mathrm{nm}$. The latter loses weight increasing the front section current. Another peak at $\simeq 1210\,\mathrm{nm}$ appears, but it is not present in the experimental results. These three components are corresponding basically to the three GS central emission wavelengths of the three populations of QD layers, therefore it is not surprising that they are the main contributors to the emission. Since the peak close to 1210 nm is not present in the experimental results, the cause for a reduced spectral asymmetry tunability in the TDTW simulations could be how the QD energy levels are filled up for increasing values of driving current.

In reality, another spectrum that can be investigated is the gain one, which will give us more information regarding which levels are absorbing (negative gain) and which ones are emitting (positive gain).

Figures 6.7a and 6.7b contain the gain spectra for front and rear facets for two different driving current configurations ($I_{Rear} = 0.1\,\mathrm{A}$ and $I_{Front} = 1\,\mathrm{A}$ in 6.7a, $I_{Rear} = 0.1\,\mathrm{A}$ and $I_{Front} = 3.5\,\mathrm{A}$ in 6.7b). As always, the blue curves are associated to the front facet, while the red ones to the rear facet. Starting from Figure 6.7a ($I_{Front} = 1\,\mathrm{A}$), it is possible to state that the results are in qualitative agreement with the ones of [9]. Indeed, the front facet gain has two maxima located in the vicinity of 1250 nm (dashed green line) and of 1275 nm (dashed magenta line), which are the components of the experimental power spectrum (also found in Figure 6.6). The peak close to 1250 nm is most likely related to the second layer GS and the first layer ES1, while the one close to 1275 nm is most likely related to the first layer GS. For these wavelengths, the value of gain is $\simeq 4\,\mathrm{cm}^{-1}$, which is in line with the results of [9]. For wavelengths shorter than $\simeq 1210\,\mathrm{nm}$, this front facet gain is negative, meaning that the QD states are absorbing. Concerning the rear facet gain, it is mostly negative, except for the neighborhood of 1275 nm, where it becomes positive and reaches a maximum for that wavelength, with a value of $\simeq 1\,\mathrm{cm}^{-1}$. The only discrepancy with respect to [9] is the range of wavelength between 1140 nm and 1210 nm, because in this case the device seems to be absorbing less (gain $\simeq -5\,\mathrm{cm}^{-1}$

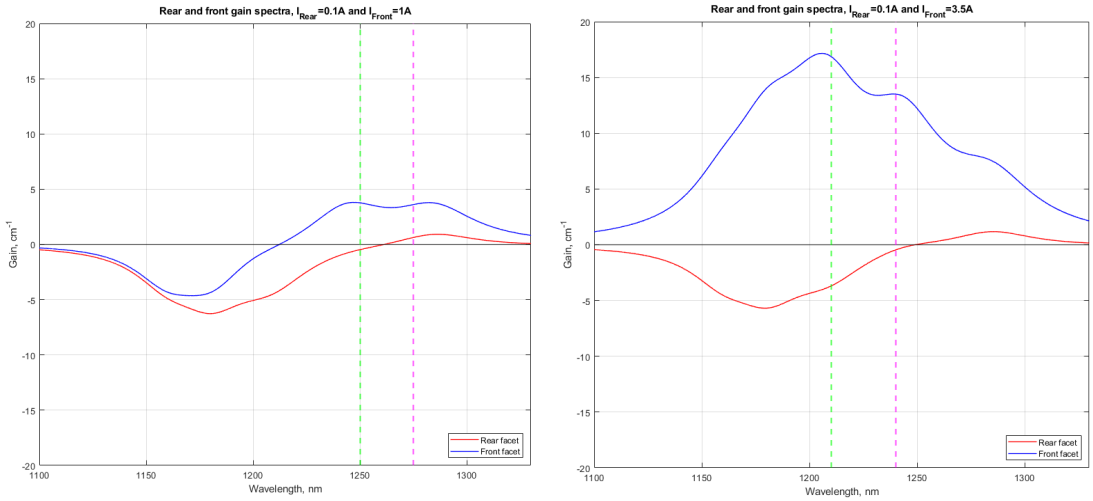

(a) **(b)**

Figure 6.7. (a) Simulated gain spectrum for the front and rear facets, with $I_{Rear} = 0.1\,\text{A}$ and $I_{Front} = 1\,\text{A}$. (b) Simulated gain spectrum for the front and rear facets, with $I_{Rear} = 0.1\,\text{A}$ and $I_{Front} = 3.5\,\text{A}$.

instead of $\simeq -10\,\text{cm}^{-1}$).

Concerning Figure 6.7b ($I_{Front} = 3.5\,\text{A}$), in this case as well, the agreement with the results of [9] is good. Indeed, the front facet gain spectrum has two visible local maxima. One is located in the proximity of 1210 nm (green dashed line) and it is most likely related to the third layer GS, the second layer ES1 and first layer ES2. This peak has a height of $\simeq 17\,\text{cm}^{-1}$, which is in line with the results from the article. Then, the second local maximum is located in proximity of 1240 nm (magenta dashed line), most likely related to the to the second layer GS and the first layer ES1. This peak, instead, has a height of $\simeq 14\,\text{cm}^{-1}$, like its counterpart in [9]. Just like in the experimental results, a lower peak located near 1280 nm is visible, corresponding to a gain of $\simeq 7\,\text{cm}^{-1}$, which is most likely related first layer GS. Concerning the rear facet gain spectrum, once again, it is possible to safely state that there is good accordance with the results of the article. Indeed, in this case the gain spectrum is negative (absorption) up until 1250 nm and it increases until reaching a maximum located in 1280 nm, with gain $\simeq 1\,\text{cm}^{-1}$, once again related to the first layer GS. In this case as well, the only discrepancy with respect to [9] is the range of wavelength between 1140 nm and 1210 nm, where the two curves resulting from the simulations are yielding higher values of gain. For instance, the rear facet gain spectrum has a minimum in 1180 nm with value $\simeq -7\,\text{cm}^{-1}$, instead of $\simeq -12\,\text{cm}^{-1}$. This range of wavelengths is associated to the second layer ES2 and third layer ES1 and ES2; the fact that the gain is too high in Figures 6.7a and 6.7b and that we have a new peak in the high current spectra of Figure 6.6, could be a problem of how these states are filled during the simulation.

This could be easily solved with further tweaking of the simulation parameters of Table 5.1.
Of course, the total amplifying capabilities of the SOA will be given by the evolution of the gain across the whole structure, therefore it is important to study the position-wavelength map of the total gain. Let's first analyse the gain map for the same configuration that was studied previously ($I_{Rear} = 0.1\,\text{A}$ and $I_{Front} = 1\,\text{A}$).

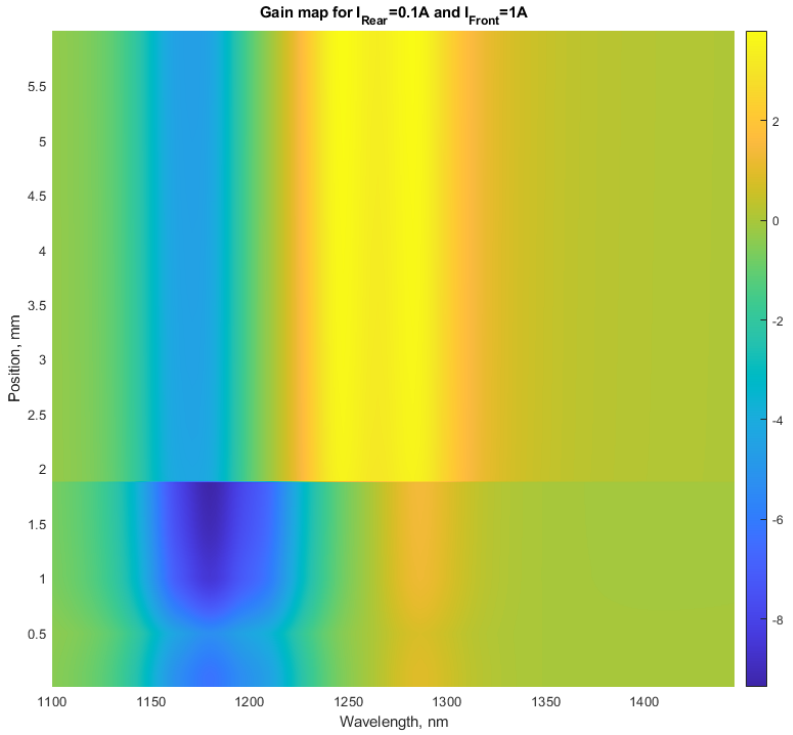

Figure 6.8. Simulated gain map with respect to position and wavelength for $I_{Rear} = 0.1\,\text{A}$ and $I_{Front} = 1\,\text{A}$.

From Figure 6.8, we can see, first of all, a net separation located at $z = 1.875\,\text{mm}$, which corresponds to the position where the two electrodes are separated by means of an insulation trench. Moreover, another clear spatial separation is located at $z = 0.5\,\text{mm}$, which is where the straight waveguide section ends and the first tapering begins. In reality, there is also the transition between first to second tapered section at $z = 1\,\text{mm}$, but it is much less clearly visible. Concerning the distribution of the gain, it is basically reproducing what we had in Figure 6.7a. Indeed, at $z = 0\,\text{mm}$ (rear facet), we have strong absorption between 1140 nm and 1210 nm, but then the gain starts increasing until reaching a maximum of $\simeq 1\,\text{cm}^{-1}$, located around 1275 nm. The profile is kept approximately constant up until the insulation trench, with the only notable difference that we have stronger absorption in the region between 1140 nm and 1210 nm. From the trench to the front facet, we have a spatially-constant distribution of gain, that corresponds to the spectrum

of front facet gain of Figure 6.7a. Indeed, we have a high gain region between 1210 nm and 1310 nm, with two maxima at 1250 nm and 1275 nm, where the gain has value $\simeq 4\,\mathrm{cm}^{-1}$. As already mentioned, the gain is constant up until the front facet: this could be related to the fact that the driving current is not high enough to saturate the gain itself.
Therefore, let's analyse the simulation results with much higher driving currents ($I_{Rear} = 0.7\,\mathrm{A}$ and $I_{Front} = 5\,\mathrm{A}$).

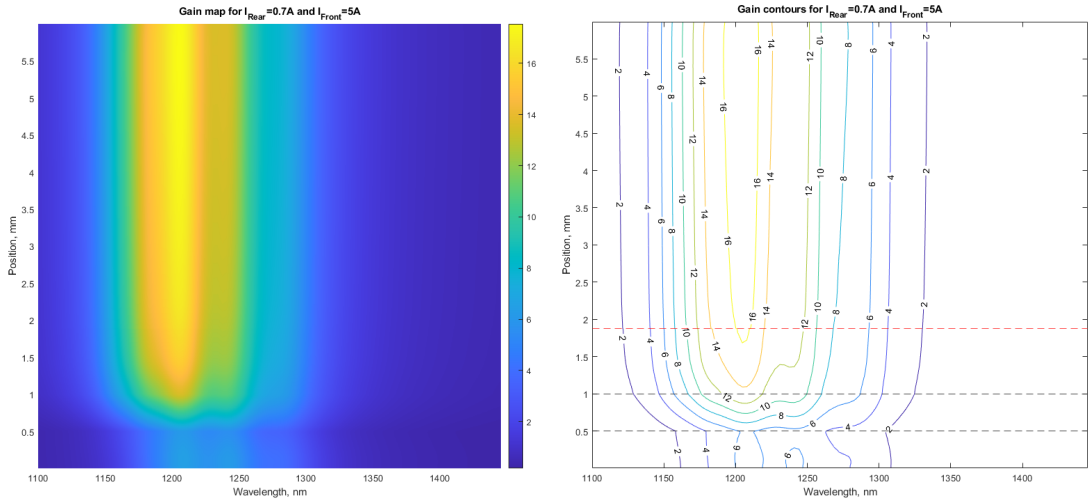

(a) **(b)**

Figure 6.9. (a) Simulated gain map with respect to position and wavelength for $I_{Rear} = 0.7\,\mathrm{A}$ and $I_{Front} = 5\,\mathrm{A}$. (b) Simulated gain contour map with respect to position and wavelength for $I_{Rear} = 0.7\,\mathrm{A}$ and $I_{Front} = 5\,\mathrm{A}$.

In Figure 6.9a, the gain map for $I_{Rear} = 0.7\,\mathrm{A}$ and $I_{Front} = 5\,\mathrm{A}$ is reported. Figure 6.9b, represents the contours of this gain map, for a better understanding of the distribution. In this case, we can see that the only net separation corresponds to the transition between the straight and tapered sections at 0.5 mm, while the insulation trench does not seem to have a visible effect on the gain distribution. In this case, in accordance with the power spectra of Figure 6.6, there is positive gain between 1250 nm and 1310 nm, but the main spectral component is located at 1210 nm, with a value of $\simeq 16\,\mathrm{cm}^{-1}$. In the straight waveguide section, the gain is characterised by much lower values ($\simeq 6\,\mathrm{cm}^{-1}$ utmost).
Concerning the profile of the gain, it is clear that it remains constant all throughout the tapered sections, despite the fact that, in this case, we could expect to have a reduction of the gain due to the strong increase of emitted photons, that is concurrent to a depletion of the carriers populations. This means that the taper of the device is designed in such a way that it is able to compensate the reduction of the carriers with the increase of the surface, hence the constant gain distribution.

6.2 Single- and double-pass simulations

In the previous section, we extensively discussed the results of the simulations of the device under CW biasing conditions, where it behaves as a SLED. Let's abandon these conditions and let's continue with the analysis of its behaviour under external optical excitation. In this case, the device is actually operated as a SOA, exploiting its amplifying capabilities in order to boost the power of a pulsed source as the one reported in Figure 5.3a. In the simulations, both the single- and double-pass configurations are employed and compared, reproducing the experiments of [7]. Therefore, it is reasonable to expect, as found experimentally, to have that the double-pass configuration has higher gain with respect to the single-pass one, but without significant pulse degradation.

The simulations are set to last 20 ns. This is done because the pulsed light source is turned on after 10 ns, in order to let the SOA reach a steady ASE output power first. As already discussed in Chapter 4, the external source is characterized by a central emission wavelength of 1258 nm, pulse repetition rate of 50 GHz, pulse duration of 2.3 ps and average pulse power of 2.5 mW. Since the pulse repetition rate is 5 GHz and the source is left on for 10 ns, 50 pulses are amplified by the device.

Let's start by analysing in general the obtained results. First, it has to be noted that, due to the employment of different configurations, in which the device is flipped, the output power has to be taken from the front facet in the double-pass case and from the rear facet in the single-pass one.

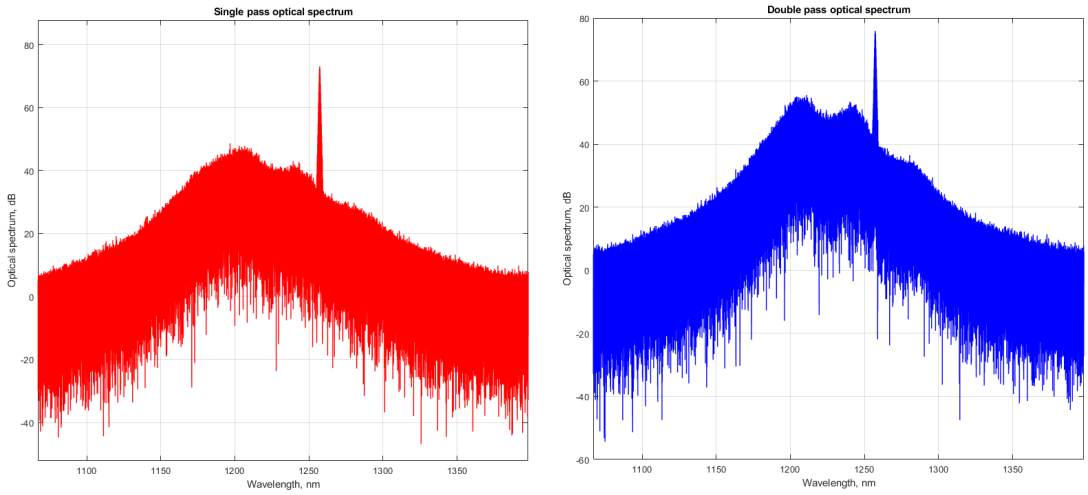

(a) **(b)**

Figure 6.10. (a) Simulated optical output spectrum in single-pass configuration, with $I_{Rear} = 0.3$ A and $I_{Front} = 3.5$ A. (b) Simulated optical output spectrum in double-pass configuration, with $I_{Rear} = 0.3$ A and $I_{Front} = 3.5$ A.

Figures 6.10a and 6.10b represent the output power spectra in single- (red) and double-pass (blue) configuration with $I_{Rear} = 0.3\,\mathrm{A}$ and $I_{Front} = 3.5\,\mathrm{A}$, under optical excitation. First of all, it has to be noted that there are the same prominent optical components that we had in CW conditions in the previous section. Then in both cases a very sharp peak emerges from this ASE baseline. It is located at 1258 nm and corresponds to the amplified light source through stimulated emission. We are of course interested in the capability of the device of amplifying the external optical signal, therefore we have to separate this contribution from the ASE. From Figures 6.10a and 6.10b, it is also already possible to see qualitatively that the double-pass configuration offers better amplification.

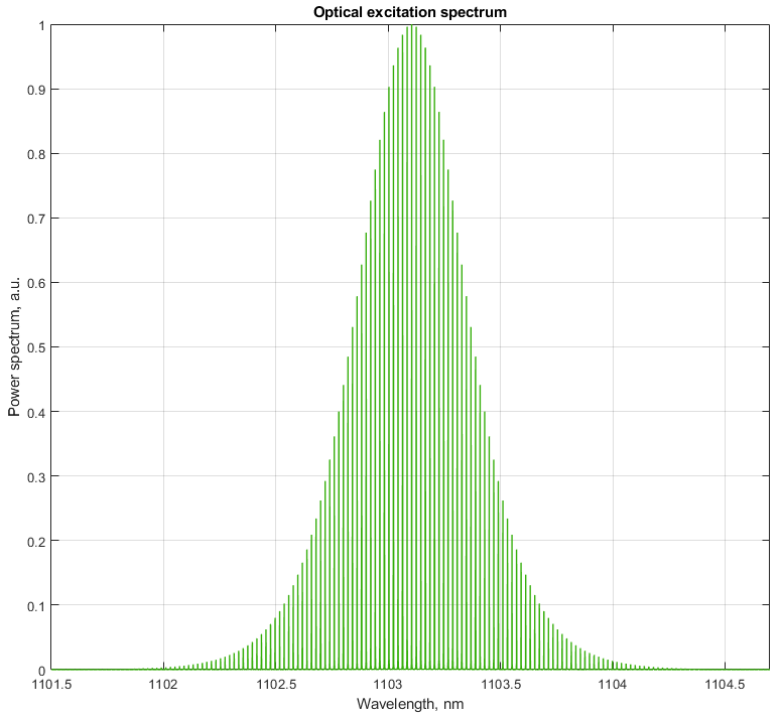

Figure 6.11. Power spectrum of the external optical source.

In the time domain, the concept is the same: the amplified pulses at the output facet of the device will be superimposed to the ASE power. In order to assess the properties of the amplified pulse train, of course, it is mandatory to separate the signal of interest from the ASE background. For this purpose, it is convenient to work in the frequency domain. We know the spectral occupation of the optical source signal (Figure 6.11) and we also know that it will not be affected by the amplification in the SOA. Therefore, we simply have to filter out everything outside the band occupied by the pulsed laser spectrum. This should leave us with the amplified optical excitation signal, superimposed to the remaining ASE falling in that window.

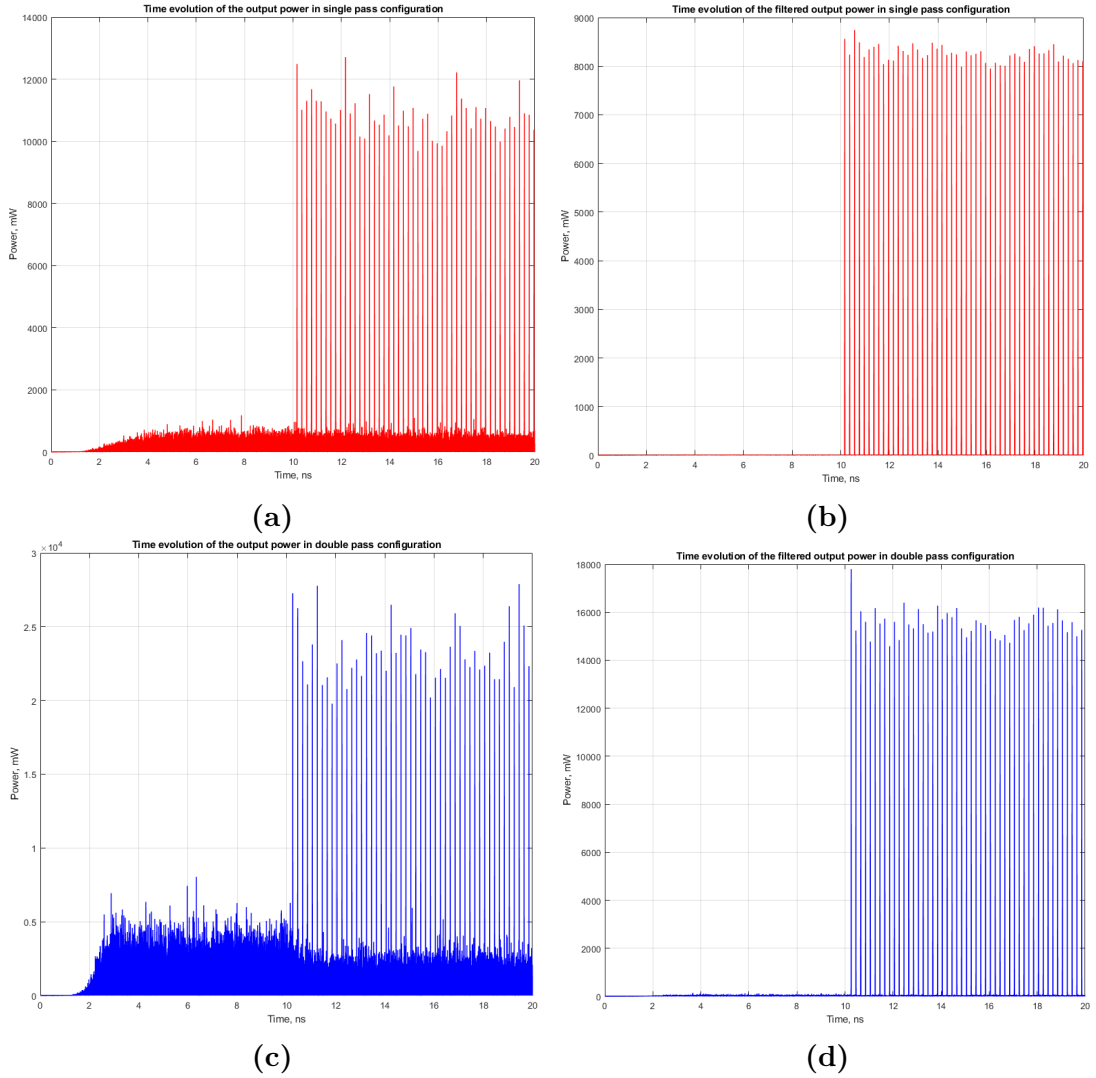

Figure 6.12. (a) Time evolution of the power at the output facet in single-pass configuration. (b) Time evolution of the power at the output facet in single-pass configuration without the ASE. (c) Time evolution of the power at the output facet in double-pass configuration. (d) Time evolution of the power at the output facet in double-pass configuration, without the ASE. All images are obtained for simulations with $I_{Rear} = 0.3\,\text{A}$ and $I_{Front} = 3.5\,\text{A}$.

Figures 6.12a and 6.12c represent the power with ASE at the output facet for the single- and double-pass configurations, respectively. The images are taken for a set of simulations with $I_{Rear} = 0.3\,\text{A}$ and $I_{Front} = 3.5\,\text{A}$, chosen randomly. After 10 ns, the pulses are already visible, but it is not possible to perform reliable measurements on power and pulse duration due to the presence of the ASE power. Therefore, employing the method explained before, Figures 6.12b and 6.12d are obtained. They represent the power filtered from ASE at the output facet for the

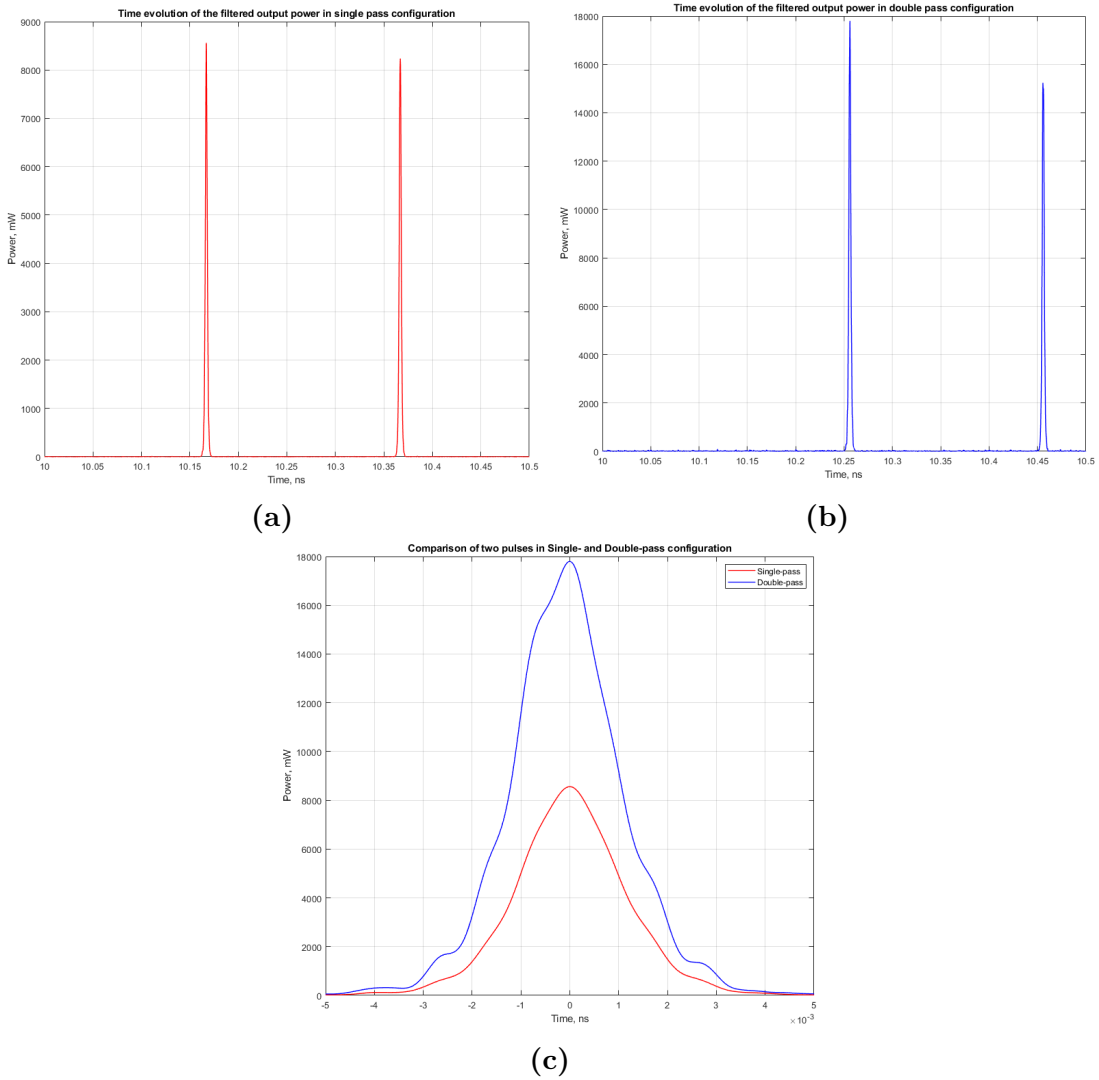

Figure 6.13. (a) Detail of the time evolution of the power at the output facet in single-pass configuration without the ASE. (b) Detail of the time evolution of the power at the output facet in double-pass configuration without the ASE. (c) Comparison of the first peak in single- and double-pass configuration. Shifted time axis for better comparison. All images are obtained for simulations with $I_{Rear} = 0.3\,\mathrm{A}$ and $I_{Front} = 3.5\,\mathrm{A}$.

single- and double-pass configurations, respectively.

It can be seen immediately that: a) with the double-pass configuration, the output power reaches higher values for the peaks; b) with the method employed, we are indeed able to delete the ASE noise power. In this way, we are left with the amplified train of pulses, that we can better analyse. Note that the pulse height is still not uniform due to the presence of the remaining portion of ASE noise in the band occupied by the external optical signal. In Figures 6.13a and 6.13b, details of

the trains of pulses in single- and double-pass configuration are reported. These images are detailing the time interval between 10 ns and 10.5 ns, thus containing the first two pulses of the trains. From Figure 6.13c, we can see immediately that we still have the square hyperbolic secant shape for the pulses in both configurations, despite having a bit of distortion in the double-pass case. This is not surprising because, with this configuration, the ASE noise is going to be amplified twice as well, thus impacting more on the useful optical signal.
If we concentrate on the first pulse, we can see that it is not located at the same time instant in the two configurations. In particular, we have that the first pulse is registered at $t = 10.1668$ ns for the single-pass configuration and at $t = 10.2561$ ns for the double-pass one. Of course, we have to consider that the light is travelling through the device with finite speed. Indeed, the results are consistent with the time that takes light to cross 6 mm of a device made out of a material with $n_r = 3.3445$ (exactly 66.89 ps) and with the time that takes light to cross twice the 6 mm of the device and twice the 1 mm of external cavity with $n_r = 1$ (exactly 140.54 ps).

At this point, we are finally able to compare the performances of the two possible configurations for what concerns output power and gain.

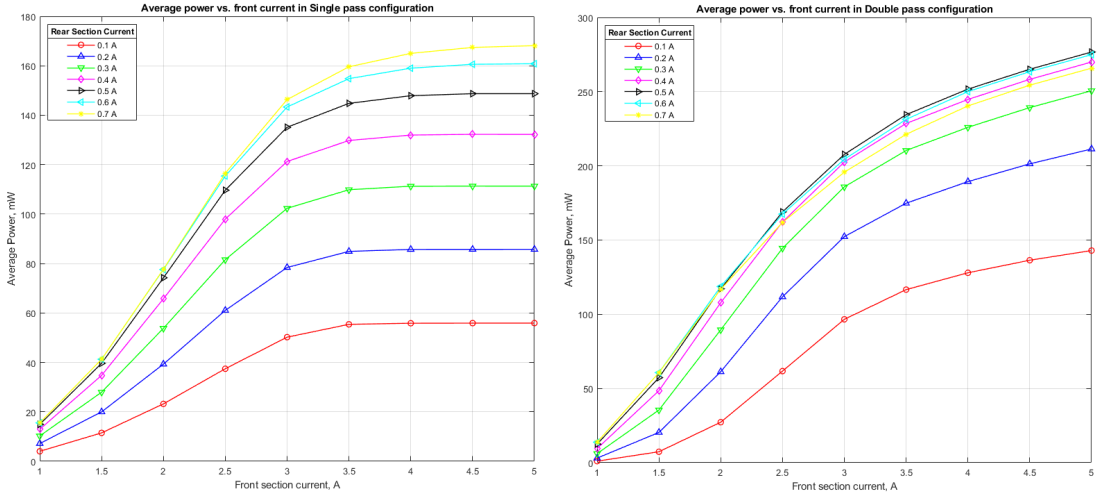

(a) **(b)**

Figure 6.14. (a) Plots of the average output power in single-pass configuration with respect to the front section current, for different values of rear section current. (b) Plots of the average output power in double-pass configuration with respect to the front section current, for different values of rear section current.

In Figures 6.14a and 6.14b, the power characteristics for single- (left plot) and double-pass (right plot) configurations are reported. As before, the different curves are characterised by different values of fixed rear section current and they are plotted with respect to the front section current. Starting from the single-pass

case, in Figure 6.14a, it is possible to appreciate a clear saturating behaviour with respect to increasing values of front section current, but also with respect to increasing values of rear section current, as it is clear that the curves associated to higher values of rear section current are closer to each other. However, in general, for a fixed value of front section current, simulations with higher rear section current yield a higher average output power. Although both the profiles and the values are consistent with the experimental results of [7], the results of the simulations are higher with respect to the experimental measurements. This is probably related, as before, to the fact that in the simulations the output power is measured directly outside the output facet of the device, while experimentally a lossy optical apparatus is needed in order to both couple the source to the SOA and to perform the measurements.
Continuing with the double-pass results for the average power, represented in Figure 6.14b, it can be seen right away that the profiles are slightly different and that, in general, the curves reach higher powers with respect to their single-pass counterparts. Anyway, the saturating behaviour is still present in the double-pass case as well. However, there is a peculiar behaviour that was not present in the single-pass results. If we consider the curve for $I_{Rear} = 0.7\,\mathrm{A}$ (yellow) at high values of front section current, we can see that its output power values are lower with respect to the curves with smaller rear section current, even the one with $I_{Rear} = 0.4\,\mathrm{A}$ (magenta). Similarly, the curve for $I_{Rear} = 0.6\,\mathrm{A}$ (cyan) at high values of front section current results to be lower than the curve with $I_{Rear} = 0.5\,\mathrm{A}$ (black). This effect can be explained as follows: due to the high optical power levels after the first passage through the device, the population of carriers in the QD states will be strongly depleted but, due to the closeness of the feedback mirror to the rear facet of the device and to the comparatively slow recovery time of the carriers, they will not be able to reach a new steady state before the second amplification of the external source signal. Therefore, it is reasonable to expect a reduction of the average output power, since there is a reduction of the amplifying capabilities of the device. In reality, these power levels are most likely too high to actually operate the device safely in the problematic biasing current configuration. Indeed, there are not experimental measures from [7] for the current configurations of interest in order to confirm this simulation behaviour. In any case, like before, the profiles of the curves are coherent and the simulated power values are slightly larger than the experimental measurements.

In reality, the power gain is a better parameter to compare the simulation and experimental results. In Figures 6.15, the simulation results are reported on the left (top left single-pass, bottom left double pass), while the experimental results are reported on the right (top left single-pass, bottom left double pass). Note that the experimental double-pass results are the ones associated to the experiments performed with the long-pass filter inserted inside the external cavity to avoid the

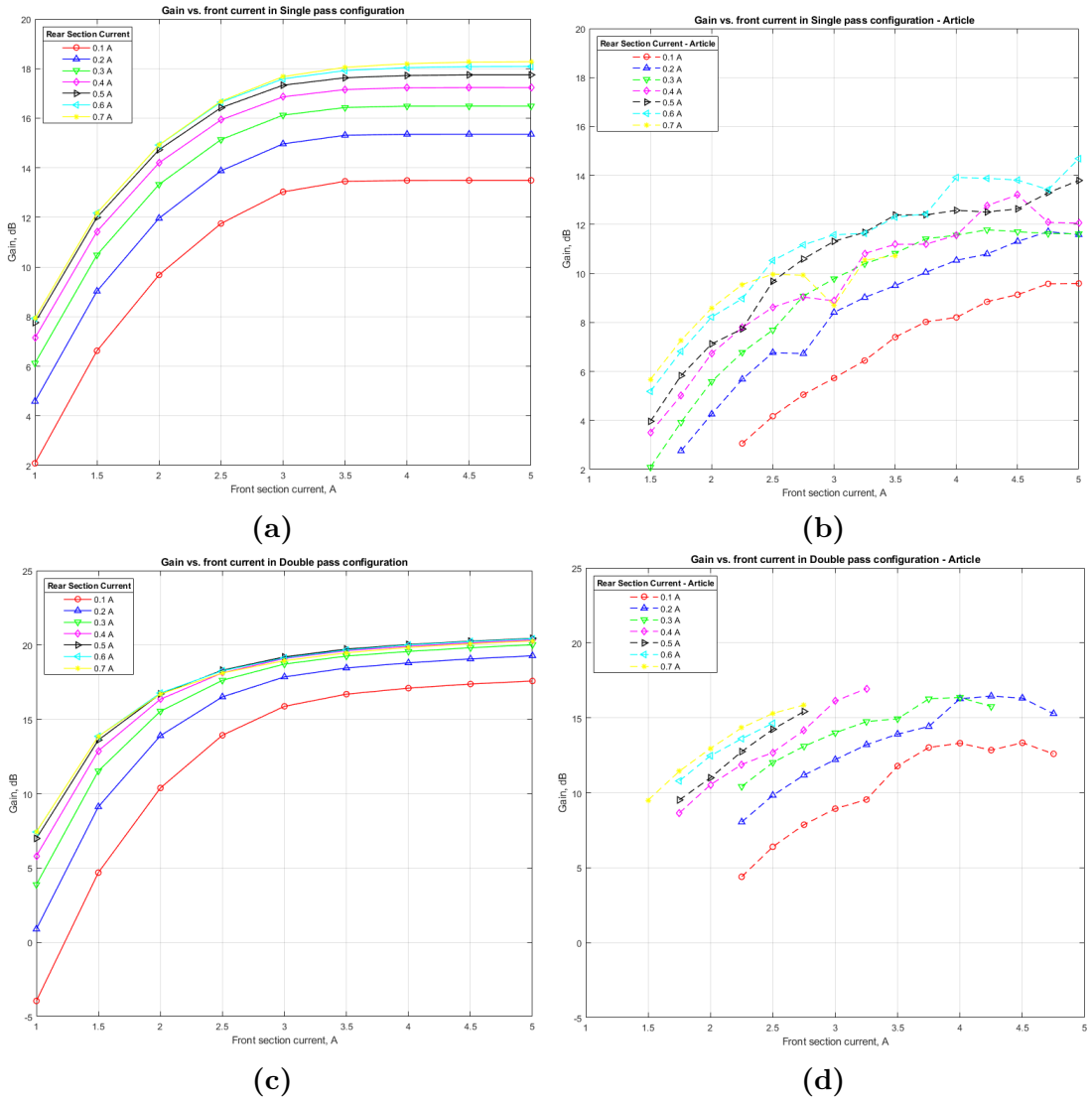

Figure 6.15. (a) Gain vs. front facet current in single-pass configuration. (b) Gain vs. front facet current in single-pass configuration from [7], data taken from [21]. (c) Gain vs. front facet current in double-pass configuration. (d) Gain vs. front facet current in double-pass configuration from [7], data taken from [21].

spurious lasing.

First of all, as we can expect from the analysis of the average output power and from the experimental evidences, the gain in double-pass is higher than in single-pass. If we then compare the simulation results with the experimental measurements, we can see that, in general, the simulations are characterised by the same profile with respect to the front section current. Indeed, it is possible to state that both the single- and double-pass gains present a saturating profile that reproduces quite well

the experimental measurements. This of course is in line with the saturating profile of the output power characteristic. If we compare the single-pass simulation (Figure 6.15a) with the results from [7] (Figure 6.15b), we can see that the simulated gain appears to be higher than the experimental results, approximately by a factor 2. If we consider then the double-pass simulation (Figure 6.15c) with the results from [7] (Figure 6.15d), the obtained values follow the same trend as the previous case. In [7], it was found that, without considering the long-pass filter,

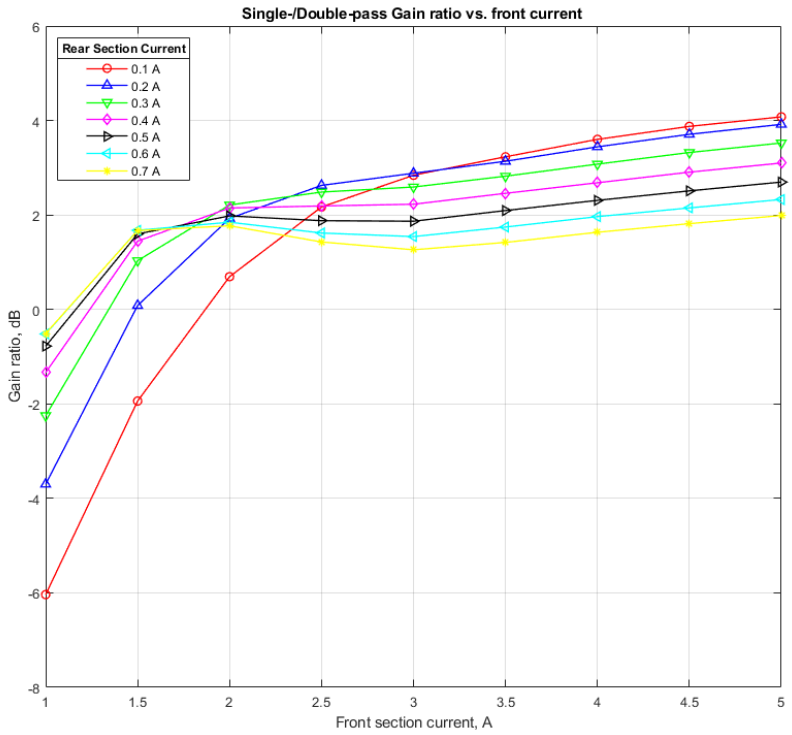

Figure 6.16. Double-/single-pass simulated gain ratio with respect to the front facet current, for different values of rear facet current.

in double-pass configuration, the improvement of the gain with respect to the single-pass configuration was around 3 dB, due to the presence of the spurious lasing that capped the amplifying capabilities of the SOA. With the insertion of the long-pass filter to forbid the lasing, they were able to retrieve a maximum improvement of 7 dB, with typical values of about 4 dB. The simulation results are in between these two opposite situation: the maximum enhancement of the double-pass gain with respect to the single-pass one is 4.1 dB (for the bias condition with $I_{Rear} = 0.1$ A and $I_{Front} = 5$ A), but the typical values range between 2.5 dB and 4 dB. A graphical representation of the ratio between double- and single-pass gains is contained in Figure 6.16. From this picture, we can also see that, for low values of front section current, the performances of the double-pass amplifier are not much better than those of the single-pass one, becoming even worse (negative

ratio in dB) for all curve at $I_{Front} = 1\,\text{A}$. Moreover, we have also that, for high values front section current, the double-pass configuration become progressively less convenient performance-wise with respect to the single-pass as the rear section current is increased. In reality this point can be easily predicted from the power characteristic in Figure 6.14b. Unfortunately, it is not possible to verify these limit behaviours since measurements for low front section currents and high front and rear section currents were not performed experimentally for [7].

Therefore, thus far the simulation results seem to confirm the experimental evidence that the double-pass configuration significantly improves the amplifying capabilities of the SOA under test, more than the factor 2 that one could predict from a double amplification of the source signal. At this point, we have to verify that this gain and output power enhancement does not imply a toll on the quality of the amplified pulses for what concerns the pulse duration. For this reason, a MATLAB function was implemented in order to recognize the peaks from the filtered time evolution of the output power and to measure the duration of each peak as its full width half maximum. The durations for each detected peak are collected and then averaged. In [7] it is stated that, for the single-pass configuration, the average duration of the amplified pulses ranges from 2.4 ps to 2.7 ps. For the double-pass configuration, instead, we have that the average duration of the amplified pulses ranges from 2.4 ps to 3.1 ps, meaning that the double amplification of the external optical signal does not degrade the quality of the pulses.

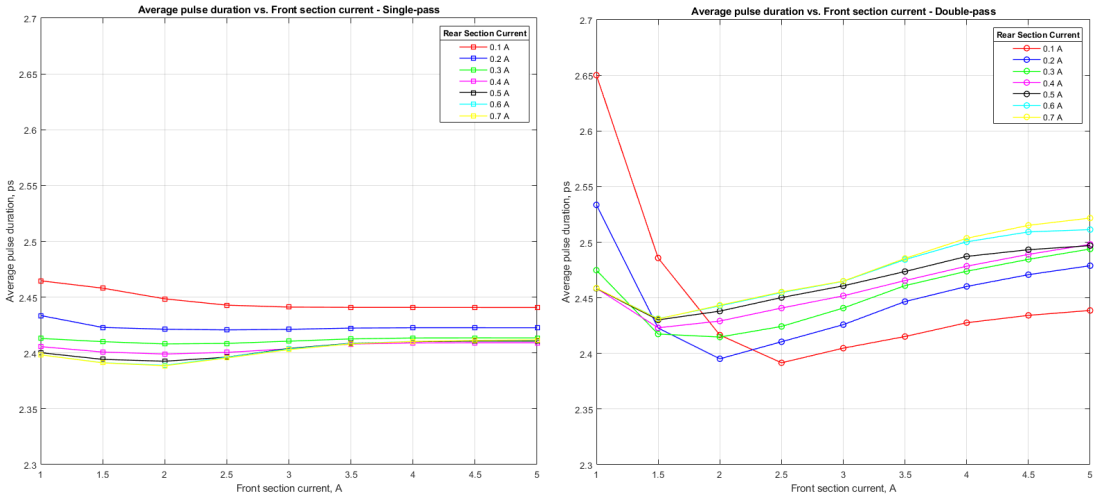

(a) **(b)**

Figure 6.17. (a) Average pulse duration in single-pass configuration with respect to the front section current, for different values of rear section current. (b) Average pulse duration in double-pass configuration with respect to the front section current, for different values of rear section current.

Figures 6.17 represent the trends of the average pulse durations with respect to the

front section current, for different fixed values of rear section current. Graphically, it is already clear that in the two cases we have similar values for the average durations. In particular, in the single-pass configuration case of Figure 6.17a, we have that the average duration is narrowly distributed between 2.4 ps to 2.45 ps, but the maximum registered duration is around 2.65 ps. A peculiar aspect is that in the single-pass case the simulations at lower rear section currents are characterised by more broadened peaks.

In the double-pass case, instead, the average pulse duration ranges from 2.4 ps to 2.65 ps, but there are values registered also over the 3.0 ps mark. In this case, contrary to what we had for the single-pass case, the simulations with higher rear section current have a longer average pulse duration, exception made for low values of front section current.

Therefore, it can be stated that the simulated results are congruent with the experimental measurements for what concerns the pulse duration of the amplified signal. Indeed, the single-pass and double-pass configurations have quite similar average pulse durations for the various combinations of rear and front section currents, despite the latter being characterised in some cases by longer values. In reality, there is not a perfect prediction of the experimental results, but this can be ascribed to the measurement uncertainty that of course affects any pratical measurement of any device.

These results, in conjunction with the average power results, therefore confirm the experimental evidences that the double-pass configuration for the chirped and tapered SOA seems to introduce a substantial enhancement of gain and output power (more than a factor 2), but without degrading the quality of the original signal: the maximum increase of the pulse duration is 2.65 ps and it is associated to a bias condition in which we do not have high gain, so it will not be used in practice anyway. This is a good outcome, especially considering that the maximum increase in average pulse duration in single-pass configuration is merely 0.2 ps lower.

This means that the simulation results confirm the thesis of [7] that the double-pass configuration for the SOA has very promising features that could make it the new standard for the amplification of ultrashort pulsed light source such as mode-locked lasers. For sure, SOAs cannot be employed effectively if the double-pass configuration is implemented with the external feedback mirror that was considered in the simulations, due to the increased area occupation and the stringent requirements concerning the alignment of both facets of the device. However, it has the advantage of potentially allowing the creation of an integrated double-pass configuration by means of a highly reflective rear facet: in this way, the device would bring all the positive features of the double-pass configuration, but with the area occupation of a traditional SOA. It would also require the alignment of the front facet only, thus simplifying the practical setup. The only real disadvantage that can be foreseen consists in the mandatory use of some kind of one-way optical gate to keep the input and output signals well separated, although introducing

possibly additional losses and spurious reflections. Moreover, it would be necessary to check which power levels this integrated implementation is able to withstand, before experiencing the reduction of the amplifying capabilities that has been obtained in Figure 6.14b for high driving currents.

Chapter 7

Conclusions and outlook

In this thesis work, a preexisting TDTW MATLAB simulator for QD-based lasers was adapted in order to simulate chirped and tapered SOAs, by including the chirped QD layers and the stimulated emission from the second QD excited state, which is usually neglected in laser models since it has negligible effects, but it is important in SOA models.

This TDTW simulator was then used in order to simulate the chirped, tapered and double-section SOA studied by the Photonic group at Heriot-Watt University, Edinburgh, thus trying to validate the simulated results with the experimental ones. In particular, three kinds of simulations were performed: continuous wave simulations without external optical excitation, in which the device works as a superluminescent diode, single-pass simulations and, finally, double-pass simulation, both under external optical pumping from a mode-locked laser.

The results were in general congruent with the experimental data. Indeed, for the SLED simulations, the output power levels were larger with respect the measured values, but within 3 dB; the power spectra were affected by a tunable spectral asymmetry. For the single- and double-pass simulations with external optical excitation, the latter was characterised by power levels larger of a factor 4.1 dB, but with average pulse durations between 2.4 ps and 2.7 ps, with respect to the duration of 2.3 ps of the pulses emitted by the optical source.

The simulated results are qualitatively reproducing the experimental data. For instance, the spectral asymmetry is less tunable with respect to the actual device, due to the presence of a spectral component at 1210 nm that is stronger than what it should be. Moreover, we have that in the range of wavelengths between 1140 nm and 1210 nm are less attenuated than how they should. This implies that the QD levels are filled in a way that does not correspond perfectly to the reality and that could be the reason behind the reduced spectral asymmetry.

Further improvements can be done by modifying the device parameters inside `DeviceData_SOA`, especially the gain and the escape and capture characteristic times related to the QD discrete confined states, using once again the SLED

simulation results as a reference, since they last less than those with external optical excitation.

It could be interesting also to introduce in the simulation the leftover spurious reflectivity of the facets (e.g. low values as $r = 1 \times 10^{-3}$), in order to verify whether the simulator is able to predict the spurious lasing detuned from the wavelength of the external source, that was detected in the double-pass measurements in [7] and that reduced the amplifying capabilities of the SOA for high current bias. At that point, it would be useful to model the long-pass filter that was used in order to prevent the lasing, in order to estimate the advantages that it would produce. It would be also interesting to implement the double pass configuration with the highly reflective rear facet in order to asses the performances of the SOA in these conditions and the possible issues that could arise.
Once the remaining minor issues are fixed, another possible further work could consist in the iterative modification of the device parameters (i.e. maching learning-assisted code) with the goal of finding possible device structures and/or active material compositions able to provide even better performances in the double-pass configuration with respect to the device that was analysed in this thesis.

Bibliography

[1] P. Bardella, L. Columbo, and M. Gioannini. «Self-generation of optical frequency comb in single section quantum dot Fabry-Perot lasers: a theoretical study». In: *Opt. Express* 25.21 (Oct. 2017), pp. 26234–26252. DOI: 10.1364/OE.25.026234 (cit. on pp. 2, 62).

[2] P. Bardella, M. Rossetti, and I. Montrosset. «Modeling of Broadband Chirped Quantum-Dot Super-Luminescent Diodes». In: *IEEE Journal of Selected Topics in Quantum Electronics* 15.3 (May 2009), pp. 785–791. DOI: 10.1109/JSTQE.2009.2013128 (cit. on p. 22).

[3] M. Van Beest. «Fock-Darwin States for an Elliptical Spin-Orbit Coupled Quantum Well». Bachelor's Thesis. Niels Bohr Institute, University of Copenhagen, 2015 (cit. on p. 6).

[4] P. Blood, H. Pask, H.D. Summers, and I. Sandall. «Localized Auger Recombination in Quantum-Dot Lasers». In: *IEEE Journal of Quantum Electronics* 43.12 (Dec. 2007), pp. 1140–1146. DOI: 10.1109/JQE.2007.907541 (cit. on p. 20).

[5] L. A. Coldren. *Diode Lasers and Photonic Integrated Circuits*. Wiley Series in Microwave and Optical Engineering. John Wiley and Sons, Inc., 2012. ISBN: 0-470-48412-8 (cit. on p. 15).

[6] A. F. Forrest, M. A. Cataluna, M. Krakowski, G. Giannuzzi, and P. Bardella. «Numerical and Experimental Characterization of Chirped Quantum Dot-based Semiconductor Optical Amplifiers». In: *2021 International Conference on Numerical Simulation of Optoelectronic Devices (NUSOD)*. 2021, pp. 17–18. DOI: 10.1109/NUSOD52207.2021.9541489 (cit. on p. 12).

[7] A. F. Forrest, M. Krakowski, P. Bardella, and M. A. Cataluna. «Double-pass amplification of picosecond pulses with a tapered semiconductor amplifier». In: *Opt. Express* 27.21 (Oct. 2019), pp. 30752–30762. DOI: 10.1364/OE.27.030752 (cit. on pp. ii, 2, 3, 26, 27, 29–31, 46, 47, 69, 81, 86–90, 93).

[8] A. F. Forrest, M. Krakowski, P. Bardella, and M. A. Cataluna. «High-power quantum-dot superluminescent tapered diode under CW operation». In:

Opt. Express 27.8 (Apr. 2019), pp. 10981–10990. DOI: 10.1364/OE.27.010981 (cit. on pp. 2, 26, 69, 70, 74).

[9] A. F. Forrest, M. Krakowski, P. Bardella, and M. A. Cataluna. «Wide and tunable spectral asymmetry between narrow and wide facet outputs in a tapered quantum-dot superluminescent diode». In: *Opt. Express* 28.2 (Jan. 2020), pp. 846–859. DOI: 10.1364/OE.377768 (cit. on pp. 3, 27–29, 32, 33, 39, 41, 56, 69–72, 74, 76–78).

[10] S. Franchi, G. Trevisi, L. Seravalli, and P. Frigeri. «Quantum dot nanostructures and molecular beam epitaxy». In: *Progress in Crystal Growth and Characterization of Materials* 47.2 (2003). Vapour Growth of Bulk Crystals and Epitaxy: Part I, pp. 166–195. ISSN: 0960-8974. DOI: https://doi.org/10.1016/j.pcrysgrow.2005.01.002 (cit. on pp. 9, 10).

[11] G. Ghione. *Semiconductor Devices for High-Speed Optoelectronics*. Cambridge: Cambridge University Press, 2009. ISBN: 0521763444 (cit. on pp. 4, 8, 18).

[12] M. Gioannini, P. Bardella, and I. Montrosset. «Time-Domain Traveling-Wave Analysis of the Multimode Dynamics of Quantum Dot Fabry-Perot Lasers». In: *IEEE journal of selected topics in quantum electronics* 21.6 (2015), pp. 698–708. ISSN: 1077-260X (cit. on p. 18).

[13] M. Gioannini and I. Montrosset. «Numerical Analysis of the Frequency Chirp in Quantum-Dot Semiconductor Lasers». In: *IEEE Journal of Quantum Electronics* 43.10 (Oct. 2007), pp. 941–949. DOI: 10.1109/JQE.2007.904306 (cit. on pp. 2, 18).

[14] M. van der Poel, E. Gehrig, O. Hess, D. Birkedal, and J.M. Hvam. «Ultrafast gain dynamics in quantum-dot amplifiers: theoretical analysis and experimental investigations». In: *IEEE Journal of Quantum Electronics* 41.9 (Sept. 2005), pp. 1115–1123. DOI: 10.1109/JQE.2005.852795 (cit. on p. 2).

[15] M. Razeghi. «Semiconductor Heterostructures and Low-Dimensional Quantum Structures». In: *Fundamentals of Solid State Engineering*. Springer International Publishing, 2018, pp. 473–512. ISBN: 3319757075 (cit. on pp. 6, 8).

[16] M. Rossetti. «Numerical modeling of light sources based on semiconductor quantum dots». PhD thesis. Politecnico di Torino, 2011 (cit. on pp. 5–7, 10, 13).

[17] M. Rossetti, P. Bardella, and I. Montrosset. «Time-Domain Travelling-Wave Model for Quantum Dot Passively Mode-Locked Lasers». In: *IEEE Journal of Quantum Electronics* 47.2 (Feb. 2011), pp. 139–150. DOI: 10.1109/JQE.2010.2055550 (cit. on pp. 2, 10, 12, 14, 15, 17, 18, 22).

[18] A. Wojs, P. Hawrylak, S. Fafard, and L. Jacak. «Electronic structure and magneto-optics of self-assembled quantum dots». In: *Physical review. B, Condensed matter* 54.8 (1996), pp. 5604–5608. ISSN: 0163-1829 (cit. on p. 5).

Sitography

[19] *FEL1250 - Ø1" Longpass Filter, Cut-On Wavelength: 1250 nm.* URL: https://www.thorlabs.com/thorproduct.cfm?partnumber=FEL1250 (cit. on p. 30).

[20] *Laser Pulse Calculator.* URL: https://www.calctool.org/optics/laser-pulse (cit. on p. 47).

[21] *Research Data for "Double-pass amplification of picosecond pulses with a tapered semiconductor amplifier".* URL: https://researchportal.hw.ac.uk/en/datasets/research-data-for-double-pass-amplification-of-picosecond-pulses- (cit. on p. 87).

[22] *Research Data for "High power quantum dot superluminescent tapered diode under CW operation".* URL: https://researchportal.hw.ac.uk/en/datasets/research-data-for-high-power-quantum-dot-superluminescent-tapered (cit. on pp. 74, 75).

[23] *Research Data for "Wide and tunable spectral asymmetry between narrow and wide facet outputs in a tapered quantum-dot superluminescent diode".* URL: https://researchportal.hw.ac.uk/en/datasets/research-data-for-wide-and-tunable-spectral-asymmetry-between-nar (cit. on pp. 71, 74, 75).

[24] *RP Photonics Encyclopedia - Sech2-shaped Pulses.* URL: https://www.rp-photonics.com/sech2_shaped_pulses.html (cit. on p. 47).

[25] *Self-Formation of High-Uniformity and High-Density Quantum Dots.* URL: http://www.crystal.ee.uec.ac.jp/works/t1_e.html (cit. on p. 9).